

Abstract

COFFEY, TONYA SHEA. Nanotribology Fundamentals: Predicting the Viscous Coefficient of Friction. (Under the supervision of Professor Jacqueline Krim.)

In this work, I have used the Quartz Crystal Microbalance (QCM) to study nanoscale friction of monolayer adsorbates on (111) metals. The friction of these systems is viscous friction, defined as $F_f = \eta v = \left(\frac{m}{\tau}\right)v$. Here, η is the viscous coefficient of friction, v is the velocity of the adsorbate, m is adsorbate mass, and τ is the slip time, which is the time required for the film's speed to fall to $1/e$ of its original value. The main focus of this dissertation is to determine the factors that control η , the viscous coefficient of friction. I have examined three different parameters in order to determine their effect on η .

An equation for predicting the viscous coefficient of friction has been proposed:

$\eta = \eta_{subs} + aU_o^2$. Here, η_{subs} is the damping of adsorbate sliding energy within the substrate, a is a constant depending on mainly temperature and adsorbate film coverage, and U_o is the atomic-scale surface corrugation. I have closely examined the effect of varying U_o while holding the lattice spacing relatively constant by studying the slippage of xenon films on Cu(111), Ni(111), graphene, and C_{60} substrates at 77.4 K. I have also examined the effect of varying η_{subs} while controlling other parameters by studying the slippage of n-octane films on Cu(111) vs. Pb(111) surfaces at room temperature.

It was found that the slippage of xenon on Cu(111), Ni(111), and graphene/Ni(111) was very well fit by the proposed equation. These three systems had very similar nearest neighbor lattice spacings (0.255 nm, 0.249 nm, and 0.249 nm, respectively) but varying atomic scale surface corrugations (1.9 meV, 14 meV, and 5.3 meV, respectively.) The xenon

monolayer slip times (τ) of 15.5 ns, 0.41 ns, and 1.7 ns, respectively, were well fit by the relation $\tau \propto U_o^{-2}$. Specifically, when plotted on a $\ln \tau$ vs. $\ln U_o$ plot, the data were fit by a slope of -1.82 ± 0.20 .

It has been proposed that η_{subs} should be linearly proportional to the damping of frustrated translational (FT) phonon modes (γ) of an adsorbate-substrate system via $\gamma = h\eta$. The parallel FT modes are believed to be directly linked to the sliding friction, but it is not clear how damping of the perpendicular FT modes (FT_z) affect sliding friction. To explore this question, I have examined the sliding friction of n-octane on Cu(111) vs. Pb(111) surfaces, which have $\gamma = 0.45$ meV and $\gamma = 0.26$ meV, respectively. I have observed that the slip time for a monolayer of n-octane/Cu(111) is 0.94 ns \pm 0.36 ns, and the slip time of n-octane/Pb(111) is 0.59 ns \pm 0.13 ns. I therefore observe no direct evidence of a link between the damping of perpendicular FT modes and sliding friction. It is still possible, however, that the damping of the parallel FT phonon mode affects sliding friction.

Finally, I studied the slippage of monolayer methanol films at room temperature on rotating, rigid, and slowly ratcheting C₆₀ substrates, to examine the effect that the molecular rotation of the substrate surface has on the sliding friction of an adsorbate. It had been hypothesized that the rotation of the C₆₀ molecules might reduce friction, because the round, rotating C₆₀ could act as a nanoscale ball bearing. I found that the slippage and mass uptake for methanol on rigid and slowly ratcheting C₆₀ was indistinguishable. I found that at all coverages, the slip time for methanol on rigid and slowly ratcheting C₆₀ was longer (hence lower friction) than the slip time for methanol on rotating C₆₀, defying the ball bearing analogy.

NANOTRIBOLOGY FUNDAMENTALS:
PREDICTING THE VISCOUS COEFFICIENT OF FRICTION

by
TONYA S. COFFEY

A dissertation submitted to the Graduate Faculty of
North Carolina State University
in partial fulfillment of the
requirements of the Degree of
Doctor of Philosophy

PHYSICS

Raleigh
2004

APPROVED BY:

Chair of Advisory Committee

*In dedication to my family—
My husband, Chris, my child, Nick
And my Mom and Dad
I couldn't have done this alone!*

BIOGRAPHY

I was born in Lenoir, North Carolina in February of 1975 and graduated from Hibriten High School in Lenoir in 1992. I received both my bachelors and masters degrees in physics from North Carolina State University.

I have enjoyed being at NCSU. The university has given me many wonderful experiences. Thanks to NCSU, I traveled Europe in a study abroad program. I was able to participate in state-of-the-art physics research. I have become more confident in myself and my abilities. I also made many lifelong friends—especially my husband, Chris Thaxton, a fellow physicist, who I married on July 31st, 1999.

In August of 2004, I will be starting my new job as a professor at Appalachian State University in Boone, NC. I hope my time there will be as special as my time in Raleigh.

ACKNOWLEDGEMENTS

I wish to thank my advisory committee, Marco Buongiorno Nardelli, Dale Sayers, Christine Grant, and Jacqueline Krim. They provided the focus, motivation, and accessibility I needed to complete my work and continue to fuel my scientific creativity and professional growth.

I'd like to especially thank Jackie Krim, advisor extraordinaire, cheerleader, provider of health insurance, and friend. She gave me the confidence to develop as a scientist. She listened, gave valuable advice, and bragged about my work to colleagues. I'll miss working with you on a daily basis, Jackie, but I look forward to many future collaborations.

I thank my co-workers, especially Brian Borovsky, Mohamed Abdelmaksoud, Chernoo Jaye, Sang-Min Lee, Adam Hook, and Matt Highland. They have helped in ways too numerous to count.

I thank my in-laws, June and John Thaxton, for their gracious support and their unconditional acceptance of me into their family.

I thank my parents, Barry and Gayle Coffey, for standing by me always. They helped me in every way someone can be helped.

Finally, I thank my husband, Chris Thaxton. I love you, Chris!

TABLE OF CONTENTS

LIST OF TABLES	x
LIST OF FIGURES	xi
CHAPTER 1: INTRODUCTION.....	1
1.1 BRIEF HISTORY OF FRICTION	1
1.2 AIMS OF THE DISSERTATION.....	5
1.3 REVIEW OF PRIOR WORK	6
CHAPTER 2: PREDICTING THE VISCOUS COEFFICIENT OF FRICTION.....	20
CHAPTER 3: EXPERIMENTAL METHODS AND APPARATUS.....	26
3.1 QUARTZ CRYSTAL MICROBALANCE (QCM).....	26
3.1.1 GENERAL DESCRIPTION AND COMMON USES.....	26
3.1.2 RELATIONSHIP BETWEEN MASS UPTAKE AND FREQUENCY SHIFT	27
3.1.3 THE QUALITY FACTOR	29
3.1.4 SLIDING FRICTION MEASUREMENTS	30
3.1.5 ACOUSTIC IMPEDANCE	31
(a) <i>Acoustic Impedance of a Viscous Film</i>	31

(b)	<i>Acoustic Impedance of a 3-D Gas</i>	33
(c)	<i>Acoustic Impedance of a Film-Vapor System</i>	34
3.1.6	DAMPING DUE TO INTERFACIAL SLIPPAGE	36
3.1.7	EXPERIMENTAL DETERMINATION OF Q.....	37
3.1.8	FACTORS AFFECTING THE QCM FREQUENCY.....	39
(a)	<i>Temperature</i>	39
(b)	<i>Gas Pressure</i>	40
(c)	<i>Stress</i>	41
(d)	<i>Mass Uptake and Slippage</i>	42
3.1.9	NET FREQUENCY SHIFT.....	42
3.2	EXPERIMENTAL HARDWARE	43
3.3	ELECTRONICS AND QCM CALIBRATION	44
	CHAPTER 4: IMPACT OF ATOMIC CORRUGATION ON SLIDING FRICTION AS PROBED BY QCM	53
	ABSTRACT	53
4.1	INTRODUCTION	54
4.2	EXPERIMENTAL	56
4.3	RESULTS	57
4.4	ANALYSIS AND DISCUSSION	58

CHAPTER 5: QUARTZ CRYSTAL MICROBALANCE STUDIES OF THE SLIPPAGE OF SOLID AND LIQUID KRYPTON MONOLAYERS ON METAL(111) AND C60

SURFACES 67

ABSTRACT 67

5.1 INTRODUCTION 68

5.2 EXPERIMENTAL 70

5.3 RESULTS 71

5.4 DISCUSSION 72

5.5 CONCLUSION 74

CHAPTER 6: THE EFFECT OF CHANGING ADSORBATE DAMPING ON THE VISCOUS COEFFICIENT OF FRICTION 84

ABSTRACT 84

6.1 INTRODUCTION 85

6.2 EXPERIMENTAL DETAILS 88

6.3 RESULTS AND DISCUSSION 89

CHAPTER 7: QUARTZ CRYSTAL MICROBALANCES STUDIES OF THE FRICTION OF ROTATING VS. RIGID C60 97

ABSTRACT 97

7.1 INTRODUCTION 98

7.2 EXPERIMENTAL 100

7.3 RESULTS 102

7.4 CONCLUSION 103

CHAPTER 8: A SCANNING PROBE AND QUARTZ CRYSTAL MICROBALANCE STUDY OF THE IMPACT OF C60 ON FRICTION AT SOLID-LIQUID INTERFACES.. 111

ABSTRACT..... 111

8.1 INTRODUCTION..... 112

8.2 AFM EXPERIMENTAL DETAILS AND RESULTS 116

8.3 QCM EXPERIMENTAL DETAILS AND RESULTS..... 118

8.3.1 QCM IN VACUUM 118

8.3.2 QCM IN LIQUIDS 120

8.4 DISCUSSION 121

8.5 FUTURE WORK.....	122
ACKNOWLEDGEMENTS	123
CHAPTER 9: CONCLUSIONS	129
APPENDIX.....	133
BIBLIOGRAPHY.....	160

LIST OF TABLES

TABLE 3.1	GAS PARAMETERS USED TO ANALYZE ADSORPTION DATA IN THIS WORK. ATOMIC WEIGHTS WERE OBTAINED FROM THE PERIODIC TABLE OF ELEMENTS.....	52
TABLE 4.1	THE SURFACE CORRUGATIONS, SUBSTRATE SPACING, AND OVERLAYER SPACING FOR AG(111), CU(111), NI(111), AND GRAPHENE/NI(111).....	66
TABLE 4.2	MONOLAYER SLIP TIMES AND SURFACE CORRUGATION FOR CU(111), AG(111), NI(111), GRAPHENE/NI(111), AND C ₆₀ /AG(111).....	66
TABLE 5.1	SLIP TIMES FOR THE LIQUID (τ_{LIQ}), SOLID (τ_{SOL}) PHASES OF KRYPTON AT GIVEN MONOLAYER COVERAGE (Θ) AND THE RATIO OF THE SLIP TIME OF LIQUID AND SOLID PHASES FOR THE VARIOUS SUBSTRATES.....	83
TABLE A.1	CHAPTER 4 HELIUM CALIBRATION INFORMATION.....	159

LIST OF FIGURES

FIGURE 1.1	APPARENT VERSUS ACTUAL AREA OF CONTACT	15
FIGURE 1.2	SURFACE FORCES APPARATUS SCHEMATIC.....	15
FIGURE 1.3	LATERAL (ATOMIC) FORCE MICROSCOPE SCHEMATIC.	16
FIGURE 1.4	QUARTZ CRYSTAL MICROBALANCE SCHEMATIC	16
FIGURE 1.5	FREQUENCY SHIFT , CHANGE IN QUALITY FACTOR, AND SLIP TIME DATA FOR KRYPTON ON AU(111) AND AG(111) AT 77 K	17
FIGURE 1.6	THE SOLID LINE SHOWS THE EXPERIMENTAL DATA FOR KR/AU(111) FOR KRIM ET AL. THE TRIANGLES REPRESENT THE THEORETICAL MODEL OF CIEPLAK ET AL.....	17
FIGURE 1.7	FREQUENCY SHIFT AND COVERAGE FOR XENON ON AG(111) AT 77 K.	18
FIGURE 1.8	THE SLIP TIME (TOP) AND SHEAR STRESS (BOTTOM) FOR XENON SLIDING ON AG(111) AT 77 K.....	18
FIGURE 1.9	THE SOLID LINES REPRESENT THE XE/AG(111) SLIP TIME DATA FROM DALY AND KRIM..	19
FIGURE 2.1	INTERNAL VIBRATIONAL MODES OF A FREE MOLECULE...25	
FIGURE 2.2	EXTERNAL VIRBRATIONAL MODES OF AN ABSORBED MOLECULE.	25
FIGURE 3.1	QCM SCHEMATIC.	47
FIGURE 3.2	SIDE VIEW OF QCM WHEN IT IS OSCILLATING IN TRANVERSE SHEAR MODE.....	47
FIGURE 3.3A	QUARTZ CRYSTAL AXES.....	48
FIGURE 3.4	PICTURE OF UHV CHAMBER.	48
FIGURE 3.5	PICTURE OF SAMPLE HOLDING CELL.....	49
FIGURE 3.6	SCHEMATIC OF PIERCE OSCILLATOR CIRCUIT.....	49
FIGURE 3.7	PICTURE OF CONTROL ELECTRONICS.....	50

FIGURE 3.8	A TYPICAL EXAMPLE OF A QCM GAS CALIBRATION.....	51
FIGURE 3.9	SCHEMATIC AND PICTURE OF RING DOWN CALIBRATION METHOD.....	51
FIGURE 4.1	XENON MASS UPTAKE AND QUALITY FACTOR SHIFT FOR CU(111), NI(111), AND GRAPHENE/NI(111).....	61
FIGURE 4.2	THE SLIP TIMES FOR XENON ON CU(111), NI(111), AND GRAPHENE/NI(111).....	62
FIGURE 4.3A	XENON MASS UPTAKE AND QUALITY FACTOR SHIFT FOR C ₆₀ /AG(111).....	63
FIGURE 4.3B	SLIP TIME FOR XENON SLIDING ON C ₆₀ /AG(111)	64
FIGURE 4.4	NATURAL LOG OF THE SLIP TIME VS. NATURAL LOG OF THE SURFACE CORRUGATION.....	65
FIGURE 5.1	SLIP TIME DATA ACQUIRED BY KRIM ET AL. FOR KR/AU(111) COMPARED TO NUMERICAL SIMULATION.....	75
FIGURE 5.2	FREQUENCY AND INVERSE QUALITY SHIFTS FOR KR/CU(111).....	76
FIGURE 5.3	FREQUENCY AND INVERSE QUALITY SHIFTS FOR KR/AG(111).....	77
FIGURE 5.4	FREQUENCY AND INVERSE QUALITY SHIFTS FOR KR/NI(111).....	78
FIGURE 5.5	FREQUENCY AND INVERSE QUALITY SHIFTS FOR KR/MONOLAYER C ₆₀	79
FIGURE 5.6	FREQUENCY AND INVERSE QUALITY SHIFTS FOR KR/BILAYER C ₆₀	80
FIGURE 5.7	QCM SLIP TIME DATA FOR KR/CU(111).....	81
FIGURE 5.8	QCM SLIP TIME DATA FOR KR/AG(111).	81
FIGURE 5.9	QCM SLIP TIME DATA FOR KR/NI(111).....	82

FIGURE 5.10	QCM SLIP TIME DATA FOR KR/MONOLAYER C ₆₀ AND BILAYER C ₆₀ . (JUNE 2003 SAMPLE)	82
FIGURE 6.1	HAS DATA FOR N-OCTANE ON CU(111) (TOP) AND N-OCTANE ON PB(111).	92
FIGURE 6.2	AVERAGE N-OCTANE MASS UPTAKE ON CU(111) AND PB(111).....	93
FIGURE 6.3	AVERAGE N-OCTANE SLIP TIME ATOP CU(111) AND PB(111) 93	
FIGURE 6.4	CONTOUR PLOT OF THE UNIT CELL FOR N-OCTANE ADSORPTION ONTO THE “ON TOP SITES” OF CU(111).....	94
FIGURE 6.5	CONTOUR PLOT OF THE UNIT CELL FOR N-OCTANE ADSORPTION ONTO THE “3-FOLD HOLLOW SITES” OF CU(111).	95
FIGURE 6.6	FREQUENCY AND QUALITY FACTOR SHIFT FOR A REPRESENTATIVE SAMPLE FOR N-OCTANE ON CU(111) AND PB(111). ...	96
FIGURE 7.1	FRICITION VS. LOAD CURVES ACQUIRED BY LIANG ET AL. USING LFM FOR A C ₆₀ COATED TIP SLIDING ON A C ₆₀ CRYSTALLINE SURFACE.	104
FIGURE 7.2	SCHEMATIC OF OUR QCM EXPERIMENT.	105
FIGURE 7.3	REPRESENTATIVE FREQUENCY SHIFT AND QUALITY FACTOR DATA FOR KRYPTON ADSORBED ONTO A MONOLAYER C ₆₀ /AG(111) SUBSTRATE.	106
FIGURE 7.4	AVERAGE METHANOL FREQUENCY SHIFT AND COVERAGE DATA FOR THE 4 C ₆₀ MONOLAYER AND 4 C ₆₀ BILAYER SAMPLES.	107
FIGURE 7.5	THE METHANOL SLIP TIMES FOR ALL 8 C ₆₀ SAMPLES.	108
FIGURE 7.6	THE AVERAGE SLIP TIMES FOR METHANOL ON MONOLAYER C ₆₀ AND BILAYER C ₆₀ SAMPLES.....	109
FIGURE 7.7	THE AVERAGE SLIP TIMES FOR KRYPTON SLIDING ON C ₆₀ MONOLAYER AND C ₆₀ BILAYER FILMS.	110

FIGURE 8.1	AN AFM ATOMIC-SCALE IMAGE OF THE MICA LATTICE SUBMERGED IN TOLUENE.....	124
FIGURE 8.2	AN AFM ATOMIC-SCALE IMAGE OF THE MICA LATTICE SUBMERGED IN THE C ₆₀ /TOLUENE SOLUTION.	124
FIGURE 8.3	FRICTIONAL FORCE VS. NORMAL FORCE FOR BARE MICA IN AIR VS. MICA SUBMERGED IN TOLUENE.....	125
FIGURE 8.4	FRICTIONAL FORCE VS. NORMAL FORCE FOR MICA SUBMERGED IN TOLUENE VS. MICA SUBMERGED IN THE C ₆₀ /TOLUENE SOLUTION.....	126
FIGURE 8.5	QCM FREQUENCY SHIFTS FOR TOLUENE ON AG(111) AND TOLUENE ON C ₆₀ /AG(111).....	127
FIGURE 8.6	QCM SLIP TIMES FOR TOLUENE ON AG(111) AND TOLUENE ON C ₆₀ /AG(111).....	128
FIGURE A.1	KR/AG(111), 120503A.DAT.	134
FIGURE A.2	KR/MONOLAYER C ₆₀ /AG(111), 121103A.DAT.	135
FIGURE A.3	KR/BILAYER C ₆₀ /AG(111), 121703A.DAT.....	136
FIGURE A.4	N-OCTANE/CU(111), 061902C.DAT.....	137
FIGURE A.5	N-OCTANE/CU(111), 070202C.DAT.....	138
FIGURE A.6	N-OCTANE/PB(111), 052802B.DAT.....	139
FIGURE A.7	N-OCTANE/1.5 MONOLAYERS C ₆₀ /PB(111)/CU(111), 050802C.DAT.	140
FIGURE A.8	N-OCTANE/BILAYER C ₆₀ /PB(111)/CU(111), 051002B.DAT	141
FIGURE A.9	N-OCTANE/8 LAYERS C ₆₀ /PB(111)/CU(111), 053002A.DAT.....	142
FIGURE A.10	METHANOL/MONOLAYER C ₆₀ /AG(111), 061903C.DAT.....	143
FIGURE A.11	METHANOL/MONOLAYER C ₆₀ /AG(111), 071603D.DAT..	144
FIGURE A.12	METHANOL/MONOLAYER C ₆₀ /CU(111), 082803C.DAT.....	145
FIGURE A.13	METHANOL/MONOLAYER C ₆₀ /CU(111), 101603A.DAT.....	146
FIGURE A.14	METHANOL/MONOLAYER C ₆₀ /AG(111), 121203A.DAT.	147
FIGURE A.15	METHANOL/MONOLAYER C ₆₀ /CU(111), 040804A.DAT.....	148

FIGURE A.16	METHANOL/BILAYER C ₆₀ /AG(111), 070103A.DAT.....	149
FIGURE A.17	METHANOL/BILAYER C ₆₀ /AG(111), 071703C.DAT	150
FIGURE A.18	METHANOL/BILAYER C ₆₀ /CU(111), 082903C.DAT.....	151
FIGURE A.19	METHANOL/BILAYER C ₆₀ /CU(111), 102203A.DAT.....	152
FIGURE A.20	METHANOL/BILAYER C ₆₀ /CU(111), 041304A.DAT	153
FIGURE A.21	KRYPTON/MONOLAYER C ₆₀ /AG(111), 020604A.DAT.....	154
FIGURE A.22	KRYPTON/BILAYER C ₆₀ /AG(111), 021104A.DAT	155
FIGURE A.23	KRYPTON/MONOLAYER C ₆₀ /CU(111), 040604A.DAT.....	156
FIGURE A.24	KRYPTON/BILAYER C ₆₀ /CU(111), 041204A.DAT.....	157
FIGURE A.25	METHANOL/CU(111), 101103A.DAT.....	158

CHAPTER 1: INTRODUCTION

1.1 A Brief History of Friction

When an object moves along a surface or through a viscous liquid or gas, the forces resisting its motion are referred to as friction. Frictional forces are nonconservative, converting the kinetic energy of materials in sliding contact to internal energy. Thus, if an object is given an initial velocity along a horizontal surface, the temperature of both the object and the surface upon which it slides will increase as the friction resisting its motion brings it to a stop. If an object is initially at rest, a minimum force must be applied to overcome “static friction,” giving rise to the familiar phenomenon of an object “jumping ahead” at the instant that sliding is initiated. Static friction, in contrast to kinetic friction, is associated with neither energy “loss” nor sample heating. It is entirely absent for bodies moving through viscous fluids, “viscous friction” being parameterized at low velocities by

$$F = m v/\tau. \quad (1.1)$$

Here v is the velocity of the object through the fluid, m is the object’s mass, and τ is a characteristic time for the object’s velocity to decay to $1/e$ of its initial velocity. Tribology (from the Greek word “tribos”, meaning “to rub”) is the study of friction, lubrication, and wear.

For objects sliding along solid surfaces, friction is generally well described on the macroscopic scale by Amontons’s Law:[1.1]

$$F = \mu N. \quad (1.2)$$

The “normal load” N in equation (1.2) is the force that presses surfaces in sliding contact together, and μ is the “coefficient of friction.” Amontons also reported that the friction force

was independent of the apparent area of contact: A small block experiences as much friction as a large block of the same material so long as their weights are equal. A third law, attributed to the French physicist Charles Augustin Coulomb[1.2], is frequently included with those of Amontons: The friction force is independent of velocity for ordinary sliding speeds.

The description of friction given above is not a new discovery. Da Vinci studied blocks sliding on inclined planes in ~1500 [1.3], Amontons published his studies of friction in 1699, and Coulomb published his results in 1785. Although the picture is a sufficient description of macroscale friction, it does not address the underlying mechanism of friction. Coulomb considered the possibility that friction was always associated with interfacial roughness, and disregarded it. There are many counterexamples to this argument, both theoretical and experimental. Automobile makers, for example, routinely find that the friction between bearings and cylinders is sometimes less if one of the surfaces is rougher than the other [1.4]. Furthermore, friction can increase if two surfaces are made smoother. In cold welding, for example, highly polished metals stick together firmly. Also, the stickiness of tape and other adhesives is not easy to explain with interfacial roughness.

As tribologists tried harder to understand the ultimate causes of friction, their studies demanded that they examine smaller and smaller length and time scales. For many years, however, the technology required to examine these length and time scales was not available.

In the 1950's, a research group at Cambridge headed by Bowden and Tabor made an important discovery. [1.5] They found that friction is independent of *apparent* (macroscopic) contact area, but is proportional to *true* contact area. The vast majority of surfaces are not atomically flat, and when two such surfaces touch, contact between them takes place only at

their asperities. The actual microscopic area of contact, A_c , is thus much less than the apparent area of contact A , perhaps by a factor of 10^4 . (See figure 1.1.) When the surfaces are forced to slide over each other, new contact regions are continuously formed, while others are severed. If the true area of contact is constant on average, and the contacting junctions all have the same shear strength s , then the friction force is:

$$F = A_c s \quad (1.3)$$

where s is the shear stress. The relations $F = A_c s$ and $F = \mu N$ can be linked, because as the normal load N increases, so does the true contact area A_c .

The dependence of friction on true contact area describes a macroscopic system's response to changes in load, but sheds little light on the physical origins of friction. This information is contained in the shear stress s , the frictional force per unit area of known contact. Bowden and Tabor's group explored this issue extensively, and at first believed that strong bonding at asperity contacts followed by wear was the physical mechanism underlying friction. [1.5] However, this idea was disproved in the 1970's by Tabor and Israelachvili. Israelachvili worked with a Surface Forces Apparatus (SFA) that he adapted for frictional measurements. (See figure 1.2 [1.6] for a picture and description of the SFA.) Using the SFA, Israelachvili and Tabor were the first to provide conclusive experimental evidence that friction could occur in the *total absence* of wear. [1.7,1.8]

Tomlinson published an early model, in 1929, of how friction might originate at the microscale. [1.9] In this model, when two surfaces slip across each other, wear-free friction can occur due to the vibration of the atomic lattices. The atoms close to one surface vibrate when the atoms in the opposing surface slip across them. These vibrations are called phonons, or sound waves. The phonons dissipate energy as heat, and this microscopic

process is manifested as friction. Motivated by Tomlinson's model, Bowden, Tabor and colleagues at Cambridge University attempted in the 1960's to detect evidence for the phononic contribution to friction, but failed to do so. The idea remained viable, however, as no alternate mechanism had presented itself.

Decades later, the concept of phononic friction was independently revisited by Sokoloff et al. in 1978, [1.10,1.11] and McClelland and coworkers in the 1980's, who rederived models similar to the original work of Tomlinson. McClelland, Mate and colleagues subsequently developed Lateral Force Microscopy (LFM) for studies of atomic scale friction in an effort to detect phononic mechanisms for friction. [1.12] (See figure 1.3 for a picture and description of LFM.) The technique has proven to be a revolutionary new probe for studies of atomic scale friction in particular, and nanoscale science in general.

Verification of phononic friction would first come from the combination of experiments done with a Quartz Crystal Microbalance (QCM) and the modeling of these experiments. The QCM had been used for decades for microweighing purposes, and was adapted for friction measurements in 1986-88 by Widom and Krim. [1.13,1.14,1.15] A QCM consists of a single crystal of quartz that oscillates in transverse shear motion (resonance frequencies are typically at 5-10 MHz) with very little internal dissipation (see figure 1.4 [1.16]). The oscillations are driven by applying an alternating voltage to thin metal electrodes deposited on the surface of the quartz, the electrodes generally prepared so as to present (111) metal orientations at their surfaces. Atomically thin films later adsorbed onto the QCM electrodes produce shifts in both the frequency and the quality factor Q , which are indicative of the degree to which the films are able to track the oscillatory motion of the underlying substrate. Friction in this geometry is well characterized by the "viscous friction

law”, $F/A_c = \eta v$, where v is the average sliding velocity of the adsorbed film constituents.

Characteristic slip times τ , and friction coefficients (i.e. shear stresses F/A_c per unit velocity) η , are determined via the relations [1.11]:

$$\delta(Q^{-1}) = 4\pi\tau(\delta f_o) \quad \eta = \rho_2/\tau \quad (1.4)$$

where ρ_2 is the mass per unit area of the adsorbate and δf_o is the frequency shift. Chapter 3 of this dissertation will cover the QCM in more depth.

1.2 Aims of the dissertation

There is much debate among theorists as to the causes of friction in any given experiment. However, it is generally agreed that the total friction coefficient can come from both electronic and phononic effects:

$$\eta = \eta_e + \eta_p \quad (1.16)$$

It is also generally agreed that the friction coefficient can be described by the equation:

$$\eta = \eta_{subs} + aU_o^2 \quad (1.17)$$

In this equation, η_{subs} is a damping term and aU_o^2 is the surface corrugation term. The surface corrugation term causes only phononic friction. The damping term is associated with both electronic and phononic friction, and it allows sliding energy to be dissipated within the substrate. Without the damping term, frictional energy is dissipated only via vibration of the adsorbate layers.

The primary aim of this dissertation is to conduct friction experiments on systems that have known surface properties, so that they can be accurately modeled. In Chapter 4, I will examine the effect of changing surface corrugation, U_o , on friction. In Chapter 6, I will examine the effect of the phononic damping by presenting QCM data for octane/Cu(111) and

octane/Pb(111). The phononic damping for octane on Cu(111) and Pb(111) has been measured.

1.3 Review of Prior Work

In 1991, Krim, Solina, and Chiarello reported Quartz Crystal Microbalance (QCM) measurements of the friction of krypton monolayers sliding on Au(111). [1.17] They prepared their Au(111) surfaces in ultra-high vacuum (UHV) and conducted the krypton adsorption *in situ* to ensure surface quality. The krypton adsorption isotherms were carried out at 77.4 K by submerging the adsorption chamber in a liquid nitrogen bath and allowing it to come to equilibrium. At 77.4 K, Kr condenses as a uniform film, 1 or 2 atoms thick. It starts condensation as a liquid, but solidifies as pressure is increased. They saw a 10.4 Hz frequency shift for Kr/Au(111) (originally the Au(111) sample had a resonance frequency of 5 MHz), which corresponds to a film coverage of 0.066 atoms/square angstrom. This is consistent with a liquid monolayer. They saw a phase transition “bump” in their frequency data, that caused a frequency shift to 12.5 Hz, which corresponds to coverage of 0.078 atoms/square angstrom, the solid phase coverage. This liquid/solid phase transition occurred at 1.45 Torr. They compared the slip time before and after the phase transition for Kr/Au(111), and found that solid Kr monolayers sliding on Au(111) had five times longer slip times (lower friction) than liquid monolayers of Kr. In other words, the surface was “slippery when dry.” See figure 1.5 for their frequency and slip time results.

In 1994, Cieplak, Smith, and Robbins modeled these interesting results. [1.18] Using standard molecular dynamics algorithms, they modeled mobile krypton atoms on a perfectly rigid gold substrate. The gold substrate provided a fixed periodic potential that acted on the

adsorbed krypton layer. The krypton-krypton interactions were modeled with a Lennard-Jones potential:

$$V(r) = 4\varepsilon[(\sigma/r)^{12} - (\sigma/r)^6] \quad (1.5)$$

Where r is atomic separation and $\varepsilon = 17$ meV and $\sigma = 0.357$ nm are characteristic energy and length scales for krypton, respectively. The krypton-gold interaction potential was modeled with a formula by Steele [1.19] for a Lennard-Jones adsorbate on a rigid substrate:

$$V_s(\mathbf{x}, z) = \varepsilon'[V_o(z) + fV_1(z) \sum_i \cos(\mathbf{G}_i \cdot \mathbf{x})] \quad (1.6)$$

Here \mathbf{x} is the position within the substrate plane, z is the distance above the first layer of substrate atoms, V_o is the average potential energy between adsorbate and substrate, V_1 describes the changes in adsorbate/substrate potential with respect to adsorbate position (otherwise described here as the surface corrugation), and \mathbf{G}_i are the reciprocal lattice vectors. They modified Steele's potential with a scaling factor, f , in order to allow the effect of the corrugation of the potential to be studied. (This makes the amplitude of the surface corrugation $U_o = fV_1$.) Also, a Lennard-Jones potential is too corrugated for metal surfaces, because the delocalized conduction electrons act to smooth the potential. Using this model, they then calculated the frictional force in two ways. First, they oscillated the adsorbates with an alternating force to simulate the vibrating QCM experiment, and then measured the adsorbate velocity. Second, they applied a constant force to the adsorbates and then measured the adsorbate velocity. In both of these simulations, the frictional force comes from the vibrations (phonons) of the krypton adsorbates as they slide atop the rigid gold substrate. With these simulations, they reproduced the 1991 experimental results of Krim et al.—they found that the solid krypton layer slipped longer on the substrate than the liquid. Their simulations included only one source of friction: phononic friction. Their results of

their model are shown in figure 1.6. Given the close match between their simulations and the QCM experiments, Robbins and colleagues concluded that phononic friction was “the major source of friction” for the krypton on Au(111) system. Many considered the combined QCM and numerical results to be the first definitive evidence for the existence of a phononic mechanism for friction. Another important finding of Cieplak and colleagues was that the slip time (τ) was proportional to corrugation of the potential and the lifetime of the phonons (t_{ph}) generated:

$$\tau \sim t_{ph} / f^2 \quad (1.7)$$

Hence a highly corrugated surface has a lower slip time (higher friction), and the damping or lifetime of the phonons generated by the sliding is directly proportional to the slippage.

In addition to phononic friction, there is another type of dissipation mechanism, electronic, that takes place in electrically conductive materials. In both electronic and phononic friction, kinetic energy associated with the sliding motion at an interface is transformed to heat. The heat is associated with temperature increases in both materials in sliding contact, and is reflected in the phonon populations therein. Phononic dissipative mechanisms involve direct transfer of energy into the phonon populations. In contrast, electronic mechanisms involve energy transfer into the conduction electrons before transfer to the phonon populations. In one proposed mechanism for electronic friction, the presence of another surface or an adsorbate and the sliding across the metal substrate causes excitations of the conduction electrons near the interface. The excitations generate electron-hole pairs. Electron-hole pairs in metals (in contrast to semiconductors) have very brief lifetimes. When these electron-hole pairs relax, the excess energy is dissipated as heat, and

the temperature concomitantly rises. The mechanism is quite distinct from the forces associated with static charge buildup on insulating materials.

In 1996, Daly and Krim reported on the sliding friction of xenon monolayers and bilayers on Ag(111). [1.20] Like the krypton on Au(111) experiment described previously, the Ag(111) films were prepared in UHV, and the xenon adsorption isotherm was conducted *in situ*, to ensure surface quality. The isotherms were collected at 77.4 K by submerging the adsorption chamber in liquid nitrogen and allowing it to come to equilibrium. See figure 1.7 for their isotherm data. At 77.4 K, xenon forms an incommensurate triangular solid monolayer film with a nearest neighbor spacing of 0.452 nm (5.624 atoms/nm²). With increasing xenon adsorption, the monolayer film will allow more atoms by compressing until it reaches a nearest neighbor spacing of 0.439 nm (5.97 atoms/nm²). This spacing is the same as bulk solid Xe(111). As more xenon is adsorbed, a second layer will form on top of the monolayer that is commensurate with the compressed monolayer. Daly and Krim assumed that the two layers move in unison while sliding. They observed that the friction force per unit area required to slide the two-layer thick Xe film was 27% greater than that required to slide the monolayer film. See figure 1.8. Due to their intriguing result, there have been several subsequent efforts to explain and to model the sliding of Xe/Ag(111).

Models of the Xe/Ag(111) system by Persson and Nitzan [1.21] included both phononic (η_p) and electronic (η_e) contributions to friction, as described by the following equation:

$$\eta = \eta_e + \eta_p \quad (1.8)$$

They used the following equation to obtain the sliding friction of particle i , mass m , at position \mathbf{r} , of Xe/Ag(111). The particles are moving under the influence of an external force \mathbf{F} and a stochastically fluctuating (thermal) force \mathbf{f} :

$$m\ddot{\mathbf{r}}_i + m\eta\dot{\mathbf{r}}_i = -\frac{\partial U}{\partial \mathbf{r}_i} - \frac{\partial V}{\partial \mathbf{r}_i} + \mathbf{f}_i + \mathbf{F} \quad (1.9)$$

They modeled the Xe-Xe interactions as a sum of Lennard-Jones pair potentials.

$$V(r) = \varepsilon[(r_o/r)^{12} - 2(r_o/r)^6] \quad (1.10)$$

Here, ε and r_o are characteristic energy and length scales, respectively, and r is the atomic separation. The interaction of a xenon atom with a Ag(100) substrate (Persson and Nitzan modeled the Ag(100) substrate, but claim the general results should not be dependent on the detailed form of the potential) is described by:

$$U(r) = E_b[e^{-2\alpha(z-z_o)} - 2e^{-\alpha(z-z_o)}] + U_1[2-\cos(kx)-\cos(ky)]e^{-\alpha'(z-z_o)} \quad (1.11)$$

Here, E_b is adsorbate binding energy, $k=2\pi/a$, where a is the lattice constant of the substrate, $2U_o$ is the surface corrugation or barrier height, and α is the decay constant. Persson and Nitzan used a barrier height of $U_o = 2 U_1 = 1.9 \text{ meV}$, based on experimental measurements of the phonon modes for the Xe/Cu(111) system [1.22]. This estimate of the surface corrugation assumes that there is some interaction between the adsorbate and substrate phonons, i.e. that the Cu(111) substrate is not perfectly rigid. In their paper, Persson and Nitzan state that this is the correct assumption, and that the model of Cieplak et al. [1.18] was flawed because they modeled the Au(111) substrate as perfectly rigid and allowed for no adsorbate/substrate phonon interaction. Persson and Nitzan also use a thermostat to hold the temperature at 77.4 K. They based their electronic friction measurements on both theory and experiment, and found an electronic friction coefficient of $5 \times 10^8 \text{ s}^{-1}$. Their model predicted a very low

contribution to the friction from phonons, and attributed almost all of the friction in the Xe/Ag(111) system to electronic friction. Daly and Krim's result, the increase in friction from the monolayer to the bilayer, was reported to be caused by an increase in the electronic friction. They reported that the second layer pushes the xenon closer to the silver surface, thus increasing the van der Waals contribution to the electronic friction.

Tomassone and colleagues [1.23], however, stated that the friction in the Xe/Ag(111) system was primarily due to phononic friction. They reported that the increased number of possible vibrational modes that dissipate energy is greater for a bilayer than a monolayer, and that this is the cause of the increase in friction. They used molecular dynamics simulations with a sum of Lennard-Jones pair potentials to model the Xe-Xe interaction, as did Persson and Nitzan. They differed from Persson and Nitzan in their model of the xenon atom interacting with the Ag(111) substrate. They instead used a potential similar to that used by Cieplak et al. [1.18] This is the potential originally derived by Steele [1.19] (see equation 1.6) to model the interaction between a xenon atom and the silver substrate. Steele's potential is rougher than the actual interaction, so Tomassone and colleagues modified the Steele potential to include the electronic screening of the corrugation potentials by the conduction electrons. They state that their maximum peak-to-peak surface corrugation is $U_o = 2.7$ meV. As opposed to most nanotribological models, they used a thermostat to establish equilibrium, but turned it off while monitoring the properties of the system. They did this because sometimes thermostats have the side effect of artificially damping the atomic vibrations, which artificially increases friction. Using this model, which included only phononic friction, they were able to successfully fit the xenon on Ag(111) experiment of Daly and Krim. See figure 1.9. However, to prove that phononic friction dominates, Tomassone and

colleagues also carried out simulations using the same electronic friction damping constants used by Persson and Nitzan. With the modified Steele corrugation potential and Persson and Nitzan's model for electronic friction, they still found that 75% of the friction in the Xe/Ag(111) system was phononic friction, and concluded from this that phonons dominate.

Persson has suggested that the electronic component of friction, μ_{eh} , is related to the surface resistivity of an adsorbate-substrate system [1.24] via:

$$\mu_{eh} = n^2 e^2 d \Delta\rho / mn_a \quad (1.12)$$

Here, n is the number of conduction electrons per unit volume, e is the electron charge, d is the thickness of the metal film, $\Delta\rho$ is the adsorbate-induced increase in film resistivity, m is the adsorbate mass, and n_a is the number of adsorbates per unit area in direct contact with the adsorbate. This is derived for a viscous friction law of the following form.

$$F_{fric} = m \mu_{eh} v \quad (1.13)$$

Where F_{fric} is the force of friction and v is the sliding speed.

Schumacher et al. [1.25] employed Eq. (5.1) to infer friction coefficients for a range of adsorbates, and found the slip times to be in the range $10^{-9} - 10^{-12}$ seconds. The values compared favorably with slip times measured by means of QCM. In an attempt to quantify the relative contributions of electronic friction to phononic friction, Dayo and Krim compared the electronic friction calculated from electrical resistivity measurements to total friction taken from QCM measurements for Xenon on Ag(111) at 77 K. [1.26] They observed the resistivity of the Ag(111) film to increase monotonically with the adsorption of the Xe, up to coverages of one monolayer. Above one monolayer, the resistivity increased only very slightly. However, the friction force per unit area required to slide the two-layer thick Xe film was 27% greater than that required to slide the monolayer film. [1.20] Using

equation 1.12, they calculated the electronic contribution to friction and compared it to the total friction obtained from the QCM, and reported the electronic contribution to be at most 30% of the total for Xe/Ag(111).

A paper by Liebsch, Goncalves and Kiwi claimed that both electronic and phononic friction were required to accurately model the Xe/Ag(111) experiment of Daly and Krim. [1.27] They believe this because electronic friction is not highly coverage dependent, as are the experimental results of Daly and Krim. They pointed out that nanotribological models are strongly dependent on knowledge of the corrugation amplitude of the Xe/Ag interaction potential, a number that has not been precisely determined experimentally. Without knowledge of the corrugation amplitude, they argued, it is not possible to predict the relative contribution of phononic vs. electronic friction with any accuracy. In their model, they therefore varied both the corrugation amplitude and electronic contribution to friction using the following equation:

$$\eta = \eta_{el} + a U_o^2 \quad (1.14)$$

Here η is the total friction coefficient, η_{el} is damping due to the electronic contribution to friction, a is a constant dependent on temperature and coverage, and U_o is the corrugation of the adsorbate/substrate interaction potential. Using their model, they concluded that both phononic and electronic friction were necessary to accurately model the Xe/Ag system. As they varied the values of the surface corrugation, they found that if their model included a surface corrugation that was too large, electronic friction did not show up. They used this to explain the results of Tomassone and colleagues. Also, if the value for the electronic friction coefficient was too large, naturally electronic friction dominated in that model. They claimed that Persson and Nitzan fell into this category. They argued that since both the

surface corrugation and the electronic friction coefficient have not been conclusively determined experimentally, it is very difficult to accurately model the friction for Xe/Ag(111). Robbins and Muser later made a small modification to equation 1.14. [1.28]

$$\eta = \eta_{subs} + a U_o^2 \quad (1.15)$$

Here, η_{subs} is a damping term that includes both electronic and phononic friction. By including a contribution to the damping from phonons, Robbins and Muser are allowing the phononic frictional energy to also be dissipated within the substrate.

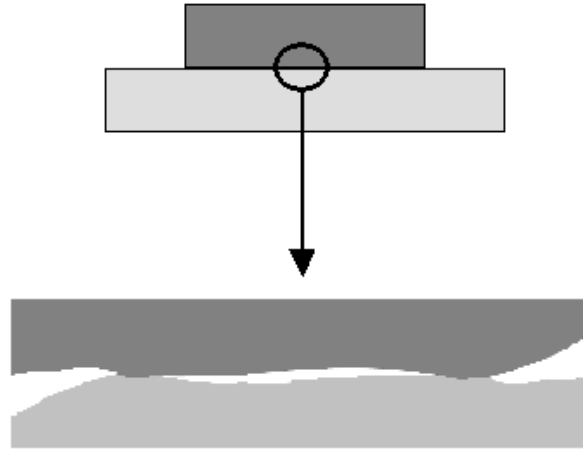


Figure 1.1 At top, we see that the apparent area of contact. In the enlarged region, we see the actual area of contact. The surfaces are only touching at the asperities.

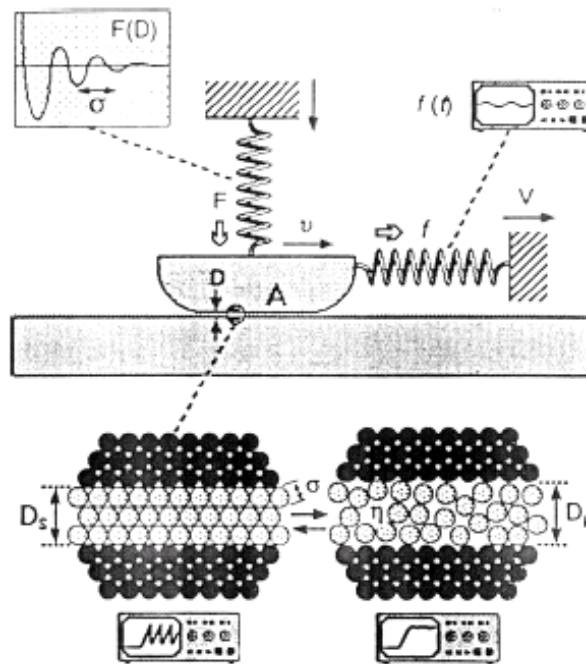


Figure 1.2 Surface Forces Apparatus schematic [1.6]. The SFA has two cleaved mica surfaces, which are atomically flat. Lubricants or films go between the mica surfaces, as is shown in the magnified region at bottom. The normal and frictional forces between the surfaces can be measured, as is shown schematically in the springs.

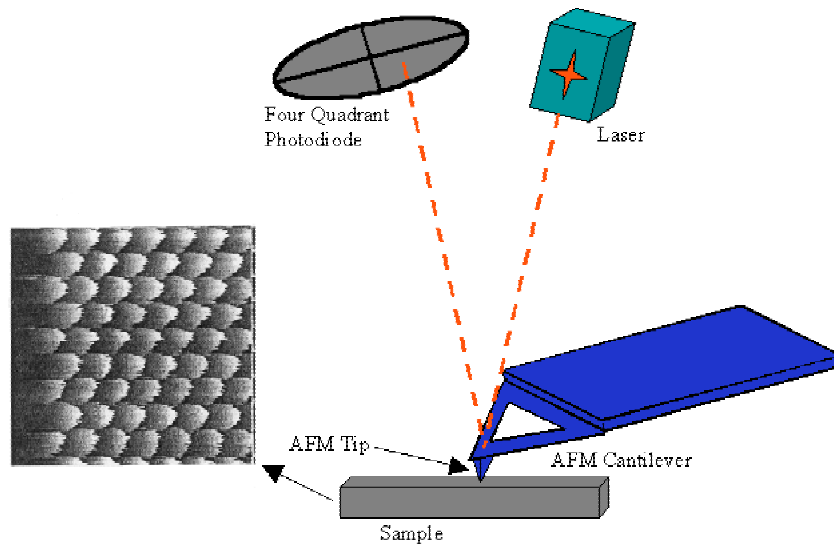


Figure 1.3 Lateral (Atomic) Force Microscope schematic. The LFM consists of a sharp tip mounted at the end of a compliant cantilever. For LFM measurements, the tip is held in contact with the sample surface while it is raster scanned across the sample surface. The frictional forces which act on the tip are determined by measuring the angular deflections of the cantilever, via the laser and four quadrant photodiode.

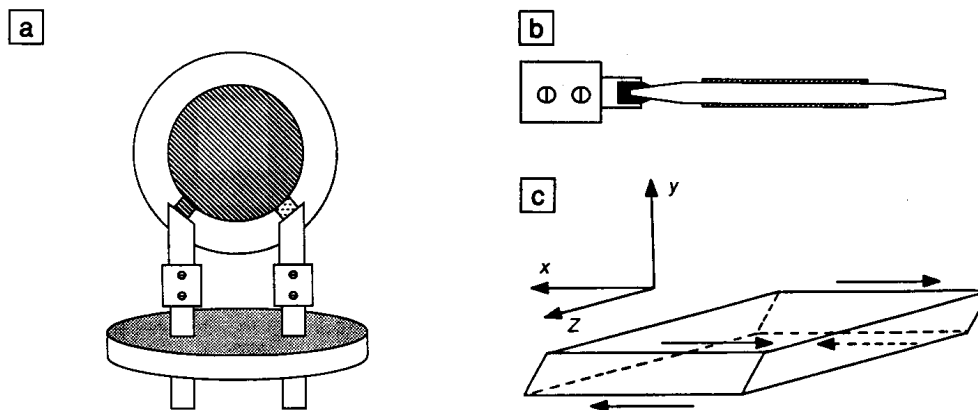


Figure 1.4 Quartz Crystal Microbalance schematic [1.16]. A QCM consists of a single crystal of quartz that oscillates in transverse shear motion (resonance frequencies are typically at 5-10 MHz) with very little internal dissipation. The oscillations are driven by applying an alternating voltage to thin metal electrodes deposited on the surface of the quartz. Atomically thin films later adsorbed onto the QCM electrodes produce shifts in both the frequency and the quality factor Q , which are indicative of the degree to which the films are able to track the oscillatory motion of the underlying substrate.

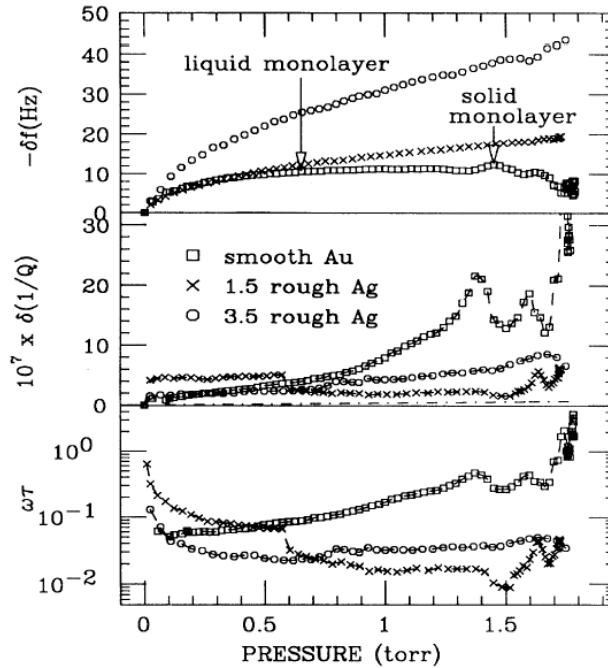


Figure 1.5 Frequency shift (top), change in quality factor (middle), and slip time (bottom) data for Krypton on Au(111) and Ag(111) at 77 K [1.17].

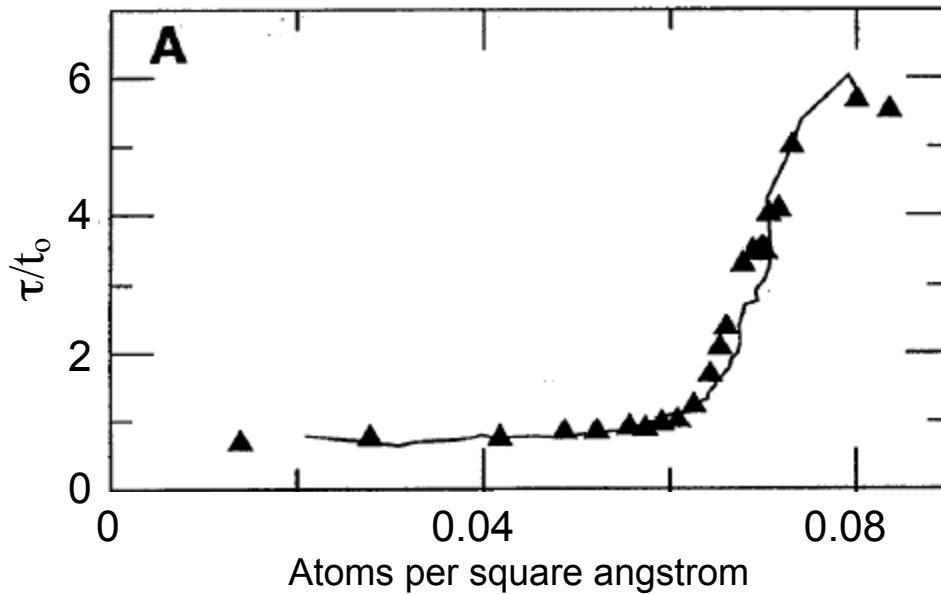


Figure 1.6. The solid line shows the experimental data for Kr/Au(111) for Krim et al. The triangles represent the theoretical model of Cieplak et al., which is a model of the Kr/Au(111) system. The model, which includes only phononic friction, fits the experiment very well.[1.18]

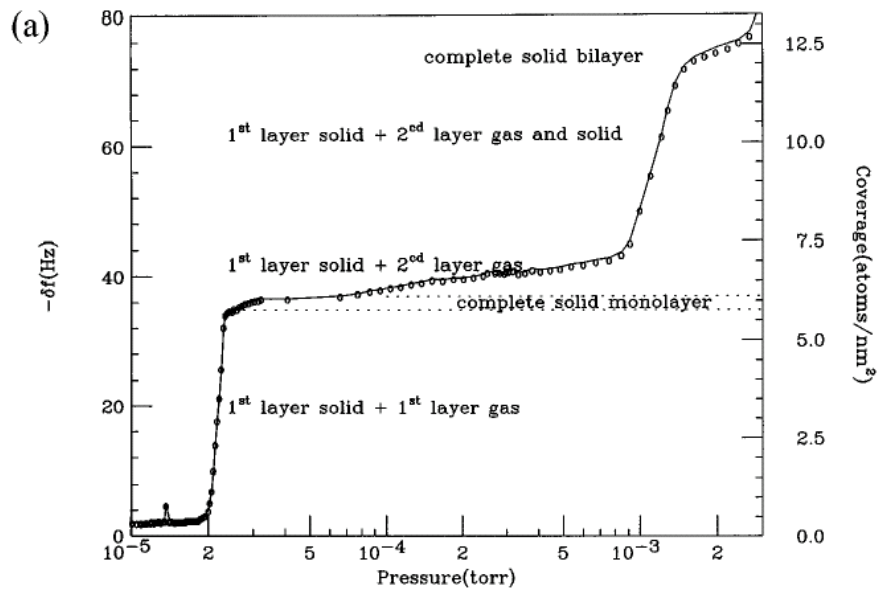


Figure 1.7 Frequency shift and coverage for xenon on Ag(111) at 77 K. [1.20]

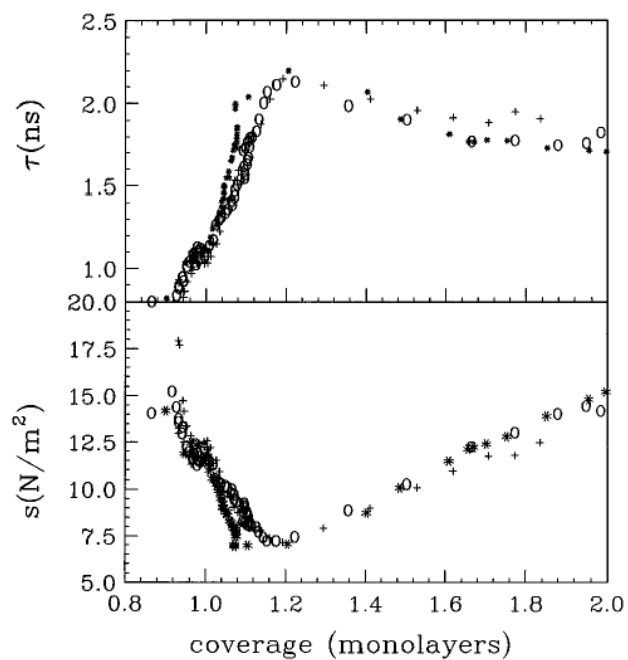


Figure 1.8 The slip time (top) and shear stress (bottom) for xenon sliding on Ag(111) at 77 K. [1.20] Note that the shear stress required to slide two layers is 27% greater than that required to slide one layer.

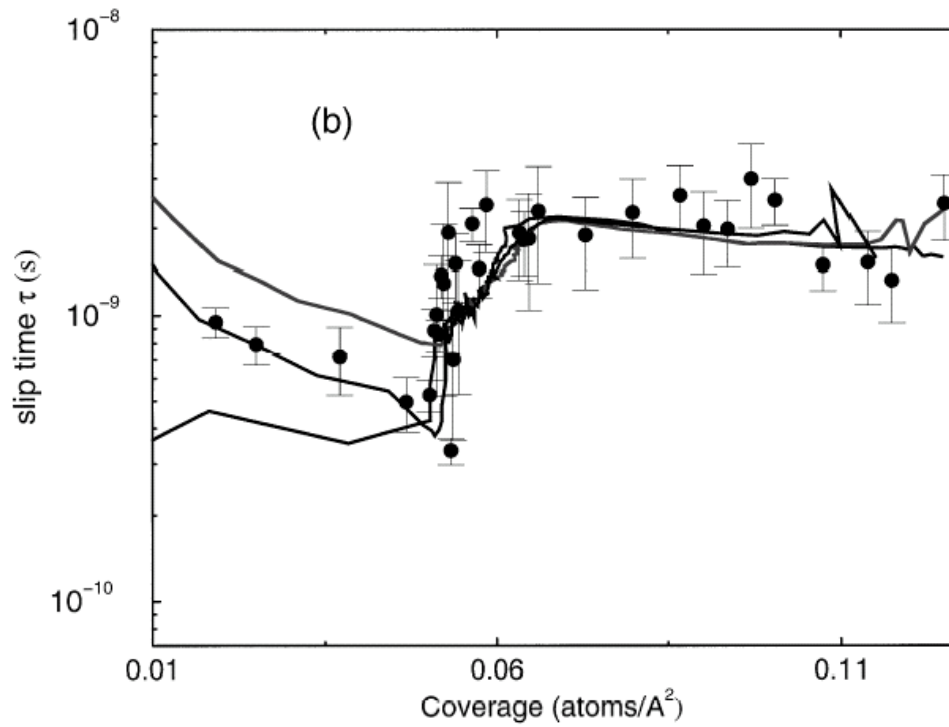


Figure 1.9. The solid lines represent the Xe/Ag(111) slip time data from Daly and Krim. The circles represent the fit to the data from the model by Tomassone et al. The model fits the data extremely well, using less than 30% electronic friction. [1.23]

CHAPTER 2: PREDICTING THE VISCOUS COEFFICIENT OF FRICTION

Tribologists are not the only research community to have pondered energy dissipation mechanisms at moving interfaces. An entirely distinct surface science community emerged in the late 1980's, members of which studied both phononic and electronic contributions to energy dissipation within the context of small vibrational motions of atoms on surfaces.

Whenever atoms or molecules adsorb on surfaces, new vibrational modes will emerge which are not present in either an isolated surface or the adsorbate alone. The modes which appear include both "internal", (stretching or torsional vibrations within a molecule) and "external" modes whereby the entire molecule or atom moves as a whole with respect to the surface.

See figures 2.1 and 2.2 for examples of internal and external modes. These phonon modes for adsorbate-substrate systems have characteristic energies that can be measured by Helium Atom Scattering (HAS) and related spectroscopies. [2.1-2.5] They can also measure the line width (defined as the lifetime or damping) of adsorbate vibrations, which is indicative of the rate at which the energy of the phonon mode is dissipated into heat.

Frustrated, or damped, translational modes both parallel and perpendicular to the substrate have been measured. Perpendicular modes (S-modes or FT_z modes) mainly probe the energy and damping of the interaction between the adsorbate and substrate. Low frequency (~ 10 meV, or $\sim 2.4 \times 10^{12}$ Hz) FT_z modes indicate that the adsorbate is physisorbed, and high frequency (higher than physisorbed modes by a factor of ~ 10 or more) FT_z modes indicate chemisorption, for example. [2.2] Modes parallel to the surface (T-

modes) probe the curvature or corrugation of the adsorbate-substrate interaction potential [2.3-2.5] and the commensurability between adsorbate and substrate. [2.5]

From the information given by the phonon dispersion curves gleaned from HAS and related spectroscopies, it should be possible to predict and explain the friction for a given adsorbate-substrate system. For example, if we use equation 1.17, $\eta = \eta_{subs} + a U_o^2$, as a description of the friction coefficient, we can use parameters obtained from HAS experiments as estimates for η_{subs} and U_o . The frequency of the frustrated translational modes is related to the surface corrugation, U_o . It is also hypothesized that the damping of the frustrated translational modes is related to the damping term η_{subs} .

L.W. Bruch used the energies (frequencies) of the frustrated translational phonon modes to determine the surface corrugation (interaction potential) for krypton on graphite, however his results can be generalized to any given adsorbate-substrate combination by simply changing the parameters. [2.6] Bruch used the following equation to describe the interaction potential:

$$V(\mathbf{r},z) = V_o(z) + \sum_g V_g(z) \exp(i\mathbf{g} \cdot \mathbf{r}) \quad (2.1)$$

Here, V_o and V_g are the amplitudes of the constant and periodic components of the adsorbate-substrate potential, \mathbf{g} are the reciprocal lattice vectors, z is the height of the adsorbate with respect to the substrate, and \mathbf{r} is a vector in the plane of the substrate.

According to Bruch, the amplitude of the periodic component of the adsorbate-substrate potential could be estimated as following. The sign of V_g depends on the adsorption site of the adatom with respect to the substrate lattice and is determined on a case by case basis.

For $V_g < 0$:

$$\omega_z = \left(\frac{V_o + 6V_g}{m} \right)^{1/2} \quad \omega_{\parallel} = g_o \left(\frac{-3V_g}{m} \right)^{1/2} \quad (2.2)$$

For $V_g > 0$:

$$\omega_z = \left(\frac{V_o - 3V_g}{m} \right)^{1/2} \quad \omega_{\parallel} = g_o \left(\frac{1.5V_g}{m} \right)^{1/2} \quad (2.3)$$

Here, ω_z and ω_{\parallel} are the frequencies of the frustrated translations perpendicular and parallel to the substrate, respectively, and m is the adsorbate mass. The reciprocal lattice vector, g_o , can be estimated by using:

$$g = \frac{4\pi}{d_{nm}\sqrt{3}} \quad (2.4)$$

Here d_{nm} is the nearest neighbor distance of the substrate atoms. The surface corrugation, U_o , can then be estimated using $U_o = -8V_g$, for $V_g < 0$, and $U_o = V_g$, for $V_g > 0$.

Persson [2.7] claims that the damping term, η_{subs} , can be estimated using HAS and related spectroscopies. For adsorbates on the (100) surface of an fcc crystal, the motion of adsorbate i is given by:

$$m\ddot{\mathbf{r}}_i + m\eta\dot{\mathbf{r}}_i = -\frac{\partial U}{\partial \mathbf{r}_i} - \frac{\partial V}{\partial \mathbf{r}_i} + \mathbf{f}_i + \mathbf{F} \quad (2.5)$$

Here, m is the mass of the adsorbate, U is the periodically corrugated adsorbate-substrate interaction potential, V is the adsorbate/adsorbate interaction potential, \mathbf{f}_i is a fluctuating force due to thermal effects, and \mathbf{F} is an external force. The friction or dissipation term, η , is a matrix:

$$\begin{matrix} \eta_{\parallel} & 0 & 0 \\ 0 & \eta_{\parallel} & 0 \\ 0 & 0 & \eta_{\perp} \end{matrix} \quad (2.6)$$

According to Persson, η is caused by coupling of the adsorbate and substrate phonon modes and also by the excitation of electron-hole pairs in the substrate by the adsorbate. Persson states, “Information about η can be deduced from infrared spectroscopy and inelastic helium atom scattering spectroscopy since η determines the line width of the adsorbate vibrations if inhomogeneous broadening and pure dephasing processes can be neglected.” Persson relates the line width, γ , of the adsorbate vibrations to η in the following way:

$$\hbar\eta = \gamma \quad (2.7)$$

Therefore, according to various theorists, we should be able to predict the coefficient of friction for a given adsorbate-substrate combination if the phonon dispersion curves have been measured. One can determine the corrugation of the adsorbate-substrate interaction potential by measuring the frequencies of the frustrated translations. [2.6] In addition, it is hypothesized that one can determine the damping of the sliding energy of the adsorbate into the substrate by measuring the line width of the adsorbate vibrations. As mentioned above, one primary aim of this dissertation is to explore the validity of this hypothesis, which I will do in Chapter 6.

Chapters 1 and 2 functioned as a literature review and a general introduction to nanotribology and predicting the viscous coefficient of friction. Chapter 3 covers experimental techniques and procedures, and the experimental apparatus used to acquire my data. Chapters 4, 5, 6, 7 and 8 are self-contained. Chapter 4 describes the effects of the changing surface corrugation on sliding friction. Chapter 5 describes QCM experiments with krypton sliding on various surfaces. Chapter 6, as stated above, explores the effects that

changing the damping coefficient of a perpendicular phonon mode has on sliding friction.

Chapter 7 concerns C_{60} , and the effects that the molecular rotation of C_{60} has on sliding friction. Chapter 8 is also a C_{60} experiment (previously published in the Journal of Physics, Condensed Matter) which cross-references various techniques to measure nanoscale friction.

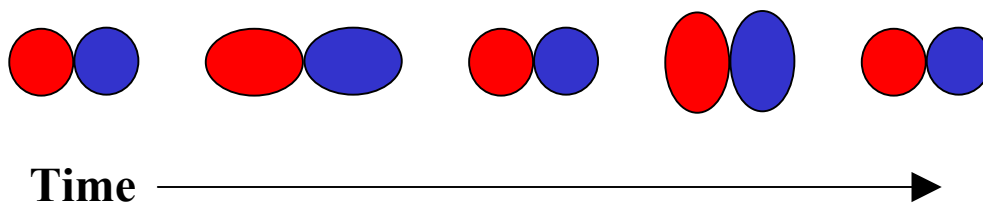


Figure 2.1 A free molecule vibrates with internal vibrational modes of given energy. The red and blue diatomic molecule above is in a stretching and compression mode of vibration.

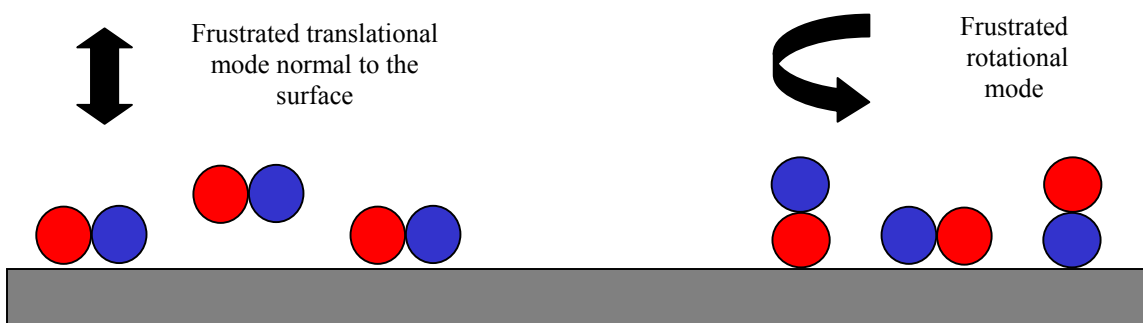


Figure 2.2 When the molecules are adsorbed to a surface, new vibrational modes are created. These modes are external modes of the molecule with respect to the surface. These modes can be classified as frustrated translational or rotational modes of the molecule either perpendicular or parallel to the surface. They have characteristic and measurable frequencies and lifetimes. On the left of the figure above, we see the molecule translate perpendicularly to the surface. On the right, we see the molecule rotate with respect to the surface.

CHAPTER 3: EXPERIMENTAL METHODS AND APPARATUS

This chapter will describe in detail the Quartz Crystal Microbalance (QCM), how the QCM measures friction, and the experimental apparatus with which I acquired my data. The gas adsorption studies described in this work require ultra-high vacuum (UHV) conditions to ensure sample quality and integrity and also purity of the gases studied. Nearly all data taken to prepare this dissertation was acquired using QCM in UHV as described here.

3.1 Quartz Crystal Microbalance (QCM)

3.1.1 General Description and Common Uses

The Quartz Crystal Microbalance (QCM) has been used for decades for microweighing purposes [3.1,3.2]. A schematic of the QCM is shown in Figure 3.1. Quartz is a crystalline form of silicon dioxide, SiO_2 . For temperatures below 573°C , the phase is α -quartz, which is a piezoelectric material. [3.3]

Our QCM consists of a thin disk ($< 1\text{mm}$) of single quartz crystal. By coating the two faces of the QCM with metal electrodes and applying an alternating voltage, the QCM can be made to mechanically oscillate due to its piezoelectric properties. Its quality factor (Q) is relatively high, near 10^5 . Because of their high frequency stability and high Q, QCM can detect mass changes as small as 1 pg/cm^2 . It is this extreme sensitivity to small mass changes that has made the QCM so popular as a rate monitor, or microbalance. In our lab, we focus on the use of QCM as a probe for sliding friction. This technique was developed in 1986-88 by J. Krim and Widom [3.4]. Through acoustic impedance calculations, they were able to

show that if the shear stress between the film and the QCM surface is below 10^3 N/m^2 , then the film will slip atop the QCM surface enough to be detected by monitoring the changes in the QCM resonance frequency and amplitude.

The QCM's used in this work are exclusively AT-cut crystals. This means that the crystal oscillates in transverse shear mode, as shown in Figure 3.2. [3.5] Figure 3.3(a) shows the crystallographic axes of the quartz crystal. The Z-axis is chosen to be parallel to the quartz trigonal axis. It is so called because it has three symmetric diagonal axes perpendicular to it. The x-axis is chosen parallel to one of the diagonal axes. The piezoelectric effect depends greatly on direction, for example, if stress is applied along the Z-axis, no electric signal is generated. Therefore, the way the quartz disk is cut has a great impact on the crystal frequency as well as its stress and temperature responses. For example, the AT- and BT-cuts are oriented at angles of $\theta = 35^\circ 15'$, figure 3.3(b), and $\theta = -49^\circ$ respectively from the ZX-plane. These crystal cuts are used for the high-frequency thickness-shear mode of oscillation. Since the AT-cut crystals have zero temperature coefficient near room temperature, they became the most popular choice for most of the applications. Also, they exhibit higher frequency stability and mass sensitivity.

3.1.2 Relationship between Mass Uptake and Frequency shift

Sauerbrey investigated the quantitative relation between mass deposited on the QCM electrodes and change in its oscillation frequency [3.6, 3.7]. Consider an AT-cut crystal. When an alternating voltage is applied across its electrodes, mechanical shear waves are generated across its thickness. Standing waves are established if the thickness of the crystal, t , is an odd integer of $\lambda/2$ where λ is the wavelength of the induced

wave. Then, the fundamental frequency f_0 is given by:

$$f_0 = \frac{v_q}{\lambda} = \frac{v_q}{2t} \quad (3.1)$$

where v_q is the speed of wave propagation in quartz. Differentiating and rearranging both sides, one obtains:

$$\frac{df_0}{f_0} = - \frac{dt}{t} \quad (3.2)$$

which can be rewritten in terms of the mass of the quartz as:

$$\frac{df_0}{f_0} = - \frac{dm_q}{m_q} \quad (3.3)$$

Sauerbrey made the assumption that for thin films adsorption onto QCM crystals, the mass of the added film could be treated as a small perturbation of the quartz oscillator's mass, i.e., dm_q in the last equation could be replaced by m_f . This is valid for $m_f \ll m_q$, and also for a film evenly distributed over the active area of the crystal. Using equations 3.1 and 3.3 and the fact that $m_q = \rho_q A t$, where A is the area of the quartz crystal and ρ_q is its density, one obtains:

$$\Delta f = - 2 \frac{(m_{\text{film}} / A)}{\rho_q v_q} f_0^2 \quad (3.4)$$

For quartz, $\rho_q = 2.65 \text{ g/cm}^3$ and $v_q = 3.34 \times 10^5 \text{ cm/s}$. Taking into consideration that in a typical experiment the adsorbed film is deposited on both electrodes of the QCM, the right hand side is multiplied by a factor of two, yielding:

$$\Delta f = - 4.52 \times 10^{-6} \left(\frac{m_{film}}{A} \right) f_0^2 \quad (3.5)$$

Applying this equation for one monolayer deposited on 8 MHz crystal one finds $\Delta f = -37.1$ Hz for xenon, -27.1 Hz for krypton, -10 Hz for methanol, and -14.3 Hz for octane. The gas parameters are given in table 3.1. [3.8]

There are four conditions that need to be satisfied in order to apply equation 3.4 and 3.5 properly. These conditions are (a) the mass of the deposited film is much smaller than the mass of the crystal, (b) the film covers the active area of the QCM uniformly, (c) the film is non-dissipative, and (d) the film adheres perfectly to the QCM. Other approaches have been developed for more general cases of mass adsorption but they all reduce to Sauerbrey's formula for small mass uptakes.

3.1.3 The Quality Factor

The quality factor “ Q “ is a dimensionless quantity that has been used in both mechanical and electrical oscillating systems to represent the degree of damping of the oscillator. It is defined as:

$$Q = 2\pi \frac{\text{Energy stored in one cycle}}{\text{Energy lost in one cycle}} \quad (3.6)$$

Energy is stored in the system by the driving mechanism and it is dissipated due to internal friction and external damping forces. From the definition of the Q factor, it is obvious that its inverse is the dissipation factor, $D = Q^{-1}$. Therefore, a high Q means low loss and high frequency stability. The maximum attainable Q of a crystal is a function of the diameter and surface curvature of the blank quartz and is inversely proportional to the frequency of oscillation.

When mass is added to the oscillator the overall dissipation is just the sum of the individual dissipations in the mass plus the quartz:

$$\frac{1}{Q} = \frac{1}{Q_q} + \frac{1}{Q_m} \quad (3.7)$$

As more mass is added, acoustic losses in the material increase and Q decreases further. When the Q factor of the QCM becomes exceedingly low, its oscillation will not be sustained and the crystal will cease to function. Changes in Q can be monitored via changes in the QCM amplitude, as well as the ring down of the QCM (see section 3.3 for details on the QCM ring down.)

3.1.4 Sliding Friction Measurements

In this section, the use of the QCM to study the interfacial sliding will be discussed. This technique, developed by Krim and Widom [3.4], is based on the theory that if a film is sitting on a solid substrate that is sliding back and forth, interfacial slippage, and thus sliding

friction could be probed. The acoustic impedance presented by the film to the substrate motion serves as the probe to the interfacial slippage.

3.1.5 Acoustic Impedance

(a) Acoustic Impedance of a Viscous Film

Consider a film of thickness d , with bulk density ρ_{3f} and bulk viscosity η_{3f} , lying on a flat, solid surface oscillating in plane with velocity $u = u_0 e^{-i\omega t}$. The motion of the solid surface will cause shear waves to propagate through the film.

Taking the z -direction to be perpendicular to the solid surface, and the x -direction to be parallel to the motion of the surface, the film can be described by the Navier-Stokes equation for a viscous, incompressible fluid [3.9]

$$\rho_{3f} \frac{\partial v_x(z,t)}{\partial t} = \eta_{3f} \frac{\partial^2 v_x(z,t)}{\partial z^2} \quad (3.8)$$

where $v_x(z,t)$ is the component of the film velocity in the direction of the motion of the solid surface. (From now on, the subscripts 2 and 3 will refer to surface and bulk values respectively, while f and v will refer to the film and vapor phases.) Assuming that the film does not slip on the solid surface and that its upper surface is free to move without any resistive force, the solution of the problem, for frequency f , is given by:

$$v_x(z,t) = u(t) \frac{\cos k(d-z)}{\cos(kd)} \quad (3.9)$$

where the dispersion relation is given by $k=(1+i)(\omega\rho/2\eta)^{1/2}$. From the stress tensor component $\sigma_{zy} = \eta(\partial v/\partial z)_{z=0}$, one obtains the acoustic impedance, $Z = \sigma_{zy} / v$, presented by the film to the motion of the solid plane as:

$$Z_f = R_f - i X_f = \eta_{3f} k \tan(kd), \quad \text{where } k^2 = i \frac{\omega\rho_{3f}}{\eta_{3f}} \quad (3.10)$$

The resistive component R is proportional to the energy dissipation, while the reactive component X is proportional to the inertia of the oscillator.

Stockbridge [3.10] has shown that the total frequency and quality factor shifts of the QCM are related to the total impedance presented to it by the relation:

$$\delta\left(\frac{1}{Q}\right) = \frac{4R_{tot}}{\omega\rho_q t_q}, \quad \delta\omega = \frac{2X_{tot}}{\rho_q t_q} \quad (3.11)$$

where ρ_q and t_q are the density and thickness of the quartz crystal respectively. These equations assume, as explained above, exposure of both electrodes of the crystal to the mass deposited. Of course, if only one side is exposed, the right hand side of the equations must be divided by 2.

For very thin films, such that $|kd| \ll 1$, the dissipative part of equation 3.10 vanishes and the acoustic impedance reduces to:

$$Z_f = -i X_f = -i\omega\rho_{3f}d = -i\omega\rho_{2f}, \quad \text{for } |kd| \ll 1 \quad (3.12)$$

Substituting this result into equation 3.11 leads to Sauerbrey's result for the mass-frequency relationship given by equation 3.4.

(b) Acoustic Impedance of a 3-D Gas

When the QCM is brought from vacuum to a gaseous environment, the acoustic impedance presented to the oscillator has contributions from the shear impedance of the gas, and mass uptake if gas adsorption occurs.

Consider first the case when there is no adsorption. The acoustic impedance of a purely viscous gas (with bulk density ρ_{3v} and bulk viscosity η_{3v}) to shear wave propagation is given by [3.9]

$$Z_v = R_v - i X_v = (1-i)\sqrt{\pi\rho_{3v}\eta_{3v}f} \quad (3.13)$$

The reactive loading of the gas is equivalent to an increase in inertia of the oscillator and leads to frequency shifts which could be calculated by substituting equation 3.13 into equation 3.11:

$$\frac{\delta f}{f_0} = \frac{\sqrt{\pi\rho_{3v}\eta_{3v}f}}{2\pi\rho_q v_q} \quad (3.14)$$

At low pressures, the relaxation time τ_r of the gas particles after collision with the vibrating crystal becomes commensurate with the period of oscillation. The gas therefore is no longer a simple viscous fluid but must be regarded as a viscoelastic. Its viscosity becomes a function of frequency according to [3.11]

$$\eta_{3v}^* = \frac{\eta_{3v}}{1 + i\omega\tau_r} \quad (3.15)$$

The acoustic impedance Z_v^* of the viscoelastic gas is then given by [3.10]

$$Z_v^* = R_v^* - iX_v^* \quad (3.16)$$

where

$$R_v^* = \sqrt{\pi\rho_{3v}\eta_{3v}f} \sqrt{\frac{\omega\tau_r}{1+(\omega\tau_r)^2} \left(\sqrt{1 + \frac{1}{(\omega\tau_r)^2}} + 1 \right)}$$

$$X_v^* = \sqrt{\pi\rho_{3v}\eta_{3v}f} \sqrt{\frac{\omega\tau_r}{1+(\omega\tau_r)^2} \left(\sqrt{1 + \frac{1}{(\omega\tau_r)^2}} - 1 \right)}$$

For pressures above 300 Torr, $\omega\tau_r \ll 1$, the relaxation argument becomes unimportant and equation 3.16 degenerates into the classical viscous impedance given by equation 3.13.

(c) Acoustic Impedance of a Film-Vapor System

If the gas adsorbs on the crystal under equilibrium conditions, the shear waves generated by the oscillator will diffuse away from the electrodes, through the film, and into the viscous gas. The acoustic impedance at the film-substrate boundary will therefore have contributions from both the adsorbed film and the 3-D vapor. Assuming there is no slippage at the film-substrate boundary, the acoustic impedance is given by:

$$Z_{fv} = Z_{3f} \tanh(\Psi + \gamma d)$$

where,

$$\begin{aligned} \tanh(\Psi) &= \frac{Z_{3v}}{Z_{3f}} \\ Z_{3v} &= (1-i)\sqrt{\pi\rho_{3v}n_{3v}f} \\ Z_{3f} &= (1-i)\sqrt{\pi\rho_{3f}n_{3f}f} \\ \gamma &= Z_{3v} = (1-i)\sqrt{\frac{\rho_{3f}\omega}{2n_{3f}}} \end{aligned} \quad (3.17)$$

If the adsorbed film is sufficiently thin such that $|kd| \ll 1$, then the acoustic impedance reduces to:

$$Z_{fv} = -i\omega\rho_{2f} \left[1 - \left(\frac{Z_{3v}}{Z_{3f}} \right)^2 \right] + Z_{3v}, \quad |kd| \ll 1. \quad (3.18)$$

This equation can be further simplified by noting that the acoustic mismatch factor

$\left[1 - \left(\frac{Z_{3v}}{Z_{3f}} \right)^2 \right]$ is close to unity in most cases. Then:

$$Z_{fv} = -i\omega\rho_{2f} + Z_{3v} = Z_f + Z_v \quad (3.19)$$

The damping effects of the film and the gas vapor on the oscillator can therefore be separated and we can write the frequency and quality factor shifts as:

$$\begin{aligned} \delta(\omega) &= \delta(\omega)_f + \delta(\omega)_v = \frac{X_f}{\rho_q t_q} + \frac{X_v}{\rho_q t_q} \\ \delta\left(\frac{1}{Q}\right) &= \delta\left(\frac{1}{Q}\right)_f + \delta\left(\frac{1}{Q}\right)_v = 0 + \frac{R_v}{\omega\rho_q t_q} \end{aligned} \quad (3.20)$$

3.1.6 Damping Due to Interfacial Slippage

The film impedance given in equation 3.19 assumes the 'no-slip' condition. Bruschi and Mistura [3.12] calculated the effect of film slippage on the mechanical impedance presented to the QCM. If the film slips on the surface of the electrodes, energy dissipation due to interfacial friction will introduce additional impedance $1/\eta_2$ in parallel to the 'no-slip' impedance of the film given in equation 3.19. The total acoustic impedance is then given by:

$$\frac{1}{Z_{tot}} = \frac{1}{\eta_2} + \frac{1}{Z_{fv}} \quad (3.21)$$

Solving for the dissipative and reactive terms gives [3.12]:

$$\begin{aligned} \frac{X_{tot}}{R_{tot}^2 + X_{tot}^2} &= \frac{\omega\rho_2 + X_v}{R_v^2 + (\omega\rho_2 + X_v)^2} \\ \frac{R_{tot}}{R_{tot}^2 + X_{tot}^2} &= \frac{R_v}{R_v^2 + (\omega\rho_2 + X_v)^2} + \frac{1}{\eta_2} \end{aligned} \quad (3.22)$$

To calculate the slip time, τ , we solve for η_2 from equation 3.22 and use:

$$\tau = \frac{\rho_{2f}}{\eta_2} \quad (3.23)$$

The slip time τ characterizes the decay of the total film momentum with respect to the substrate. It is a direct measure of how much slippage occurs at the film-substrate boundary. Note that it is an average over all the particles in the film, since not all of them are slipping in the same direction at a given time.

By equation 3.11, we can use the change in inverse quality factor and the change in frequency shift to calculate the total dissipation R_{tot} and total reactance X_{tot} . Then, using equation 3.23, we can calculate the interfacial slippage and the slip time, τ . Hence, the slip time τ can be determined from frequency and quality factor measurements of the QCM.

Bruschi and Mistura's approach is a small correction to the earlier efforts of Krim and Widom [3.4]. Instead of equation 3.21, Krim and Widom used the following:

$$Z_{tot} = Z_v + \frac{Z_f \eta_2}{Z_f + \eta_2}$$

In the limit of low vapor density, the approaches of Bruschi and Mistura vs. Krim and Widom give the same result. As the vapor density increases, the Bruschi and Mistura approach gives a small correction (10% - 15%) to the Krim and Widom approach.

3.1.7 Experimental Determination of Q

Measurement of interfacial slippage requires simultaneous recording of both quality factor shifts and resonance frequency shifts.

The QCM can be described as a damped driven harmonic oscillator. Its equation of motion is written as:

$$m \frac{d^2 x}{dt^2} + b \frac{dx}{dt} + kx = F_0 \cos(\omega t) \quad (3.24)$$

where m is the total mass of the crystal and film, c is the damping constant, and $\sqrt{k/m}$ the natural frequency of the crystal. The solution of equation 3.24 is $x = A \cos(\omega t - \phi)$. Substitute this solution into equation 3.24 one obtains the expression for the amplitude as:

$$A(\omega) = \frac{F_0}{\sqrt{(k - m\omega^2)^2 + c^2 \omega^2}} \quad (3.25)$$

and the phase angle:

$$\phi = \arctan \left(\frac{c\omega}{k - m\omega^2} \right) \quad (3.26)$$

Using the following relations:

$$\omega_0 = \sqrt{k/m} \quad \text{and} \quad Q = \frac{m\omega_0}{c}$$

Equation 3.25 can be rewritten as:

$$A(\omega) = \frac{F_0/m}{\sqrt{(\omega_0^2 - \omega^2)^2 + \left(\frac{\omega_0\omega}{Q}\right)^2}} \quad (3.27)$$

Since the QCM is driven at its resonance frequency, i.e., $\omega \cong \omega_0$, the above equation reduces to:

$$A(\omega_0) \cong \frac{F_0}{m} \left(\frac{Q}{\omega_0^2} \right) \quad (3.28)$$

The variation of the amplitude with both frequency and quality factor are then given by:

$$\frac{\partial \left(\frac{1}{A} \right)}{\partial \left(\frac{1}{Q} \right)} = \frac{m}{F_0} \omega_0^2 \quad \text{and} \quad \frac{\partial \left(\frac{1}{A} \right)}{\partial \omega} = \frac{2m}{F_0} \left(\frac{2\omega_0}{Q} \right) \quad (3.29)$$

Substituting our experimental values, $\omega \approx 10^8$ Hz and $Q \approx 10^5$, we get:

$$\frac{\partial\left(\frac{1}{A}\right)}{\partial\left(\frac{1}{Q}\right)} \cong 10^{13} \frac{\partial\left(\frac{1}{A}\right)}{\partial(\omega)} \quad (3.30)$$

This means that changes in the amplitude of oscillation are essentially independent of changes in frequency. Therefore, amplitude changes may be used to monitor changes in the quality factor " Q " directly.

3.1.8 Factors affecting the QCM frequency

Generally temperature, pressure and stress affect the vibrational motion of the QCM by inducing changes in the crystal's dimensions, density and elastic stiffness. These effects need to be taken into consideration and corrected for in order to isolate the damping due to film-substrate interactions alone which is the focus of interest in this study.

(a) Temperature

Temperature changes caused by internal and ambient conditions produce frequency shifts whose magnitudes depend on the crystal cut. These frequency shifts can result from changes in the crystal's dimensions due to thermal expansion. Mainly, however, they are due to temperature-induced changes in the crystal's elastic properties.

Stockbridge [3.13] obtained the relation between the thermal shift ΔT and the induced frequency shift δf :

$$\frac{\delta f}{f_0} = \beta a \Delta T \quad (3.31)$$

where a is the depth of the surface layer having a temperature difference ΔT from the center of the plate, and β is the coefficient of linear expansion divided by twice the thickness of the crystal. However, it is not easy to compensate for temperature effects by using this equation since the temperature of the crystal is not always well known.

For AT-cut crystals, the increase in the elastic modulus with temperature is relatively small and their frequencies are essentially temperature-independent in the range -60 to 100°C. Beyond this range, however, the temperature coefficients are large and slight temperature changes can lead to large frequency shifts. Therefore, we have to be very careful to ensure that the system maintains thermal equilibrium during measurements. This includes giving the crystal ample time to stabilize after evaporation, mounting it on a stainless steel holder which can act as a heat sink, using the lowest possible voltage to drive the oscillator circuit. This is especially important for isotherms acquired at low temperatures, such as the krypton and xenon isotherms.

(b) Gas Pressure

Stockbridge [3.10] investigated the effect of pure hydrostatic pressure on the QCM. This effect is different from the damping effects because of gas density and viscosity.

At low pressures, the effect of hydrostatic pressure is negligible. However, above 1 mTorr, the resonance frequency increases linearly with pressure due to the changes in the

elastic moduli of the quartz. This effect has a nearly linear effect with temperature and is given by [3.10]:

$$\frac{\Delta f}{f_0} = (13.5 - 0.015 T) \times 10^{-10} P \quad (3.32)$$

where T and P are measured in Kelvin and Torr, respectively. On the contrary, the hydrostatic pressure has no significant effect on the quality factor of the microbalance.

(c) Stress

The resonance frequency of the quartz oscillator may change appreciably because of high-applied stresses. These frequency shifts induced by such stresses are determined by EerNisse [3.14]. Assuming that the incremental film stress results in a uniform lateral stress in the quartz crystal, the frequency shift as a result of the film stress is given by:

$$\frac{\delta f}{f_0} = -2.75 \times 10^{-11} T_q \quad ; \quad T_q = -\frac{2}{t_q} \int_0^{t_f} T_f dz \quad (3.33)$$

where t_q and t_f are the quartz crystal and film thickness, respectively, both are measured in meters. And T_q , measured in N/m^2 , is the uniform biaxial lateral stress produced in the quartz crystal by the incremental lateral stress T_f initiated in the adsorbed film. This equation could be used to correct for stress effects only if stress levels are actually known. The factor of 2 in the integral equation accounts for exposure for both sides of the QCM.

(d) Mass uptake and Slippage

Mass uptake and interfacial slippage is our main concern in this study. The frequency shift produced by the adsorbed film is a result of both mass uptake and interfacial slippage, and is given by:

$$\Delta f_{film} = \frac{\Delta f_{massloading}}{1 + (\omega\tau)^2} \quad (3.34)$$

For $\omega\tau \ll 0.1$, the slip time is short and the film is rigidly coupled to the oscillator so that the mass sensitivity is at its maximum and the dissipation is small. When $\omega\tau \gtrsim 0.2$, the slip time is long and the film decouples from the motion of the oscillator and the mass sensitivity drops. In some of the work in this dissertation, for example the slippage of xenon on Cu(111), the frequency shift is much reduced because of this effect.

3.1.9 Net frequency Shift

The measured frequency shift of a quartz oscillator in an actual experiment is merely the sum of the frequency shifts induced by all factors discussed above, i.e.,

$$\Delta f = \Delta f_{film} + \Delta f_{gas\ viscosity} + \Delta f_{temperature} + \Delta f_{gas\ pressure} + \Delta f_{stress} \quad (3.35)$$

In these measurements, the frequency shifts induced by hydrostatic pressure are routinely subtracted away, while those due to gas viscosity are easily calibrated. Generally, the magnitude of the stress effects is generally negligible for most of the adsorbed films.

3.2 Experimental Hardware

The experimental hardware, including ultra-high vacuum equipment, QCM packaging, control electronics, and QCM drive circuits, is discussed in great detail in Steve Winder's doctoral dissertation "QCM Measurements of Sliding Friction of Inert Gas Films on Lead, Copper, Nickel, and Graphene Surfaces." [3.15] Interested readers should refer to that work for an in depth discussion of the hardware; only a brief overview will be given here.

My experimental system has several subsystems, specifically a sample preparation area for thermal evaporation of metal films, a sample holding cell in which the crystal is housed during the adsorption isotherms, and a gas dosing area that contains the experimental gases. The main chamber contains both the sample preparation area and the sample holding cell. The pressure in the main chamber is controlled by an ion pump. The gas dosing area is separated from the main chamber by a leak valve. During an adsorption isotherm, this valve is cracked, allowing the experimental gas to leak in slowly. The pressure in the gas dosing area is held at high vacuum by a diffusion pump backed by a mechanical pump. The main chamber is also separated from the high vacuum area by a gate valve; by opening the gate valve the main chamber can be pumped on by the diffusion pump. Labeled pictures of the experimental chamber are shown in figures 3.4 and 3.5.

In these experiments, as in many surface science experiments, ultra-high vacuum is required to ensure that the isotherms and friction measurements reflect those of pure gases and not that of contaminant layers. The metal films in this work were prepared in UHV conditions by thermal evaporation, and then the adsorption isotherms carried out *in situ*

unless otherwise noted. Our thermal evaporation methods are very simple. The source metal is held in a tungsten boat between electrical feedthroughs. On the order of 100 amps of current is passed through the boat to heat it resistively. The metal is then evaporated onto the QCM. C₆₀ films in this work were sublimed on top of the metal films in the same manner.

Many of the experiments in this work, specifically the krypton and xenon measurements, were conducted at low temperatures. This was accomplished by immersion of the sample holding cell in a liquid nitrogen bath, which is in equilibrium with its vapor at 77.4 K. The QCM was allowed to come to equilibrium before the krypton or xenon was adsorbed. The sample holding cell is attached to the main chamber via a bellows. It is therefore simple to submerge the sample holding cell in the liquid nitrogen bath. (See figure 3.5 for a picture of the sample holding cell.)

The pressures in these experiments are monitored in by multiple pressure gauges. An ion gauge is used to measure chamber pressures below 1×10^{-4} Torr. For pressures between 1×10^{-6} and 1×10^{-3} Torr during an adsorption isotherm, a spinning rotor gauge is used. For pressures between 1 mTorr and 1000 Torr during experimental runs, two Baratron pressure gauges are used.

3.3 Electronics and QCM Calibration

We drive the QCM with a Pierce oscillator circuit. See figure 3.6 for a schematic of the circuit. [3.16] The Pierce oscillator circuit is powered by a DC power supply at 10 V. The circuit drives the QCM at its resonance frequency with great stability. In equilibrium conditions, the crystal can be held at a constant frequency of roughly 8 MHz with a drift of +/- 2 Hz for several hours.

For our experiments, we use two Pierce oscillator circuits. One drives the sample QCM, and the other drives a reference QCM. The two signals are then fed into a mixer, and the difference frequency and amplitude can be measured with a frequency counter and a digital multimeter. The frequency counter and digital multimeter are shown in figure 3.7, as are the control electronics for the ion pump and pressure gauges. The data from the pressure gauges, frequency counter, and digital multimeter is then interfaced with the computer, which records the gas adsorption isotherms.

The data is analyzed via the “slip” program. The details of the analysis are discussed at length in section 3.1. As discussed in section 3.1.6, the change in crystal amplitude A is proportional to the change in quality factor Q :

$$\delta\left(\frac{1}{Q}\right) = C\delta\left(\frac{1}{A}\right) \quad (3.36)$$

In order to get meaningful data from the QCM, we must determine the proportionality constant, C . We call this the QCM calibration. In this dissertation, my most common method of calibration was to conduct an isotherm with a non-adsorbing gas with known acoustic impedance (such as nitrogen or helium). I then plotted change in inverse amplitude vs. change in dissipation factor, and found the slope of the line. This slope was the proportionality constant, C . An example of this technique is shown in figure 3.8.

The crystal can also be calibrated using the ring down method. In this method, the characteristic decay time of the QCM oscillation is measured, and used to determine the absolute rate of damping of the QCM. This is done by cutting off the QCM driving circuits and taking snapshots of the subsequent exponential decay of the QCM oscillation. The decay time (the time it takes for the QCM to reach $1/e$ of its initial amplitude) is then measured.

Calibration can be accomplished by taking 2 snapshots of the QCM exponential decay: with and without a known damping to the QCM oscillation. Here, the known damping is a resistor hooked up in series with the QCM. The addition of the resistor causes significant changes in decay time of QCM oscillation and output voltage of the Pierce circuit. The calibration constant C is calculated using the following formula [3.15]:

$$C = \frac{\delta R}{\delta(1/A)} = \frac{\rho_q v_q}{4f_o} \frac{(1/\tau_2 - 1/\tau_1)}{(1/A_2 - 1/A_1)} \quad (3.37)$$

Here, τ_2 and τ_1 are the decay times and A_2 and A_1 are the voltage amplitudes with and without the resistor. ρ_q and v_q are the density and speed of sound in an AT-cut QCM oscillating at frequency f_o . See figure 3.9 for a picture and schematic of the ring down method.

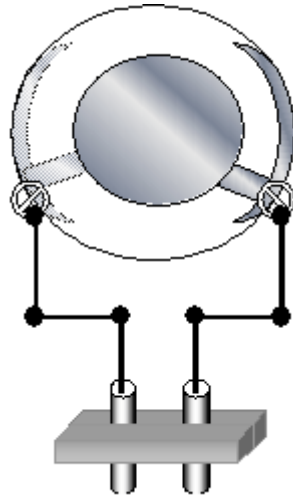


Figure 3.1. QCM Schematic. The QCM is a thin quartz disk. Metal electrodes are present on both sides of the disk in a keyhole design. Spring clips secure the QCM to the holder and provide electrical contact to the metal electrodes. Leads are attached to the spring clips. An alternating voltage is applied to the leads that causes our QCM's to oscillate.

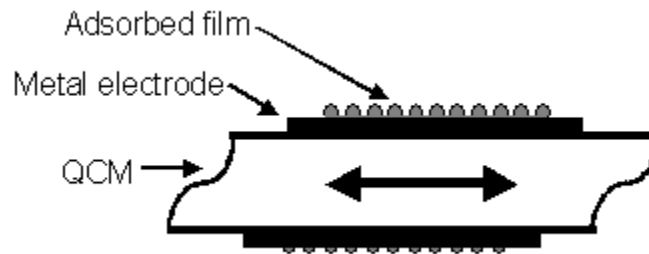


Figure 3.2. Side view of QCM when it is oscillating in tranverse shear mode. The applied alternating voltage causes the faces of the QCM to move laterally in opposing directions.

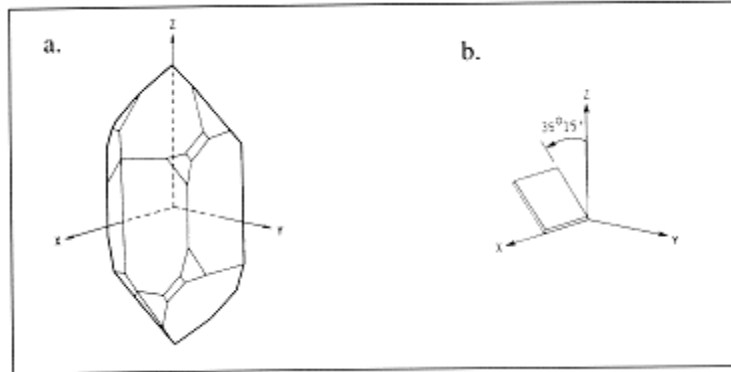


Figure 3.3a. Quartz crystal axes. b. AT-cut crystal. [3.5]

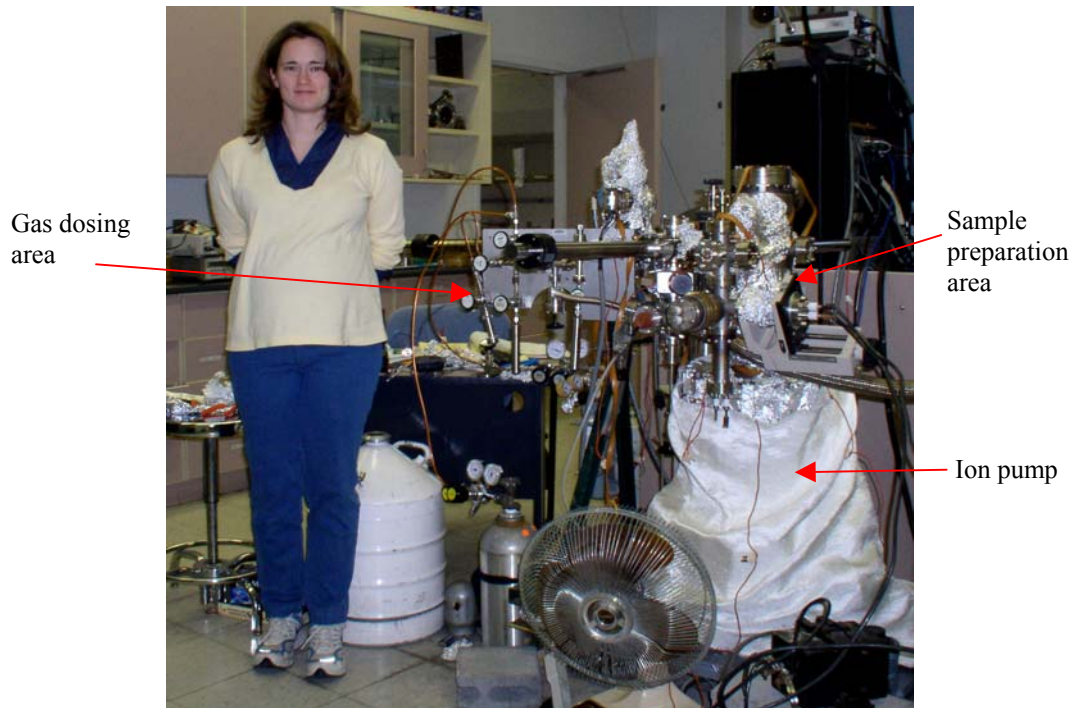


Figure 3.4. Picture of UHV chamber.

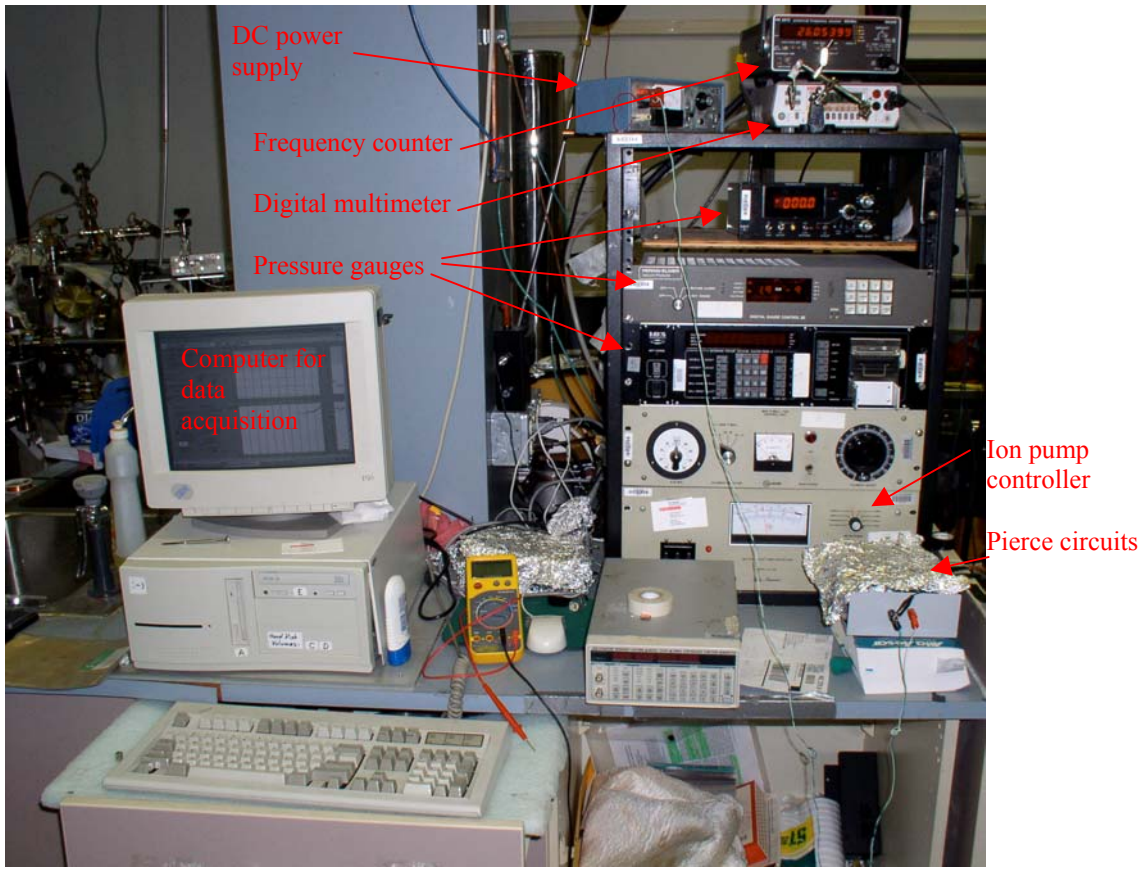


Figure 3.7. Picture of control electronics.

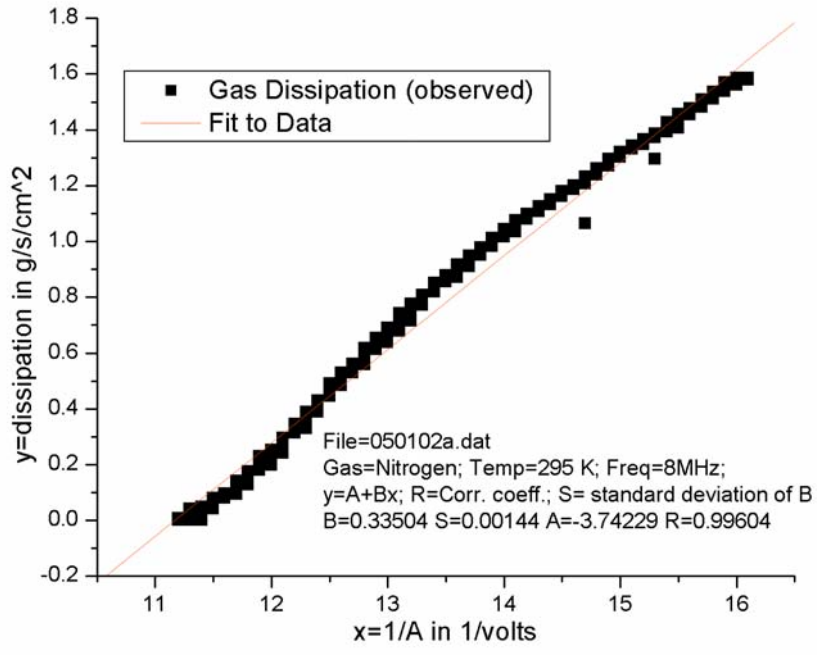


Figure 3.8. A typical example of a QCM gas calibration. In this case, the gas used was nitrogen, at room temperature, on an 8 MHz crystal. The calibration constant, C , was 0.335 ± 0.0014 .

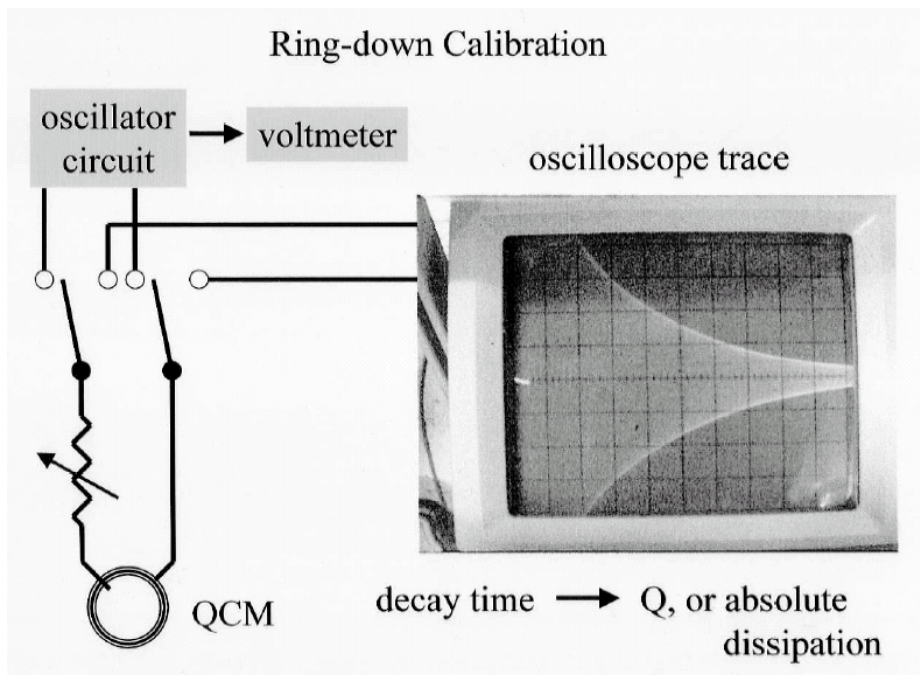


Figure 3.9. Schematic and picture of ring down calibration method. The QCM is placed in series with the resistor, and the power to the drive circuits is cut. A snapshot, shown at right, is then taken of the exponential decay of QCM oscillation, and the characteristic decay time is extracted from the curve.

Table 3.1. Gas parameters used to analyze adsorption data in this work. Atomic weights were obtained from the periodic table of elements. Molecular diameters were calculated using densities and molar weights, and assuming spherical molecules. For octane, which is not spherical, the rectangular area of the molecule was calculated, and an equivalent spherical area found to obtain molecular diameter. Critical viscosities were obtained from Yaws [3.8]. Critical temperatures were obtained from the CRC Handbook of Chemistry and Physics [3.9].

Gas	Weight (AMU)	Molecular diameter (cm)	Critical viscosity (Poise)	Critical temperature (K)
Xenon	131.3	4.1×10^{-8}	2.25×10^{-4}	287.8
Krypton	83.8	3.6×10^{-8}	1.85×10^{-4}	210.1
Octane	114.2	6.4×10^{-8}	1.05×10^{-4}	568.7
Methanol	32.0	5.0×10^{-8}	1.67×10^{-4}	512.6

CHAPTER 4: IMPACT OF ATOMIC CORRUGATION ON SLIDING FRICTION AS PROBED BY QCM

**manuscript in preparation for submission to Physical Review Letters*

T. Coffey, S.M. Winder, and J. Krim

Physics Department, Box 8202

North Carolina State University

Raleigh, NC 27695-8202

Abstract

We report a quartz crystal microbalance (QCM) study of the slippage of solid xenon films at 77 K on Cu(111), Ni(111) and graphene/Ni(111) substrates. These systems have similar lattice spacing, but varying amplitudes of adsorbate-substrate interaction potential or surface corrugation, U_o . QCM slip time (τ) data show that $\tau \sim U_o^{-2}$, consistent with numerical simulations. For comparison, we show slippage data for Xe/C₆₀, since U_o should be distinctly larger for Xe/C₆₀.

4.1 Introduction

Friction is a ubiquitous physics problem with no simple model that explains it from a fundamental point of view. The quest to understand friction has led to experiments conducted in extremely simple and well-characterized systems at the nanoscale. Krim, Solina, and Chiarello [4.1] and Daly and Krim [4.2] used the quartz crystal microbalance (QCM) to conduct friction experiments of noble gases sliding on metal substrates in ultra-high vacuum (UHV), specifically for krypton sliding on Au(111) and xenon sliding on Ag(111). The friction for these systems obeys the viscous friction law,

$F = (m/\tau)v$; $F/A = S = \eta v$. (Here, m , τ , and v are the mass, slip time, and velocity of the adsorbates, and A , S , and η are the area, shear stress, and friction coefficient for the systems.)

These experiments generated much excitement and there were many attempts to model them [4.3-4.6]. The models included energy dissipation via both electronic and phononic effects.

It has been proposed that the viscous coefficient of friction, η , can be described in the following way [4.7]:

$$\eta = \eta_{subs} + aU_o^2 \quad (4.1)$$

Here η_{subs} is the damping, or dissipation, of adsorbate sliding energy within the substrate (from both phononic and electronic friction), a is a constant depending on temperature and lattice spacing, and U_o is the surface corrugation. In all of the models cited above, the interaction of the noble gas atoms with the metal substrate was modeled with sinusoidal functions, generating a corrugated adsorbate-substrate potential. The surface corrugation, U_o ,

is the amplitude of the periodic function describing the changes in adsorbate-substrate potential with respect to adsorbate position.

All of the modeling efforts cited above successfully fit the data from the QCM friction experiments. However, the theorists disagreed about the contribution to friction from phononic vs. electronic effects. These disagreements were primarily because the damping and surface corrugation terms in equation 4.1 have not been determined for the systems studied. The surface corrugation of adsorbate-substrate systems can be determined using helium atom scattering (HAS) and related spectroscopies [4.8, 4.9], has been measured for Xe/Cu(111) [4.9] and Xe/graphite [4.10]. Surface diffusion measurements have revealed the surface corrugation for Xe/Ni(111) [4.11]. (Table 4.1. [4.9-4.14]) Since Cu(111) and Ni(111) have very similar lattice spacings, they are ideal for testing equation 4.1, since numerical simulations of equation 4.1 have used a single lattice spacing [4.3, 4.6].

We report here a QCM study of the sliding of solid monolayers of xenon at 77.4 K along Cu(111), Ni(111), graphene/Ni(111), and C₆₀/Ag(111) surfaces. The graphene substrate was grown epitaxially on top of a Ni(111) substrate so as to have the same lattice spacing as Ni(111), rather than that of natural graphite [4.16].

We also compare the systems with known corrugation values to Xe/Ag(111) and Xe/C₆₀/Ag(111), whose corrugation values are not precisely known. The data for Xe/Ag(111) has been previously published, as discussed above. [4.2] The nearest neighbor spacing of C₆₀ is very large compared to the other systems, 1 nm. Its corrugation has not been measured. However, it is expected to have a distinctly larger corrugation than the other systems studied, due to the large size of the C₆₀ molecules.

4.2 Experimental

The microbalance crystals for these studies were overtone-polished 8 MHz AT-cut quartz that had quality factors near 10^5 . For the Cu(111) sample, the copper was deposited atop a QCM with a 20 nm titanium pre-coat, to prevent roughening of the copper electrode. [4.17] The base pressure of the vacuum system ranged from 8×10^{-11} to 5×10^{-10} Torr. Thermal evaporation was then used to deposit 60 nm of 99.999% pure Cu, producing a mosaic structure with a (111) fiber texture [4.18]. C_{60} substrates were prepared by thermally evaporating 2 monolayers of C_{60} atop an 80 nm thick Ag(111) electrode on a blank QCM. Like the Cu(111), the Ag(111) was prepared via thermal evaporation of 99.999% pure Ag, and the C_{60} was deposited immediately after the Ag(111) deposition.

The 80 nm Ni(111) films were deposited using an electron beam evaporator in UHV onto a blank QCM. The deposition rate was several angstroms per second. The graphene (a graphitic layer one atom thick) samples were prepared by heating the Ni(111) samples to 500 C while dosing the sample with 10^{-6} Torr of carbon monoxide. The nickel then acts as a catalyst, forming a pure graphitic carbon onto the nickel surface and sending byproducts of carbon dioxide and nickel carbide into the gas phase. [4.16] All samples were immediately transferred *in situ* to the adsorption cell where they were electrically connected to an external Pierce oscillator circuit. They were then chilled to 77.4 K by submersion in a liquid nitrogen bath.

After the samples had come to thermal equilibrium, we exposed them to research grade xenon gas [4.19] while frequency and amplitude shifts were monitored with increasing pressure. The frequency shifts (δf) are proportional to the mass per unit area of the film that

tracks the QCM motion. [4.20]. If there is much slippage of the film, then some of the mass of the film will be decoupled from the oscillation of the substrate, and the frequency shift will be reduced [4.21].

$$\frac{\delta f_{\text{massloading}}}{f} = -\frac{2\rho_f t_f}{\rho_q t_q} \quad \delta f_{\text{film}} = \frac{\delta f_{\text{massloading}}}{1 + (\omega\tau)^2} \quad (4.2)$$

Here, ρ_f and t_f are the density and thickness of the adsorbed film, and ρ_q (2.65 g/cm³) and t_q (0.021 cm for $f = 8\text{MHz}$) are the density and thickness of the QCM. The change in amplitude (A) is proportional to the change in quality factor (Q): $\delta(Q^{-1}) = c\delta(A^{-1})$. To determine the proportionality constant, c , we calibrate our samples with helium gas adsorption after completion of the xenon uptake measurements or via a “ring down” method. [4.22] Frequency and quality factor shifts can also be caused by gas pressure, tensile stress, and temperature, however these effects were negligible in this experiment. We can therefore use the following equation to calculate characteristic slip times (τ) [4.22,4.23]:

$$\delta\left(\frac{1}{Q}\right) = 4\pi\tau(\delta f) \quad (4.3)$$

4.3 Results

The frequency shift and quality factor data for the xenon uptake on Cu(111), Ni(111), and graphene/Ni(111) are shown in figure 4.1. The frequency shift for a monolayer of xenon on an ideal, flat surface is approximately 37 Hz, corresponding to a coverage of 5.8 atoms/nm². Note that the frequency shift for a monolayer of xenon will vary slightly due to the changing xenon-xenon spacing for the different surfaces. The stepwise nature of the

isotherms indicate that our substrate films are clean and have atomically flat regions (30 nm)² or more in size. [4.24] Note that the frequency shift data for the Cu(111) sample under-represent the actual mass of the adsorbed film on account of film slippage effects (see equation 4.2).

The slip times for xenon on Cu(111), Ni(111), and graphene/Ni(111) are shown in figure 4.2. From highest to lowest xenon slip time, the surfaces are Cu(111), Ag(111), graphene, and Ni(111). The Xe/C₆₀ isotherm and Xe/C₆₀ slip time are shown separately in figures 4.3a and 4.3b. The monolayer slip times are shown in table 4.2.

4.4 Analysis and Discussion

In order to test the efficacy of equation 4.1, $\eta = \eta_{subs} + aU_o^2$, we plot in figure 4.4 the natural log of the xenon monolayer slip time τ in seconds versus the natural log of the adsorbate/substrate corrugation U_o in meV. Setting $\eta = m/\tau$ in equation 4.1 (m is adsorbate mass) and solving for τ , we find:

$$\tau = \frac{m}{\eta_{subs} + aU_o^2} \quad \ln(\tau) = \ln(m) - \ln(\eta_{subs} + aU_o^2) \quad (4.4)$$

Under the assumption that $\eta_{subs} < aU_o^2$ [4.25], equation 4.4 can be expanded as follows:

$$\ln(\tau) = \left[\ln(m) - \ln(a) - \frac{\eta_{subs}}{aU_o^2} + \frac{1}{2} \left(\frac{\eta_{subs}}{aU_o^2} \right)^2 - \dots \right] \quad (4.5)$$

Therefore when plotting $\ln(\tau)$ vs. $\ln(U_o)$, the above equation suggests the data should be well fit with a slope of -2 . The data for systems with similar lattice spacing (Xe/Cu(111), Xe/Ni(111), and Xe/graphene) is fit with a slope of -1.82 ± 0.20 .

If we assume that $\tau \sim 1/\eta \sim U_o^{-2}$, then we can fit our data to equation 4.4 and solve for the constants η_{subs} and a . At compressed monolayer coverage, we find $\eta_{subs} = 0.13 \pm 0.13 \text{ ns}^{-1}$ and $a = 0.012 \pm 0.0011 \text{ ns}^{-1} \text{ meV}^{-2}$. At coverage of 0.94 monolayers, we find $\eta_{subs} = 0.20 \pm 0.20 \text{ ns}^{-1}$ and $a = 0.010 \pm 0.0017 \text{ ns}^{-1} \text{ meV}^{-2}$. Liebsch et al. [4.6] found $a = 0.56 \text{ ns}^{-1} \text{ meV}^{-2}$ at a coverage of 0.94 monolayers. Some of the differences in our values can be explained by differing values of the surface corrugation. In our work, the total barrier height is used for U_o , but Liebsch et al. used $U_o/4.5$ in their work. Dividing $a = 0.56 \text{ ns}^{-1} \text{ meV}^{-2}$ by 4.5^2 gives $a = 0.028 \text{ ns}^{-1} \text{ meV}^{-2}$, much closer to our fitted value of $a = 0.010 \pm 0.0017 \text{ ns}^{-1} \text{ meV}^{-2}$. Note that the constant η_{subs} contains the electronic contribution to friction.

Assuming that all of the friction contained in the η_{subs} term is due to electronic friction, $1/\eta_{subs} = 1/\eta_e = \tau_e = 2.5 \text{ ns}$ or higher. For higher corrugation systems, such as Xe/Ni(111), the slip times are an order of magnitude lower than 2.5 ns, indicating that phononic friction must dominate.

The monolayer slip times of Xe/Ag(111) and Xe/C₆₀ are also plotted in figure 4.4 using estimated values of the corrugation. It is possible that the dissimilar conditions in lattice spacing for the Xe/Ag(111) and Xe/C₆₀ experiments cause the deviation from the fitted slope of -2 .

It should be noted that Xe/Cu(111) at 77 K is a commensurate system [4.12], and that Xe/Ni(111) and Xe/graphene are not commensurate systems [4.13]. Many other experiments [4.26] show that commensurate systems have very high sliding friction, or even

that the films “lock down” onto the substrate. In our results, however, the commensurate Xe/Cu(111) system has the highest slip time, or lowest friction. It has been observed numerically [4.3] that systems with low surface corrugation will slip, even in commensurate systems. The Xe/Cu(111) system has the lowest surface corrugation of the systems studied; this may explain the high slippage of the xenon film. Note that in the Xe/C₆₀ system, which should have high surface corrugation, the xenon film does lock down (no slipping) at low coverage. This may indicate a commensurate phase at low coverage, where the xenon atoms lie in the valleys of the C₆₀ surface potential.

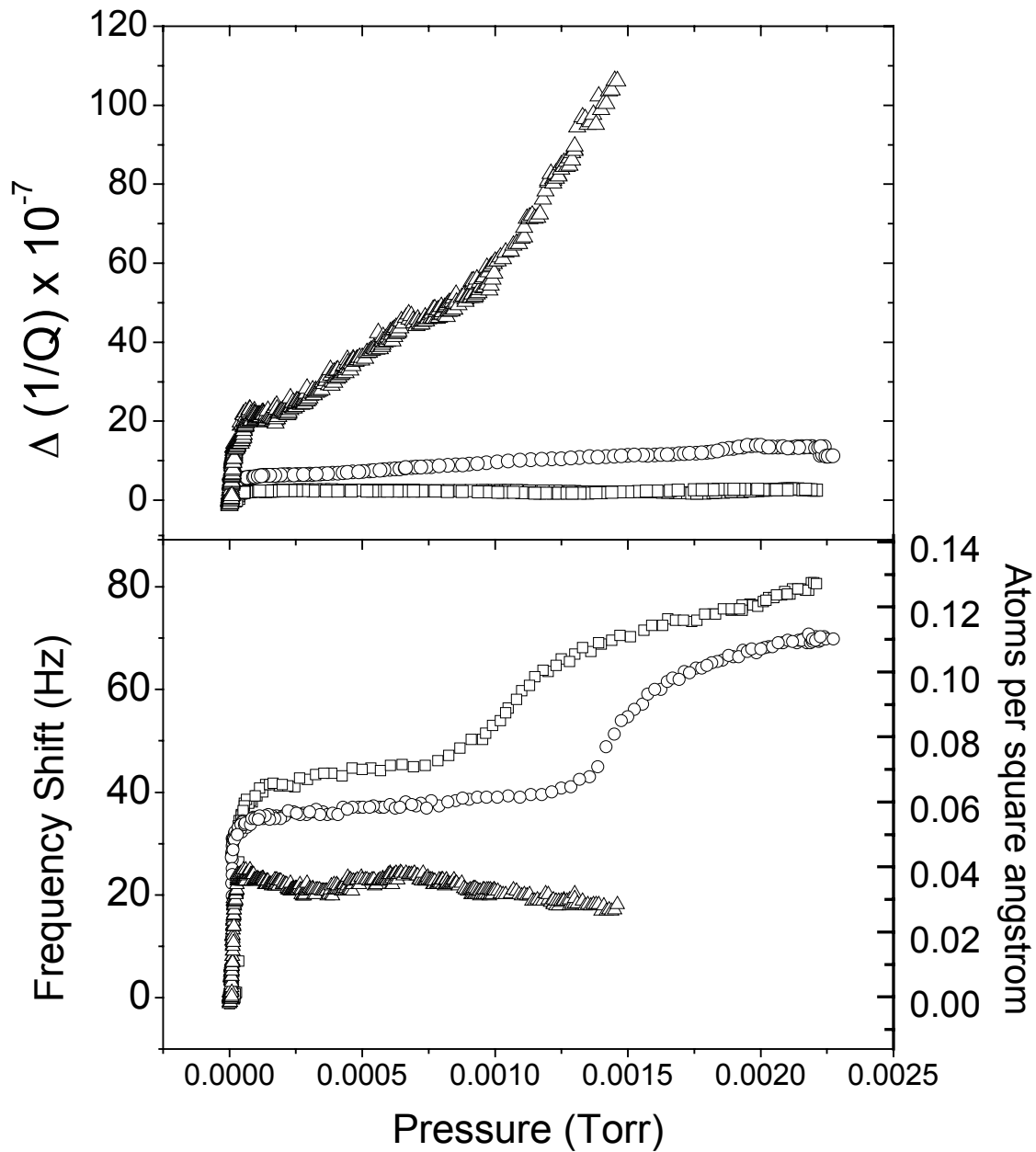


Figure 4.1. Xenon mass uptake and quality factor shift for Cu(111) (triangles), Ni(111) (squares), and graphene/Ni(111) (circles). Note that the frequency shift for Xe/Cu(111) is reduced; the high slippage of the Xe/Cu(111) causes the xenon to decouple from the oscillation of the Cu(111) substrate. [4.23] The quality factor has been multiplied by a factor of 10^{-7} .

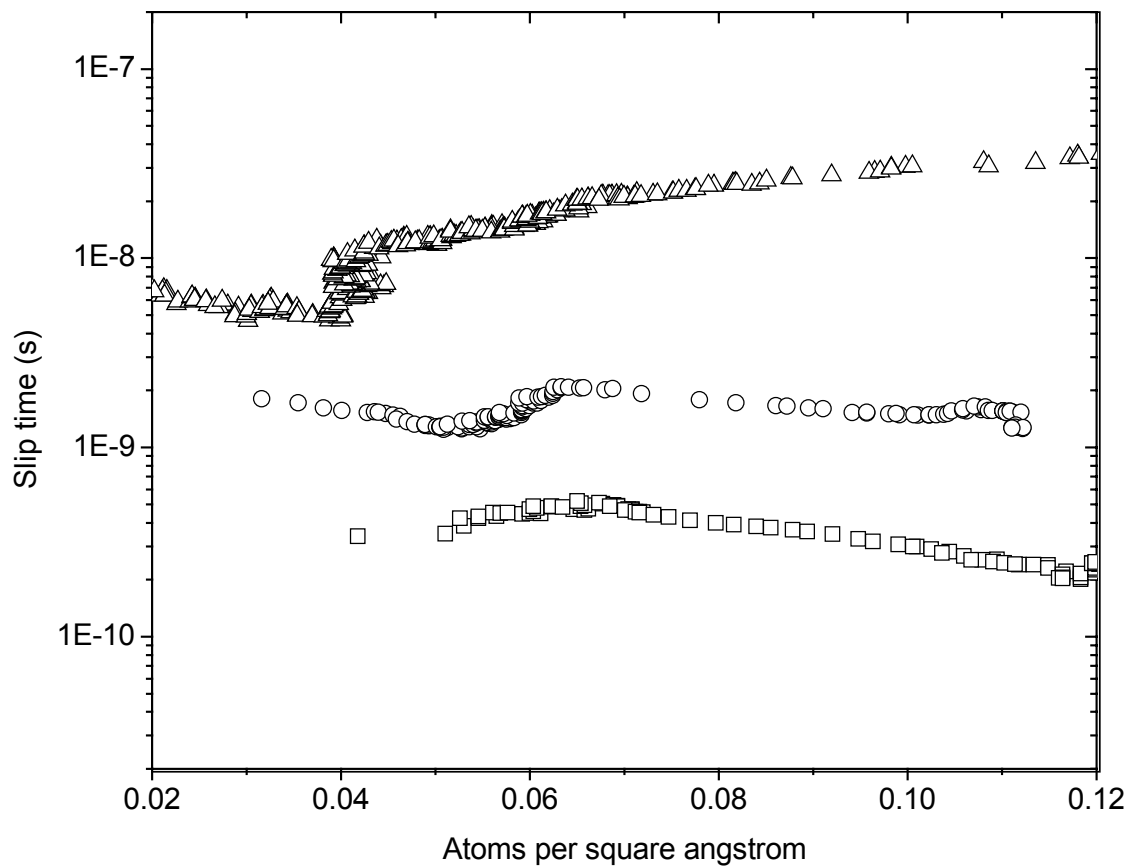


Figure 4.2. The slip times for xenon on Cu(111) (triangles), Ni(111) (squares), and graphene/Ni(111) (circles).

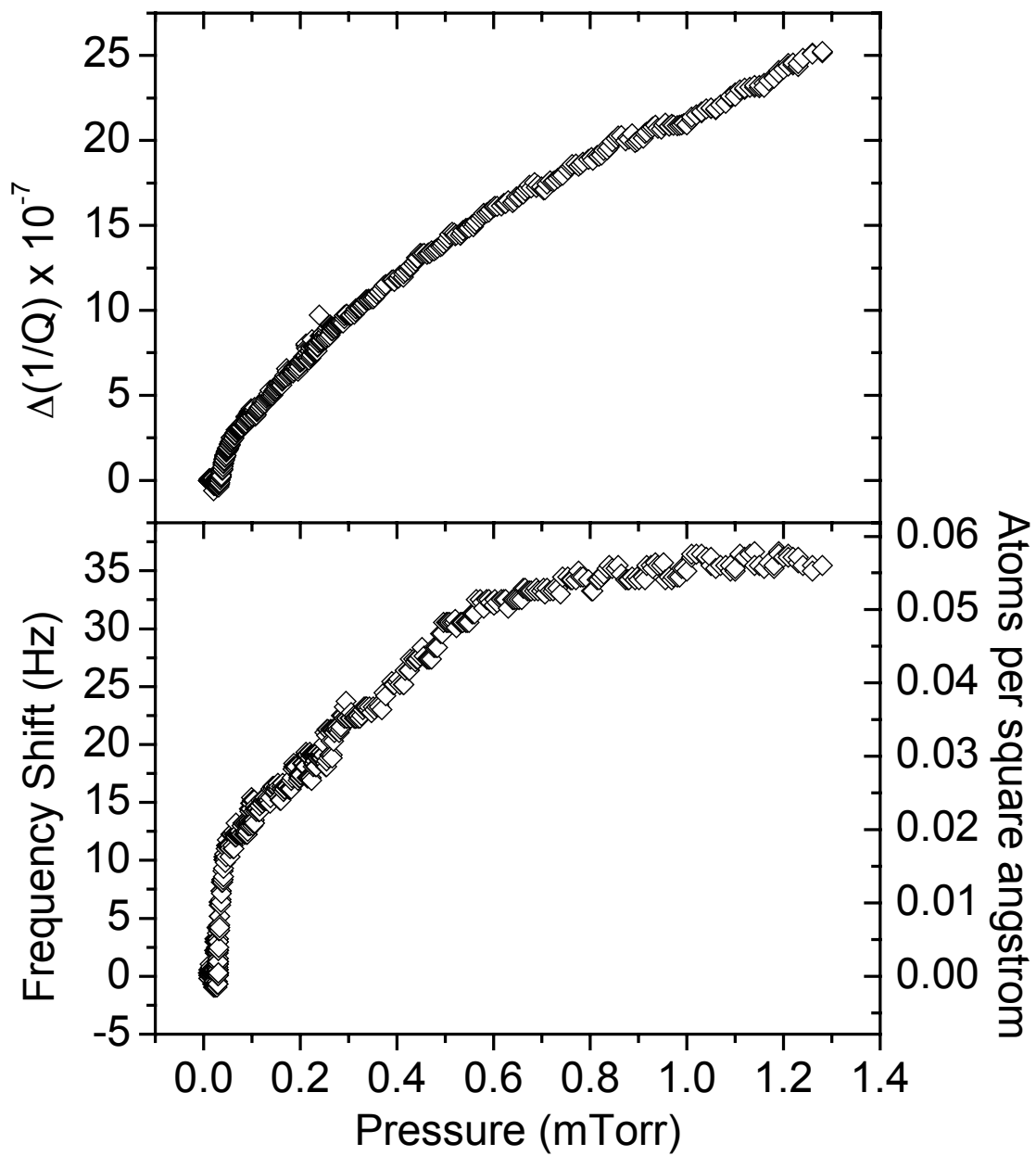


Figure 4.3a. Xenon mass uptake and quality factor shift for $C_{60}/Ag(111)$.

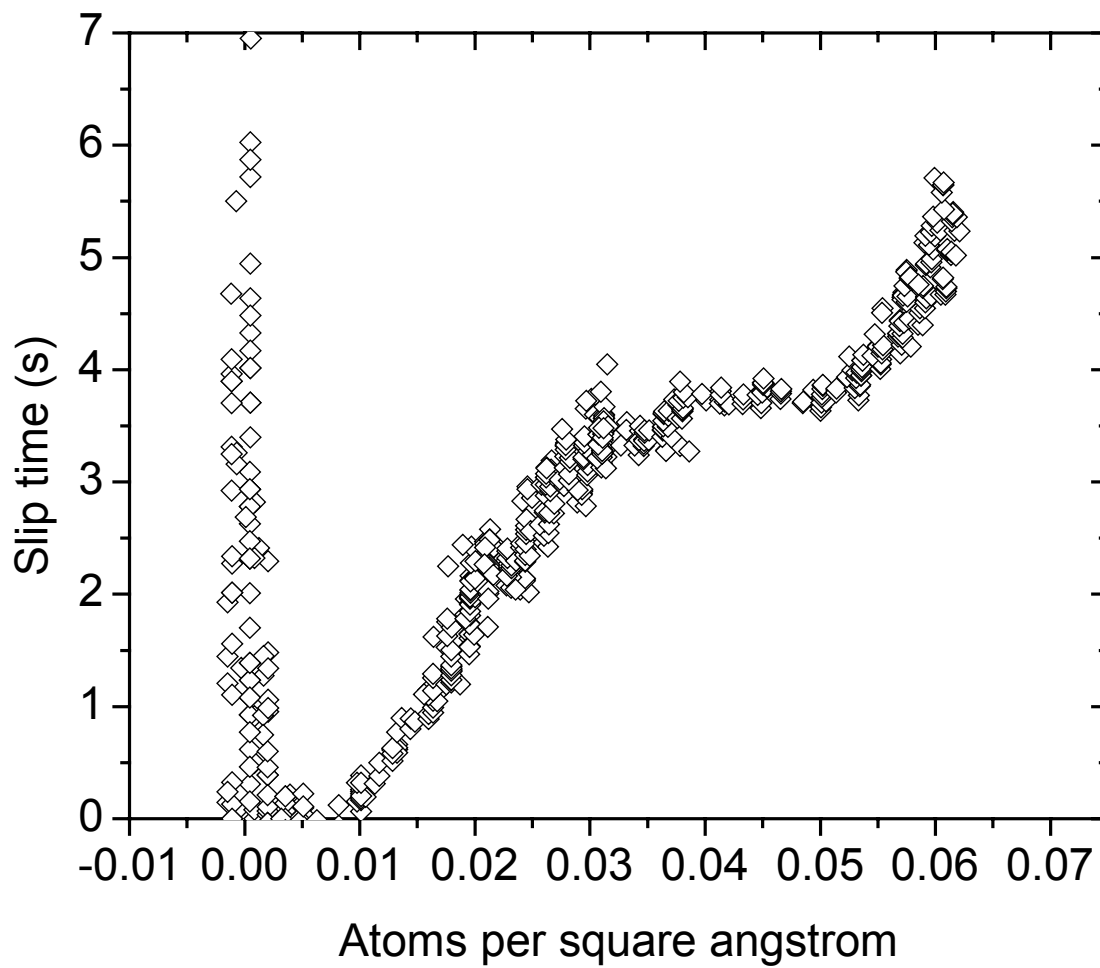


Figure 4.3b. (Bottom) Slip time for xenon sliding on $C_{60}/Ag(111)$. Note that the slip time is zero for coverages less than $0.01 \text{ atoms}/\text{angstrom}^2$.

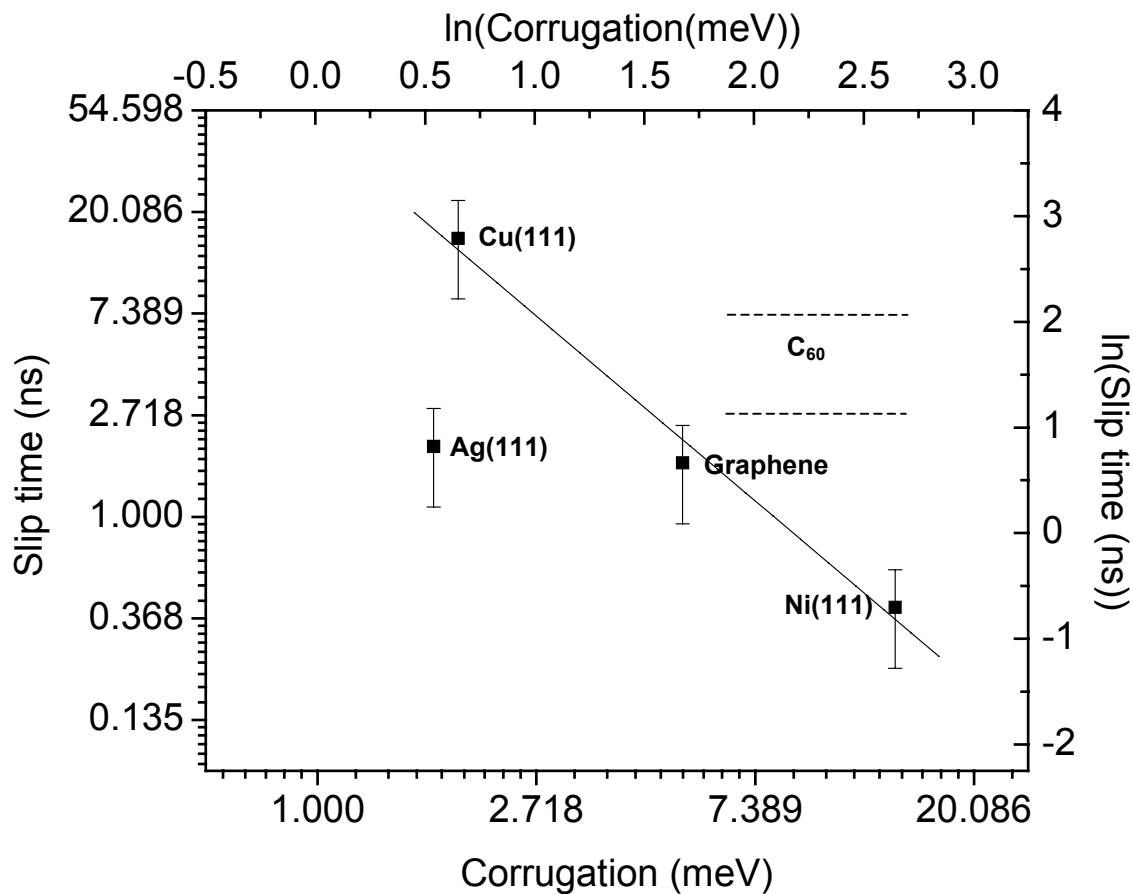


Figure 4.4. Natural log of the slip time vs. natural log of the surface corrugation. The line is the fit to the Xe/Cu(111), Xe/Ni(111), and Xe/graphene/Ni(111) data. It has a slope of -1.82 ± 0.20 and an intercept of 3.8 ± 0.37 . The corrugation value for Xe/Ag(111) is estimated here as 1.7 meV. The C₆₀ data point has a slip time of 5.5 ns, and the dashed lines around the C₆₀ represents the uncertainty in slip time. The corrugation of Xe/C₆₀ is unknown.

Table 4.1. The surface corrugations, substrate spacing, and overlayer spacing for Ag(111), Cu(111), Ni(111), and graphene/Ni(111). The corrugation of Xe/Cu(111) was acquired by measuring the energy of the $q=0$ longitudinally polarized phonon mode. [4.9] The corrugation for Xe/Ni(111) was acquired using diffusion rate measurements [4.11]. Note that corrugation estimates from diffusion rates could be an overestimate, as diffusion rate measurements often include the energy of detachment from adsorbate islands on the surface [4.15]. The corrugation of 5.3 meV for Xe/graphene was estimated from the corrugation of Xe/graphite, which were acquired via transmission high-energy electron diffraction measurements and model calculations. [4.10]

System	Surface Corrugation (meV)	Substrate Spacing (nm)	Xenon Spacing (nm)
Ag(111)	0.69 – 2.7 ^[4.14]	0.288	0.439 – 0.452 ^[4.2]
Cu(111)	1.9 ^[4.9]	0.255	0.4414 ^[4.12]
Ni(111)	14 ^[4.11]	0.249	0.441 ^[4.13]
Graphene/Ni(111)	5.3 ^[4.10]	0.249	0.441

Table 4.2 Monolayer slip times and surface corrugation for Cu(111), Ag(111), Ni(111), Graphene/Ni(111), and C₆₀/Ag(111). The slip time uncertainties are 45%.

Substrate	Slip time (ns)	Surface Corrugation (meV)
Cu(111)	15.5	1.9 ^[4.9]
Ag(111)	2.0	0.69—2.7 ^[4.14]
Ni(111)	0.41	14 ^[4.11]
Graphene/Ni(111)	1.7	5.3 ^[4.10]
C ₆₀ /Ag(111)	5.5	Large??

CHAPTER 5: QUARTZ CRYSTAL MICROBALANCE STUDIES OF THE SLIPPAGE OF SOLID AND LIQUID KRYPTON MONOLAYERS ON METAL(111) AND C₆₀ SURFACES

**manuscript in preparation for submission*

T. Coffey, S.M. Winder and J. Krim

Physics Department

North Carolina State University

Raleigh, NC 27695-8202

Abstract

We report a Quartz Crystal Microbalance (QCM) study of the nanotribology of solid and liquid krypton monolayers adsorbed on Cu(111), Ag(111), Ni(111), and C₆₀ substrates at 77.4 K. We document the liquid-solid phase transition and compare the slip times of the krypton for the various substrates. The slip times for the solid krypton monolayers are longer than the slip times for liquid krypton monolayers on metal substrates and monolayer C₆₀ films, as observed previously for krypton/Au(111). However, for bilayer C₆₀ films, the jump in slip time at the liquid-solid phase transition is not present. We discuss these topics and the underlying reasons herein.

5.1 Introduction

As technology tends towards the nanometer scale, the importance of understanding the fundamental origins of friction has increased. The quest to understand friction has led to experiments conducted in extremely simple and well-characterized systems at the nanoscale, such as studies of monolayer films sliding on substrates. These systems exhibit viscous friction, $F = (m/\tau)v$; $F/A = S = \eta v$. (Here, m , τ , and v are the mass, slip time, and velocity of the adsorbates, and A , S , and η are the area, shear stress, and friction coefficient for the systems.) Viscous friction is believed to arise from two sources, phononic η_p , and electronic, η_e , where $\eta = \eta_p + \eta_e$. At the atomic scale, phononic friction, or the energy dissipation caused by the excitation of atomic lattice vibrations (phonons), is believed to dominate. Electronic friction, or energy dissipation caused by the excitation of electron-hole pairs, has also been suggested as a possible source of friction if one of the materials is a conductor. To date, most of the modeling efforts have focused on phononic friction.

The Quartz Crystal Microbalance (QCM) technique is an extremely sensitive probe of viscous friction, capable of detecting sub-monolayer films and measuring sub-nanosecond slip times, τ , of adsorbate films on surfaces [5.1, 5.2]. In 1991, Krim, Solina, and Chiarello utilized QCM measurements of the friction of krypton monolayers sliding on Au(111) at 77.4 K. [5.3] Krypton is a liquid at 77.4 K at low film coverage. As the monolayer coverage increases, krypton undergoes a two dimensional liquid-solid phase transition. [5.4, 5.5] This phase change can be seen in the QCM frequency, dissipation, and slip time data. Krim and colleagues saw the phase change in the QCM slip time data, observing a distinct increase in

the slip time for solid vs. liquid monolayers of Kr/Au(111). In other words, the surface was “slippery when dry.”

In 1994, Cieplak, Smith, and Robbins [5.6] employed standard molecular dynamics algorithms to model mobile krypton atoms on a perfectly rigid gold substrate. In their simulations, the frictional force comes from the vibrations (phonons) of the krypton adsorbates as they slide atop the rigid gold substrate. Scaling the surface corrugation to fit the data, they reproduced the 1991 experimental results of Krim et al. Their simulations included only one source of friction: phononic friction. Given the close match between their simulations and the QCM experiments, they concluded that phononic friction was “the major source of friction” for the krypton on Au(111) system. In a later publication, Muser and Robbins [5.7] hypothesized that any electronic contribution to friction for this system should be relatively constant with coverage, and would only serve to decrease the height of the jump in slippage due to the phase transition. (See figure 5.1.)

Inspired by the fact that the jump in slip time may be an indication of the phononic friction levels, we report here a series of QCM experiments for Kr sliding on Ag(111), Cu(111), Ni(111), and C₆₀ substrates at 77.4 K. Specifically, we examine the change in slippage before and after the liquid-solid phase transition. It is our hope that these experiments will be modeled and will further knowledge about the origins of friction for these systems.

5.2 Experimental

The microbalance crystals for these studies were overtone-polished 8 MHz AT-cut quartz that had quality factors near 10^5 . For the Cu(111) sample, the copper was deposited atop a QCM with a 20 nm titanium pre-coat, to prevent roughening of the copper electrode. [5.8] The base pressure of the vacuum system ranged from 8×10^{-11} to 5×10^{-10} Torr. Thermal evaporation was then used to deposit 60 nm of 99.999% pure Cu or 80 nm of 99.999% pure Ag atop the titanium pre-coat or blank QCM, respectively, producing a mosaic structure with a (111) fiber texture [5.9]. C₆₀ substrates were prepared by thermally evaporating C₆₀ monolayers atop an 80 nm thick Ag(111) electrode on a blank QCM. The QCM frequency shift was monitored during the C₆₀ deposition; one monolayer of C₆₀ corresponds to a frequency shift of 21 +/- 1 Hz, or a mass uptake of 73 +/- 4 ng/cm². The C₆₀ was deposited immediately after the Ag(111) deposition.

The 80 nm Ni(111) films were deposited using an electron beam evaporator in UHV onto a blank QCM. The deposition rate was several angstroms per second. All samples were immediately transferred *in situ* to the adsorption cell where they were electrically connected to an external Pierce oscillator circuit. They were then chilled to 77.4 K by submersion in a liquid nitrogen bath.

After the samples had come to thermal equilibrium, they were exposed to research grade krypton gas, [5.10] and frequency and amplitude shifts were monitored as a function of increasing pressure. The frequency shifts (δf) are proportional to the mass per unit area of the film that tracks the QCM motion. [5.11]. Film slippage results in some fraction of the

mass of the film decoupling from the oscillation of the substrate, and a concomitant reduction in the frequency shift [5.12].

$$\frac{\delta f_{massloading}}{f} = -\frac{2\rho_f t_f}{\rho_q t_q} \quad \delta f_{film} = \frac{\delta f_{massloading}}{1 + (\omega\tau)^2} \quad (5.1)$$

Here, ρ_f and t_f are the density and thickness of the adsorbed film, and ρ_q (2.65 g/cm³) and t_q (0.021 cm for $f=8$ MHz) are the density and thickness of the QCM. The change in amplitude (A) is proportional to the change in quality factor (Q): $\delta(Q^{-1}) = c\delta(A^{-1})$. To determine the proportionality constant, c , the samples are calibrated with helium gas adsorption after completion of the krypton uptake measurements. [5.1] Frequency and quality factor shifts can also be caused by gas pressure, tensile stress, and temperature, however these effects were negligible in this experiment. The following equation can therefore be used to calculate characteristic slip times (τ) [5.1, 5.2]:

$$\delta\left(\frac{1}{Q}\right) = 4\pi\tau(\delta f) \quad (5.2)$$

5.3 Results

The frequency shift and quality factor data for the krypton uptake on Cu(111), Ag(111), Ni(111), and C₆₀ are shown in figures 5.2-5.6. At 77.4 K, krypton first forms a liquid monolayer with a coverage of 0.066 atoms/angstroms² (~26.6 Hz for $f_o = 8$ MHz crystals). As the coverage increases, the krypton monolayer becomes more tightly packed and changes phase to a solid, with a monolayer coverage of 0.078 atoms/angstroms² (~31.4 Hz). [5.4, 5.5] Note that the frequency shift for a monolayer of krypton will vary slightly due

to the changing krypton-krypton spacing for the different surfaces and varying surface roughness. The stepwise nature of the isotherms indicate that our substrate films are clean and have atomically flat regions $(30 \text{ nm})^2$ or more in size. [5.4, 5.13] Note that the frequency shift data for the Cu(111) sample under-represent the actual mass of the adsorbed film on account of film slippage effects (see equation 5.1).

The slip times for krypton on Cu(111), Ag(111), Ni(111), and C₆₀ are shown in figures 5.7-5.10. At a coverage of one monolayer (0.078 atoms/angstrom² coverage) there are ‘jumps’ in the slip time for Cu(111), Ag(111), Ni(111), and the C₆₀ monolayer surfaces, attributable to the liquid-solid phase transition. For the C₆₀ bilayer surface, there is no jump in slip time at monolayer coverage. The slip times for the liquid and solid phases of krypton at given monolayer coverage are shown in table 5.1.

5.4 Discussion

For the metal(111) surfaces, a jump in the slip time, attributable to the liquid-solid phase transition, is observed. However, this jump is not as large as that previously observed for krypton/Au(111) surfaces ($\tau_{sol}/\tau_{liq} = 5.0$, see table 5.1) [5.3]. One possibility is that the electronic friction of a system is linked to the chemical reactivity of the adsorbate-substrate system. This may explain the large jump in slip time for Kr/Au(111) as compared to the surfaces studied here; the electronic friction for the surfaces studied here may be higher. As suggested by Robbins and Muser [5.7], this may reduce the height of the jump in slip time due to the liquid-solid phase transition.

The slip time for liquid and solid krypton monolayers is slightly longer atop C_{60} bilayer films than C_{60} monolayer films. One possible explanation may be a changing coefficient of electronic friction for a monolayer vs. a bilayer C_{60} film. Electronic friction is present only for conductors; for insulators, only phononic friction is present. C_{60} is more insulating than silver; so as the thickness of the C_{60} coating increases, the substrate becomes less conducting, hence less electronic friction and a longer slip time.

Is it possible, however, that the electronic friction changes slightly for liquid vs. solid phases of krypton? Electronic friction has been related to the surface resistivity [5.14]. It is well-known that the resistivity of a system is dependent on lattice defects. Resistivity, and hence electronic friction, occurs when conduction electrons scatter off of the lattice. The more imperfections and defects present, the higher the resistivity. A liquid phase has more imperfections in a lattice than a solid phase; it therefore follows that a two dimensional liquid phase might have a higher resistivity, and hence higher electronic friction and lower slip times, than a two dimensional solid phase.

One of the most interesting results of this study is that the ‘jump’ in slip time due to the two dimensional liquid-solid phase transition in krypton is present for monolayer $C_{60}/Ag(111)$ films but disappears for bilayer films of $C_{60}/Ag(111)$. If the electronic friction is higher for the liquid phase of krypton and the reduced slip time for C_{60} monolayers vs. bilayers is due to electronic friction, then the slip times for liquid krypton on monolayers of C_{60} would be lower than the slip times for liquid krypton on C_{60} bilayers. If the electronic friction is much reduced for a solid phase of krypton, then the slip times for solid krypton for C_{60} monolayers vs. bilayers would depend mostly on phononic contributions to friction, and might be very similar.

Krypton sliding atop Au(111) was modeled as a thin, elastic krypton sheet atop a rigid, periodic Au(111) potential [5.6]. In the liquid phase, the krypton atoms were more mobile and could deform to fill in the low potential sites in the Au(111) substrate. This caused high phononic friction and short slip times. In the solid phase, however, the krypton atoms were more rigidly bound to each other, and thus could not as easily deform to fill the low potential sites. Thus, the solid phase had lower phononic friction and longer slip times than the liquid phase. C_{60} has a much larger lattice spacing than Au(111). It might therefore be more difficult for the liquid krypton monolayer to deform and fill the low potential sites. Therefore the phononic contribution for liquid vs. solid krypton monolayers may be similar, leaving only differences in electronic friction to explain the jump in slippage for monolayer C_{60} .

5.5 Conclusions

We have shown that for metal(111) substrates, there is a jump in the slip time at solid monolayer krypton coverage, attributable to the liquid-solid phase transition. This jump is also present for krypton slipping atop monolayers, but not bilayers, of C_{60} . Although the damping and atomic scale corrugation is not known for all of these systems, they are ideal for further study and future modeling.

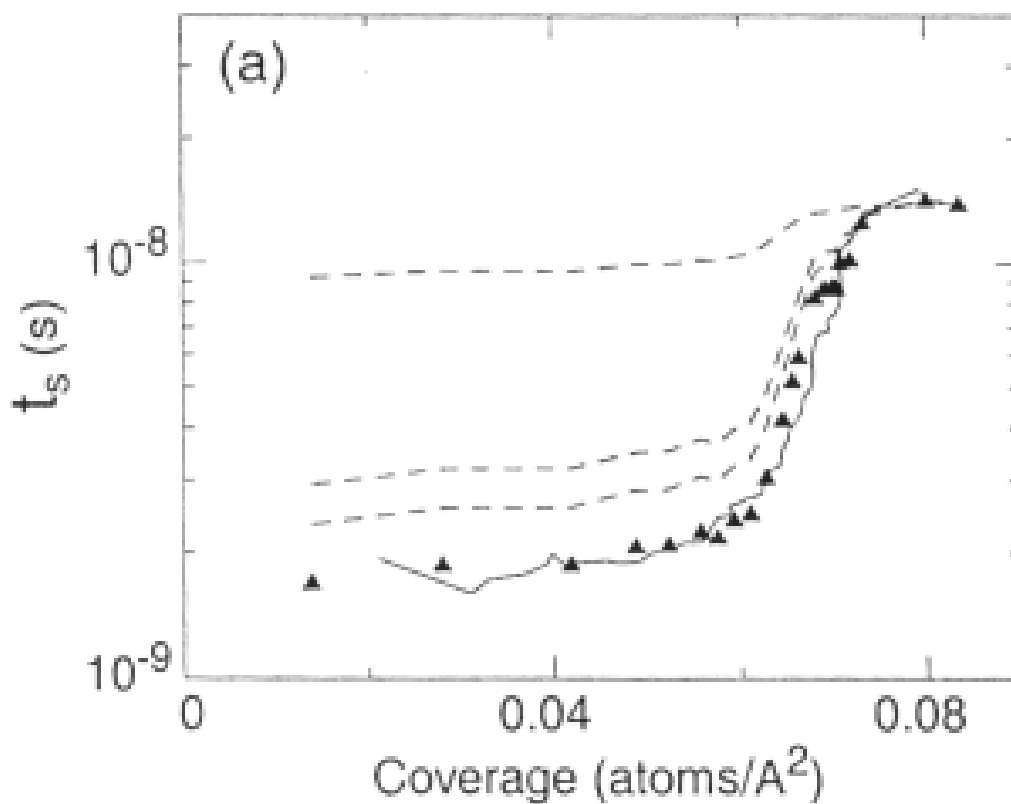


Figure 5.1. The triangles represent slip time data acquired by Krim et al. for Kr/Au(111). [5.3] The solid line shows the numerical model of Cieplak et al., which fit the experimental data using only phononic friction. [5.6] The dashed lines represent their numerical model with electronic friction included, and equal to 1/3, 1/2, and 9/10 of the friction at high coverage due to electronic friction, from bottom to top. Note that electronic friction serves to decrease the jump in slip time attributable to the phase transition. [5.7]

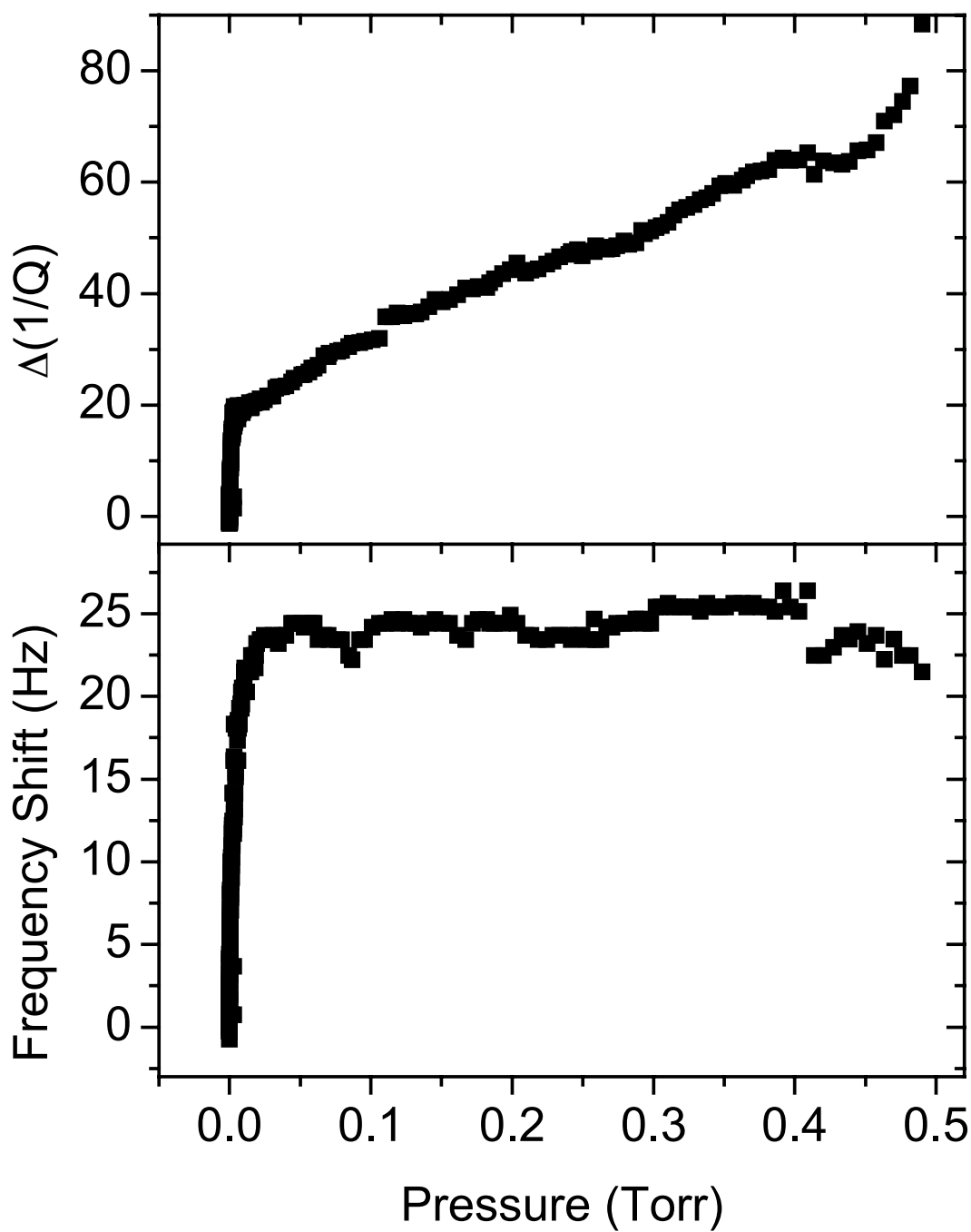


Figure 5.2. Frequency and inverse quality shifts for Kr/Cu(111). Raw data file: 101003a.dat. Note the frequency shift is reduced due to the large slippage of the krypton film. $\Delta(1/Q)$ in the figure is multiplied by 10^{-7} . The helium calibration constant is 0.341, calibrated from file 101003b.dat.

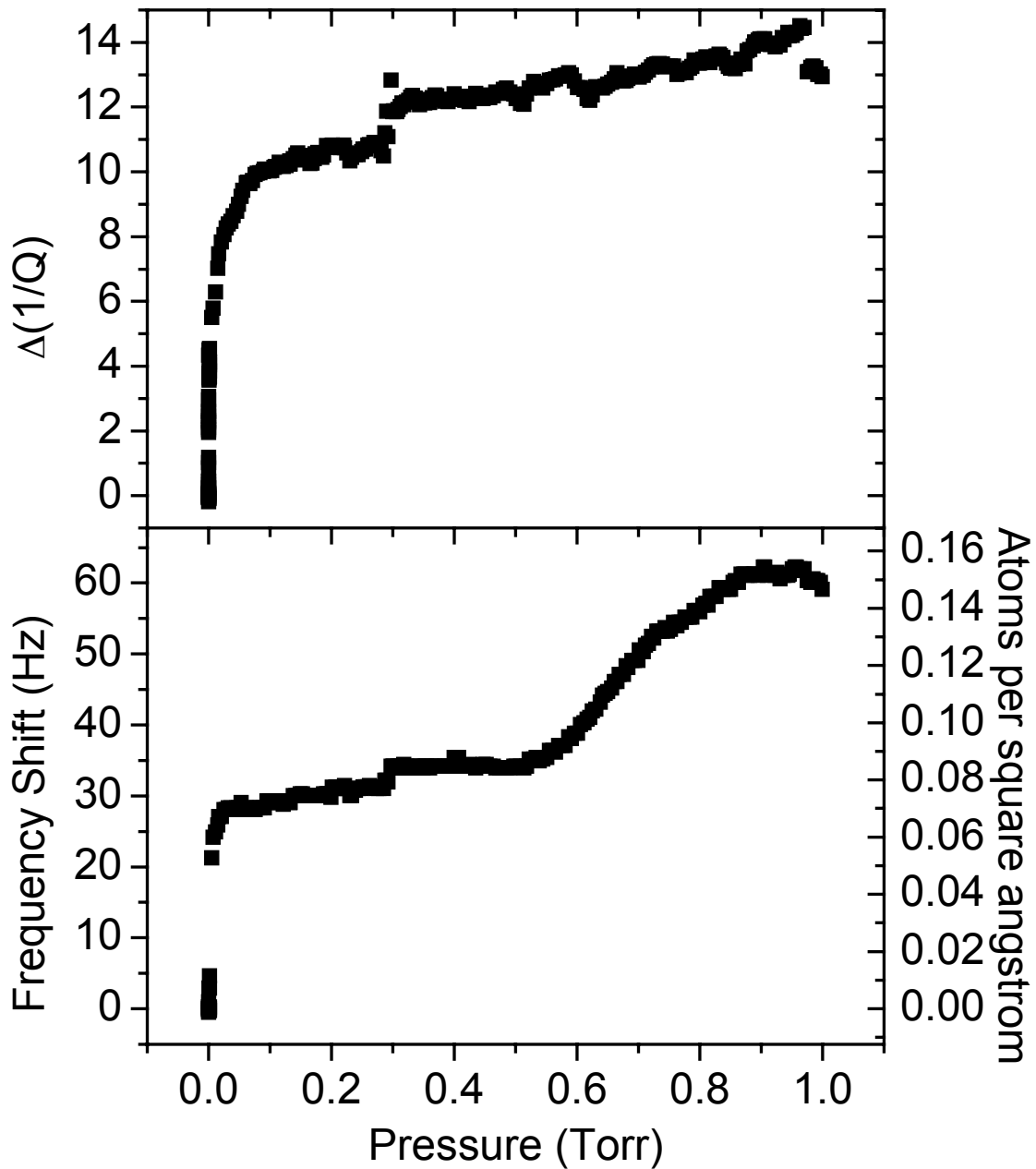


Figure 5.3. Frequency and inverse quality shifts for Kr/Ag(111). Raw data file: 012404a.dat. $\Delta(1/Q)$ in the figure is multiplied by 10^{-7} . The helium calibration constant is 0.85 for $1/A = 13-13.8 \text{ V}^{-1}$ and 0.326 for $1/A = 13.8-16 \text{ V}^{-1}$, calibrated from file 012404c.dat.

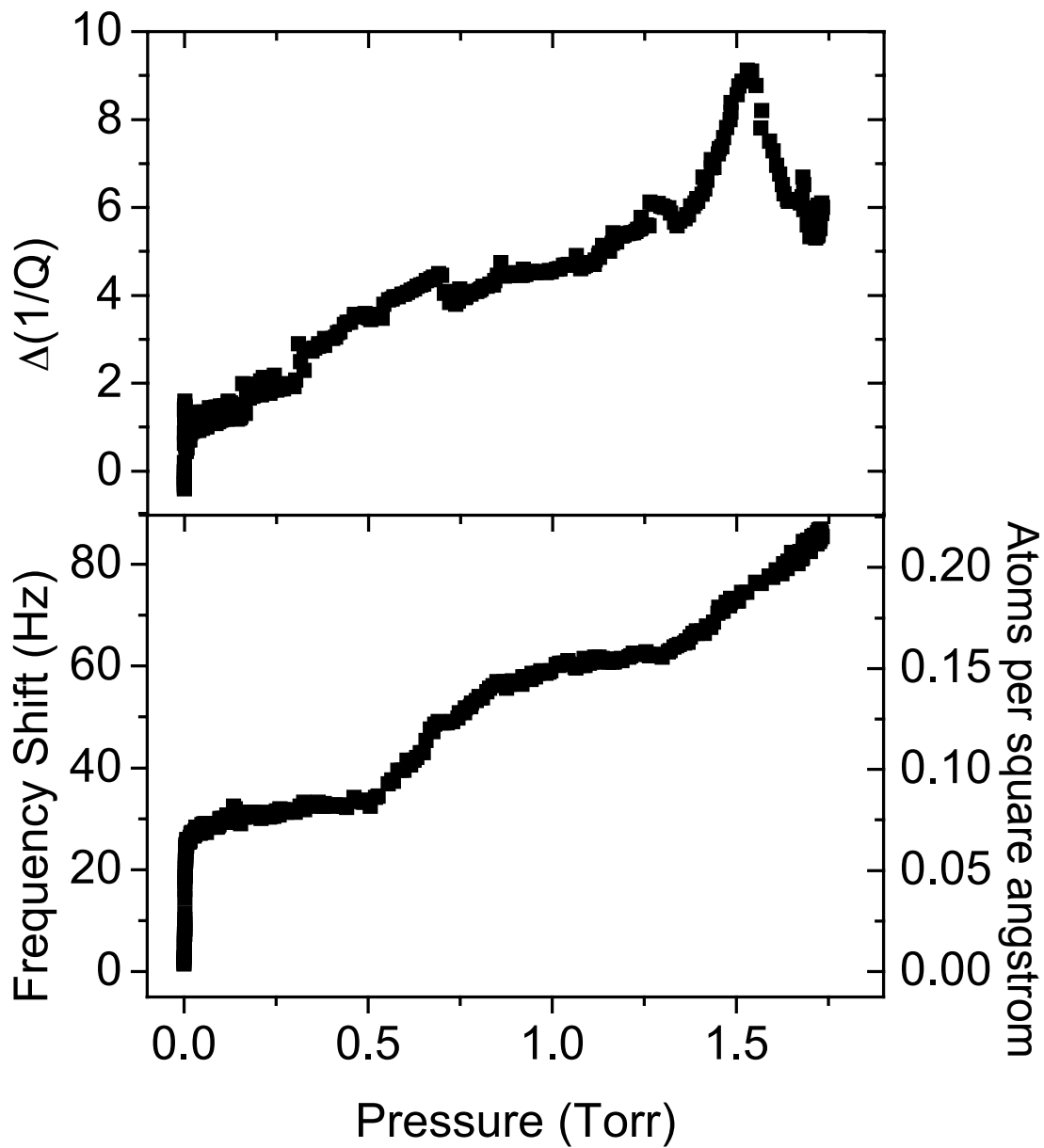


Figure 5.4. Frequency and inverse quality shifts for Kr/Ni(111). Raw data file: 022602d.dat. $\Delta(1/Q)$ in the figure is multiplied by 10^{-7} . The helium calibration constant is 0.511 for $1/A = 15.5-16.3 \text{ V}^{-1}$ and 0.29 for $1/A = 16.3-17.9 \text{ V}^{-1}$, calibrated from file 022602e.dat.

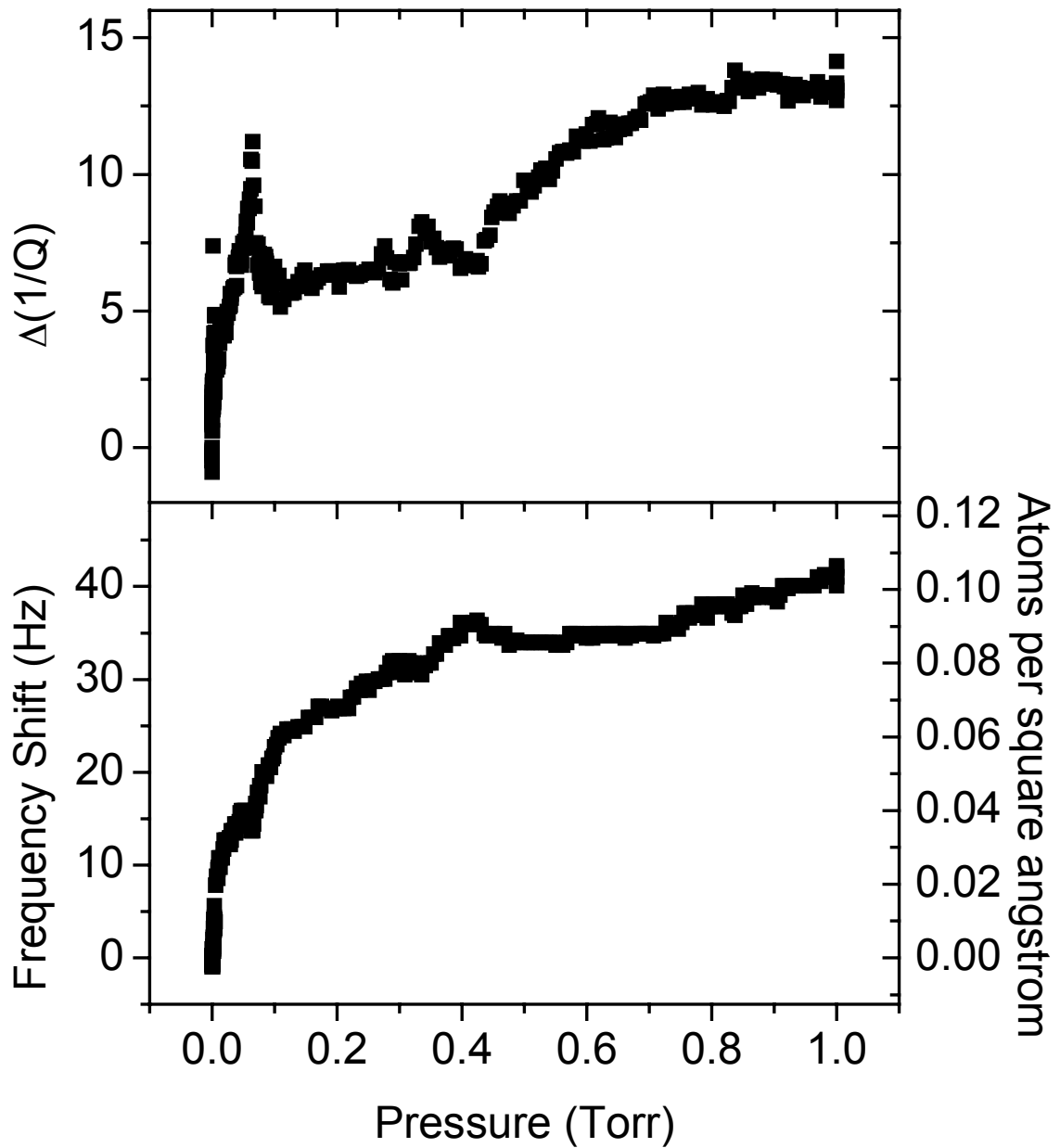


Figure 5.5. Frequency and inverse quality shifts for Kr/monolayer C_{60} . Raw data file: 061803a.dat. $\Delta(1/Q)$ in the figure is multiplied by 10^{-7} . The helium calibration constant is 0.43, calibrated from file 061703e.dat.

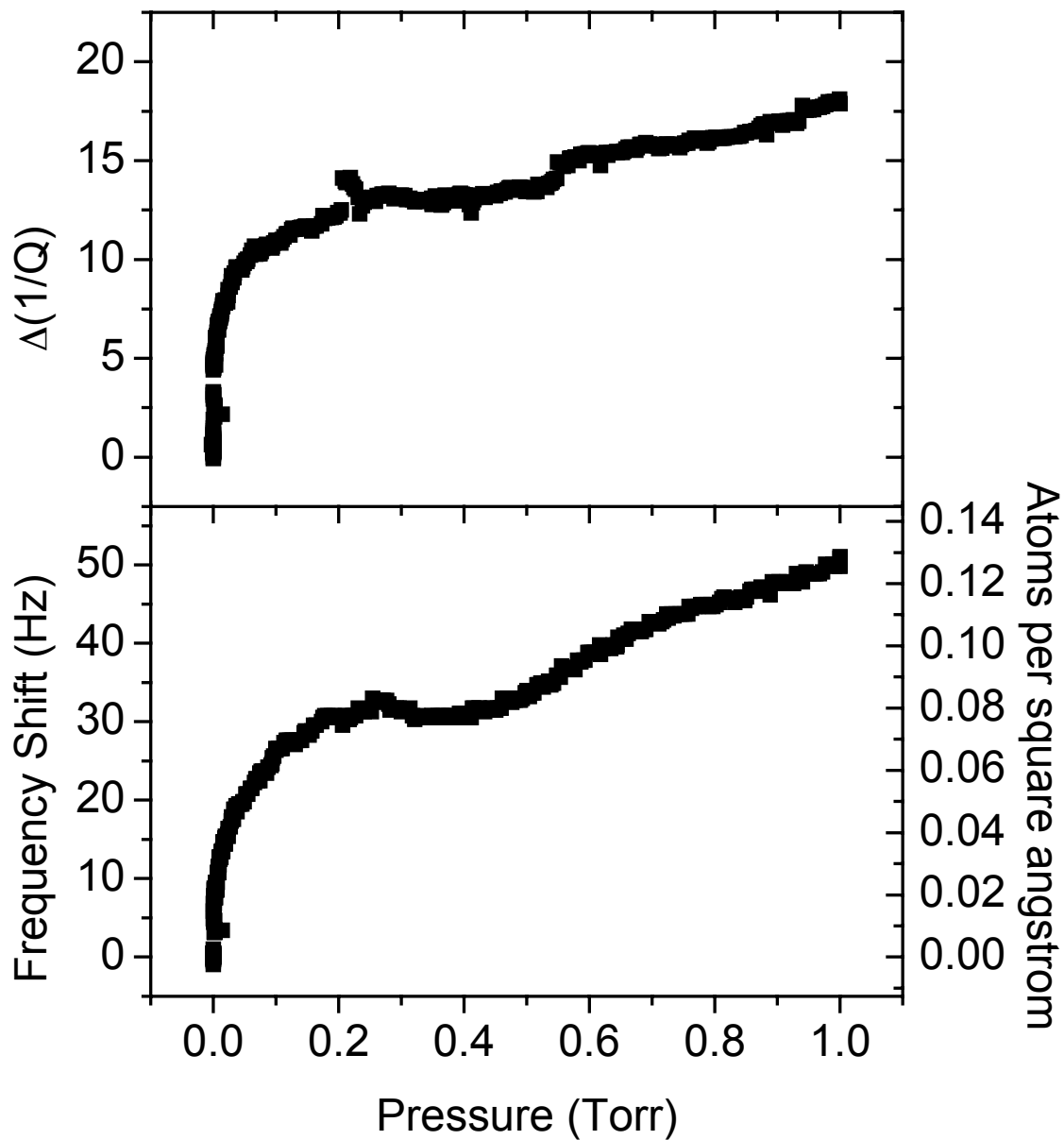


Figure 5.6. Frequency and inverse quality shifts for Kr/bilayer C_{60} . Raw data file: 062403b.dat. $\Delta(1/Q)$ in the figure is multiplied by 10^{-7} . The helium calibration constant is 0.312, calibrated from file 062404c.dat.

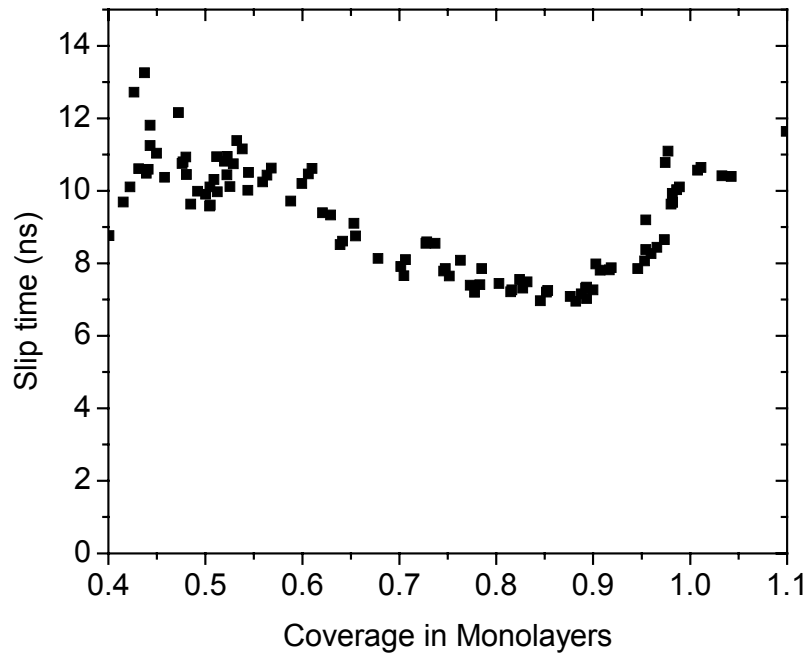


Figure 5.7. QCM slip time data for Kr/Cu(111).

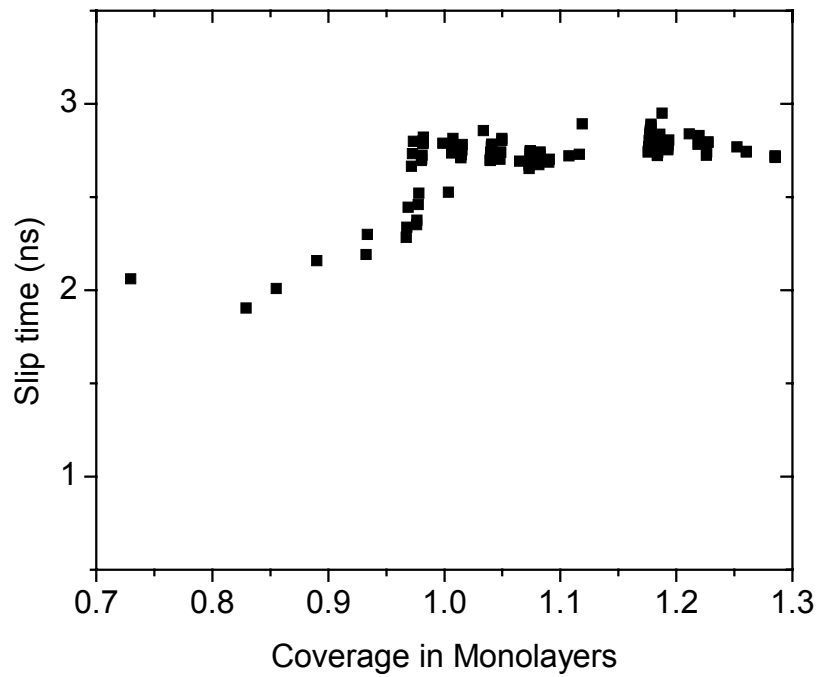


Figure 5.8. QCM slip time data for Kr/Ag(111).

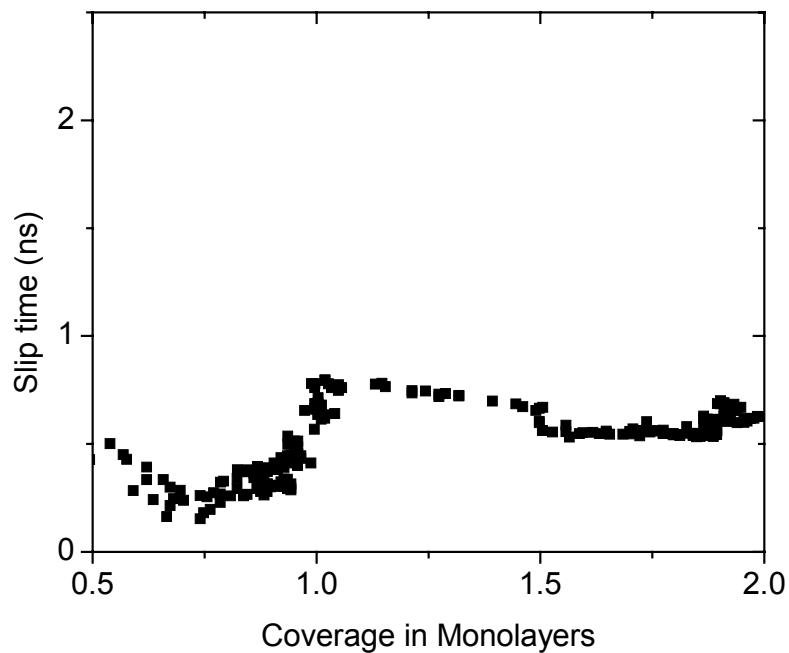


Figure 5.9. QCM slip time data for Kr/Ni(111).

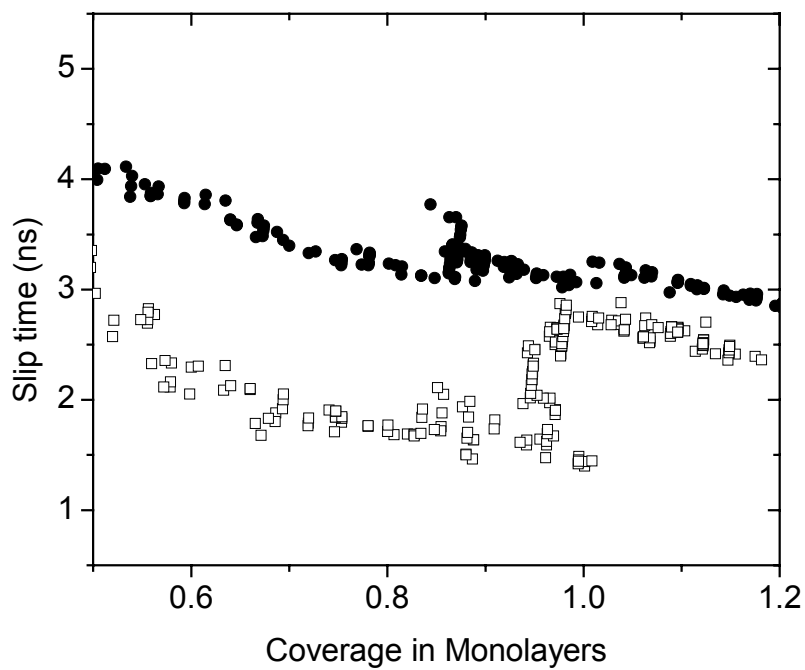


Figure 5.10. QCM slip time data for Kr/monolayer C_{60} (open squares) and bilayer C_{60} (filled circles). (June 2003 sample)

Table 5.1. Slip times for the liquid (τ_{liq}), solid (τ_{sol}) phases of krypton at given monolayer coverage (Θ) and the ratio of the slip time of liquid and solid phases for the various substrates. The superscripts for the C_{60} substrates indicate the number of C_{60} monolayers. The Au(111) data has been previously published in 2 independent experiments; however both experiments gave the same ratio of solid to liquid slip times [5.3].

Substrate	τ_{liq} in ns (Θ in monolayers)	τ_{sol} in ns (Θ in monolayers)	$\tau_{\text{sol}}/\tau_{\text{liq}}$
Cu(111)	7.0 (0.89)	11 (1.0)	1.6
Ag(111)	2.1 (0.9)	2.7 (1.0)	1.3
Au(111) [5.3]	2.0; 1.0 (0.85)	10.0; 5.0 (1.0)	5.0
Ni(111)	0.26 (0.8)	0.78 (1.0)	3.0
$C_{60}^{(1)}/\text{Ag}(111)$	1.6 (0.93)	2.7 (1.0)	1.7
$C_{60}^{(2)}/\text{Ag}(111)$	3.1 (0.93)	3.3 (1.0)	1.1

CHAPTER 6: THE EFFECTS OF CHANGING ADSORBATE DAMPING ON THE VISCOUS COEFFICIENT OF FRICTION

**manuscript in preparation for submission*

T. Coffey and J. Krim

Physics Department

North Carolina State University

Raleigh, NC 27695-8202

Abstract

It has been hypothesized that the damping of Frustrated Translational (FT) phonon modes is linearly proportional to friction between adsorbates and substrates. [6.1] The parallel FT modes are believed to be directly linked to sliding friction, but the nature of the relation between sliding friction and perpendicular FT modes is unclear. The perpendicular FT mode of n-octane adsorbed on Cu(111) has a damping constant of 0.45 meV, twice as large as that of n-octane adsorbed on Pb(111), 0.26 meV. [6.2] We report here QCM observations of the sliding of n-octane on copper and lead surfaces to determine how the damping of perpendicular FT modes affect sliding friction. We have observed that the slip time for a monolayer of n-octane/Cu(111) is 0.94 ns +/- 0.36 ns, and the slip time of n-octane/Pb(111) is 0.59 ns +/- 0.13 ns. We therefore observe no direct evidence of a link between the damping of perpendicular FT modes and sliding friction.

6.1 Introduction

The study of monolayer adsorbate films sliding on surfaces has been used extensively to probe the fundamental origins of friction [6.3]. These films exhibit viscous friction $F = (m/\tau)v$; $F/A = S = \eta v$. (Here, m , τ , and v are the mass, slip time, and velocity of the adsorbates, and A , S , and η are the area, shear stress, and friction coefficient for the systems.) The viscous coefficient of friction, η , is due to the transfer of the sliding energy of the adsorbate films into phonons (η_p), or for metal substrates, into phonons and electron-hole pairs (η_e), and then into heat: $\eta = \eta_p + \eta_e$. It has been suggested that [6.4, 6.5] the viscous coefficient of friction could also be described in the following way:

$$\eta = \eta_{subs} + aU_o^2 \quad (6.1)$$

Here, η_{subs} is a damping term representing the phononic or electronic energy dissipated within the substrate, and aU_o^2 represents phononic energy dissipated within the adsorbate film. The term U_o is the amplitude of the adsorbate-substrate interaction potential, which is a periodic function (sinusoidal) dependent on adsorbate position. U_o will hereafter be referred to as the surface corrugation. The factor a is dependent on temperature and coverage.

It may be possible to predict η for a given adsorbate-substrate combination. It has been hypothesized that the external modes of vibration of adsorbates on surfaces is related to η . [6.1] Whenever atoms or molecules adsorb on surfaces, new vibrational modes will emerge which are not present in either an isolated surface or the adsorbate alone. The modes which appear include both “internal”, (stretching or torsional vibrations within a molecule) and “external” modes whereby the entire molecule or atom moves as a whole with respect to the surface. Among these external modes are the frustrated (damped) translational modes (FT modes) both parallel and perpendicular to the substrate. FT phonon modes for adsorbate-substrate systems have characteristic energies that can be measured by Helium Atom Scattering (HAS) and related spectroscopies. [6.6-6.10] They can also measure the line width (defined as the lifetime or damping) of adsorbate vibrations, which is indicative of the rate at which the energy of the phonon mode is dissipated into heat. By using equation 6.1, $\eta = \eta_{subs} + aU_o^2$, as a description of the friction coefficient, parameters obtained from HAS experiments can be used as estimates for η_{subs} and U_o . The frequency of the frustrated translational modes is related to the surface corrugation, U_o . It is also hypothesized that the damping of the frustrated translational modes is related to the damping term η_{subs} .

It has been argued [6.1] that the damping or line width of the frustrated translations (γ) should be linearly proportional to the sliding friction (η). Since γ represents the energy of the phonon mode that is dissipated within the substrate, we hypothesize that changes in γ would be reflected in a changing η_{subs} term in equation 6.1:

$$\hbar\eta_{subs} = \gamma \quad (6.2)$$

Some claim that only the damping of the frustrated modes parallel to the surface should impact sliding friction. [6.1, 6.4, 6.5] This seems to be a logical argument—since sliding friction occurs when adsorbate films move parallel to a surface, the damping of the parallel phonon mode would be most closely related to the sliding friction. It could be argued, however, that any dissipation of energy could increase the sliding friction. If this is the case, then a larger damping results in higher friction whether or not the damping is associated with a parallel or perpendicular vibrational mode.

We have utilized the quartz crystal microbalance (QCM) technique to examine the sliding friction of n-octane on Cu(111) and Pb(111) surfaces. N-octane is a model lubricant, and the n-octane on Cu(111) and Pb(111) systems have been studied in recent HAS experiments. [6.2, 6.11] By examining the sliding friction of these systems, we have explored possible links between the frequency and damping of frustrated translational phonon modes and sliding friction. For n-octane/Pb(111), an energy (frequency) of 6.6 meV and damping of 0.26 meV of the perpendicular frustrated translational mode has been measured via HAS. [6.2] For n-octane/Cu(111), the energy (frequency) and damping of both the parallel and perpendicular frustrated translational modes have been measured. The energy and damping of the perpendicular phonon mode is 7.2 meV and 0.45 meV, respectively. (See figure 6.1) The energy and damping of the parallel phonon mode is 3.0 meV and 0.29 meV, respectively. [6.2, 6.11] The n-octane/Cu(111) sliding friction experiment is therefore particularly valuable, as this system has been very well-characterized by HAS measurements.

Our primary question is whether or not the damping of the perpendicular phonon modes affects friction. The n-octane on both Cu(111) and Pb(111) have similar energies,

implying that the interaction strengths of n-octane on these surfaces is also similar. However the damping for n-octane/Cu(111) is considerably larger than that of n-octane/Pb(111), by almost a factor of two. We therefore performed QCM experiments comparing the sliding friction of n-octane/Cu(111) to the sliding friction of n-octane/Pb(111).

6.2 Experimental Details

The microbalance crystals for these studies were polished 8 MHz AT-cut quartz which had quality factors near 10^5 . The Cu(111) and Pb(111) films on the QCM were prepared *in situ* in ultra-high vacuum. The base pressure of the vacuum system ranged from 8×10^{-11} to 5×10^{-10} Torr. In order to obtain n-octane slip time data, room temperature isotherms were acquired, exposing the QCM surfaces to n-octane gas [6.12] while frequency and amplitude shifts were monitored as a function of increasing pressure. The frequency shifts (δf) are proportional to the mass per unit area of the film that tracks the QCM motion. [6.13].

$$\frac{\delta f_{massloading}}{f} = -\frac{2\rho_f t_f}{\rho_q t_q} \quad (6.3)$$

Here, ρ_f and t_f are the density and thickness of the adsorbed film, and ρ_q (2.65 g/cm^3) and t_q (0.021 cm for $f = 8\text{MHz}$) are the density and thickness of the QCM. The change in amplitude (A) is proportional to the change in quality factor (Q): $\delta(Q^{-1}) = c\delta(A^{-1})$. To determine the proportionality constant, c , the samples are calibrated with helium or nitrogen gas adsorption after completion of the n-octane uptake measurements. [6.14]

Frequency and quality factor shifts can also be caused by gas pressure, tensile stress, and temperature, however these effects were negligible in this experiment. The following equation can therefore be used to calculate characteristic slip times (τ) [6.14, 6.15]:

$$\delta \left(\frac{1}{Q} \right) = 4\pi\tau (\delta f) \quad (6.4)$$

Five independent n-octane experiments contrasting Cu(111) and Pb(111) were performed, three Cu(111) experiments and two Pb(111) experiments. Thermal evaporation was used to deposit copper and lead films from 99.999% pure metal sources. For the Cu(111) samples, 80 nm of copper was deposited onto blank QCMs. Films prepared in this manner produce a mosaic structure with a (111) fiber texture [6.16]. For all samples, immediately after the deposition, n-octane was adsorbed *in situ* at room temperature onto the Cu(111) surface of the QCM. Multiple n-octane runs were performed. After the n-octane measurements, isotherms of nitrogen were acquired in order to calibrate the QCM response. After the n-octane/Cu(111) isotherms were performed, the Pb(111) samples were prepared. For two of the samples, 70 nm of lead was deposited atop the copper, again in UHV. Again, immediately after the deposition, n-octane was adsorbed *in situ* at room temperature onto the Pb(111) surface of the QCM. Multiple isotherms of n-octane and the calibration gas, nitrogen, were obtained.

6.3 Results and Discussion

We have measured the slip time at room temperature for n-octane/Cu(111) in three independent QCM experiments. The average n-octane mass uptake for the samples is shown in figure 6.2. (The frequency and quality factor shifts for the individual samples

are given in the appendix.) The average slip time data for the samples is shown in figure 6.3. Monolayer coverage of n-octane is 2.6 molecules/nm², or 0.026 molecules per square angstrom, corresponding to a frequency shift of 14.3 Hz on an 8 MHz crystal. The average slip time for a monolayer of n-octane on Cu(111) is 0.94 ns +/- 0.36 ns.

L.W. Bruch [6.17] has calculated the surface corrugation for n-octane on Cu(111) based on the energy of the FT mode parallel to the surface (3.0 meV) obtained from HAS measurements. He assumed that the backbone of the hydrocarbon was parallel to the surface of the copper, and that the copper had a nearest neighbor spacing of 0.255 nm. Based on his calculations, the surface corrugation of n-octane/Cu(111) is either 21 meV or 34 meV, depending on whether the n-octane adsorbs on top of the copper atoms (at the peak of the copper surface potential) or in the 3-fold hollow site (the well of the copper surface potential). Note that this surface corrugation amplitude is much higher than that of Xe/Cu(111), given in chapter 4, with an amplitude of 1.9 meV. This is due to the large size of the n-octane molecule as compared to the xenon. See figures 6.4 and 6.5 for contour plots of the unit cell for on the top vs. 3-fold hollow site adsorption. Using the calculations for the surface corrugation and the measurements of the slip time given here, it should be straightforward for future theorists to model the friction for the n-octane/Cu(111) system.

We compared the slippage of n-octane on Cu(111) and Pb(111) surfaces. The n-octane frequency and quality factor shifts for a representative sample are shown in figure 6.6. The average n-octane mass uptake for the three Cu(111) experiments and two Pb(111) experiments is shown in figure 6.2. The average slip time for n-octane on

Cu(111) and Pb(111) is shown in figure 6.3. The average monolayer slip times for n-octane for Cu(111) and Pb(111) is 0.94 ± 0.36 ns and 0.59 ± 0.13 ns, respectively.

Contrasting the slip times for n-octane on Cu(111) vs. Pb(111), we found that the slip time for a monolayer of octane/Cu(111) is longer than the slip time of a monolayer of octane/Pb(111). Therefore, the friction for n-octane/Cu(111) is lower (longer slip time) than the friction for n-octane/Pb(111).

Fuhrmann and Woll [6.2] found that the damping (γ) of n-octane on Pb(111) is 0.26 meV and damping of n-octane on Cu(111) is 0.45 meV. The energy of the FT_z is roughly the same (~ 7 meV). According to Persson [6.1], the friction should be linearly related to the damping of the FT mode. We have therefore observed no direct evidence that links the damping of the perpendicular FT mode to the sliding friction, according to current hypotheses. If the damping tracked the change in sliding friction, the damping for n-octane/Pb(111) should be larger than the damping for n-octane/Cu(111), which it is not.

Many theorists [6.1, 6.4, 6.5] have claimed that only the damping of the FT modes parallel to the surface should affect sliding friction. The damping of the FT parallel mode has been measured for n-octane/Cu(111) but not for n-octane/Pb(111). We can therefore not address that question in this work, however it is an interesting study for future research.

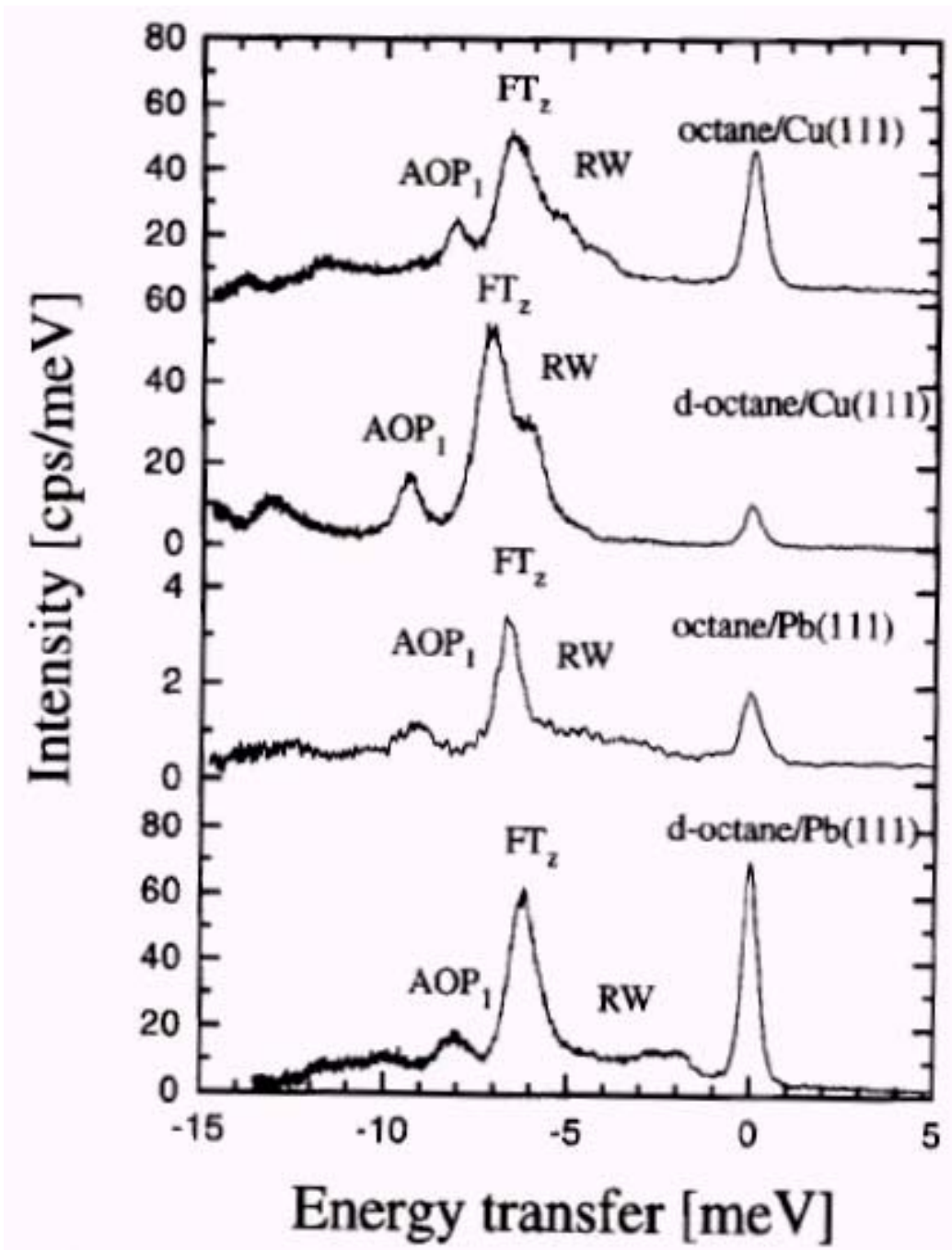


Figure 6.1. HAS data for n-octane on Cu(111) (top) and n-octane on Pb(111) (3rd from top). [6.2] Note that the FT_z peak (FT mode perpendicular to the surface) is approximately twice as wide for octane/Cu(111) as it is for octane/Pb(111). This indicates that the damping is a factor of two larger for Cu(111).

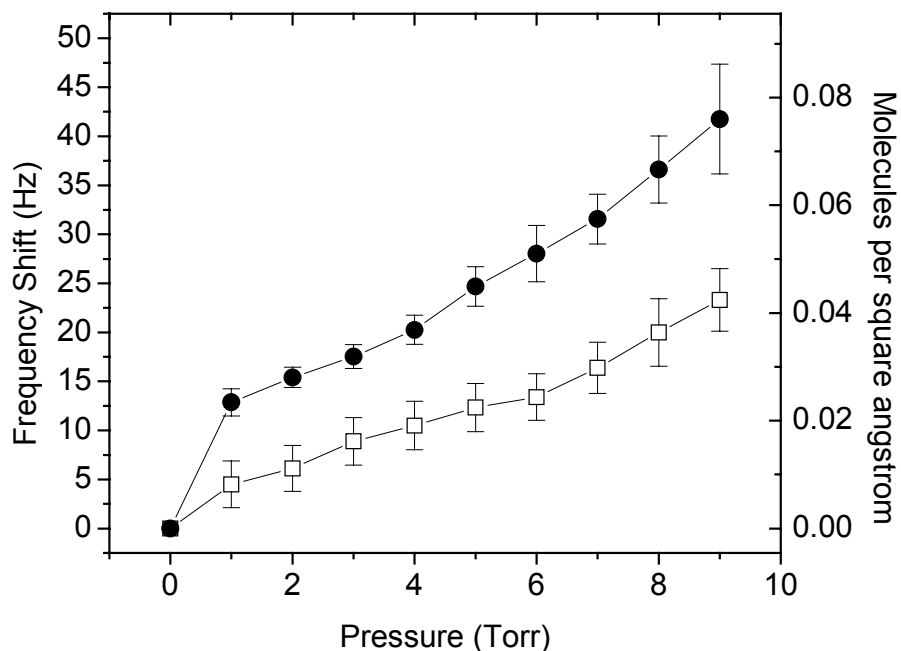


Figure 6.2. Average n-octane mass uptake on Cu(111) (open squares) and Pb(111) (closed circles). The data was box averaged from 3 Cu(111) and 2 Pb(111) independent experiments, and the error bars represent one standard deviation from the mean.

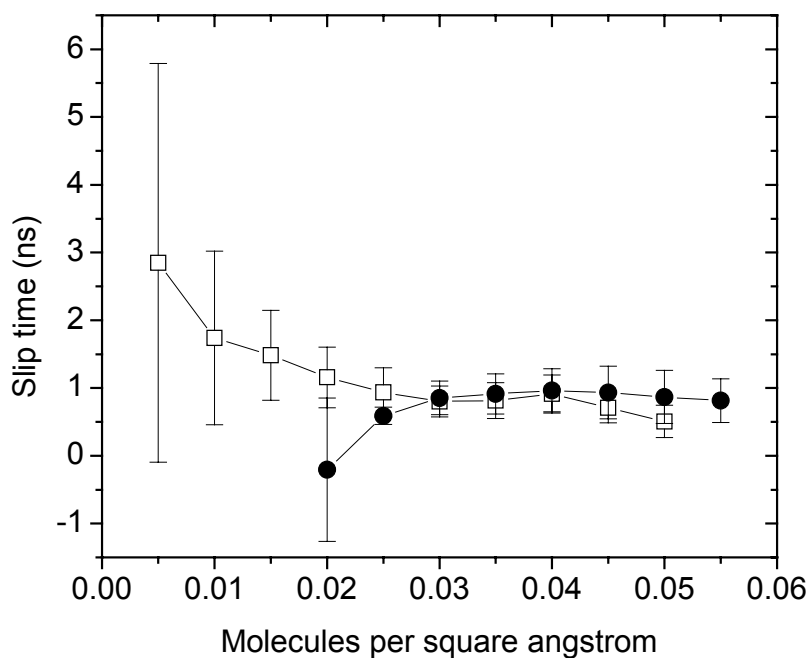


Figure 6.3. Average n-octane slip time atop Cu(111) (open squares) and Pb(111) (closed circles). The data was box averaged from 3 Cu(111) and 2 Pb(111) independent experiments, and the error bars represent one standard deviation from the mean.

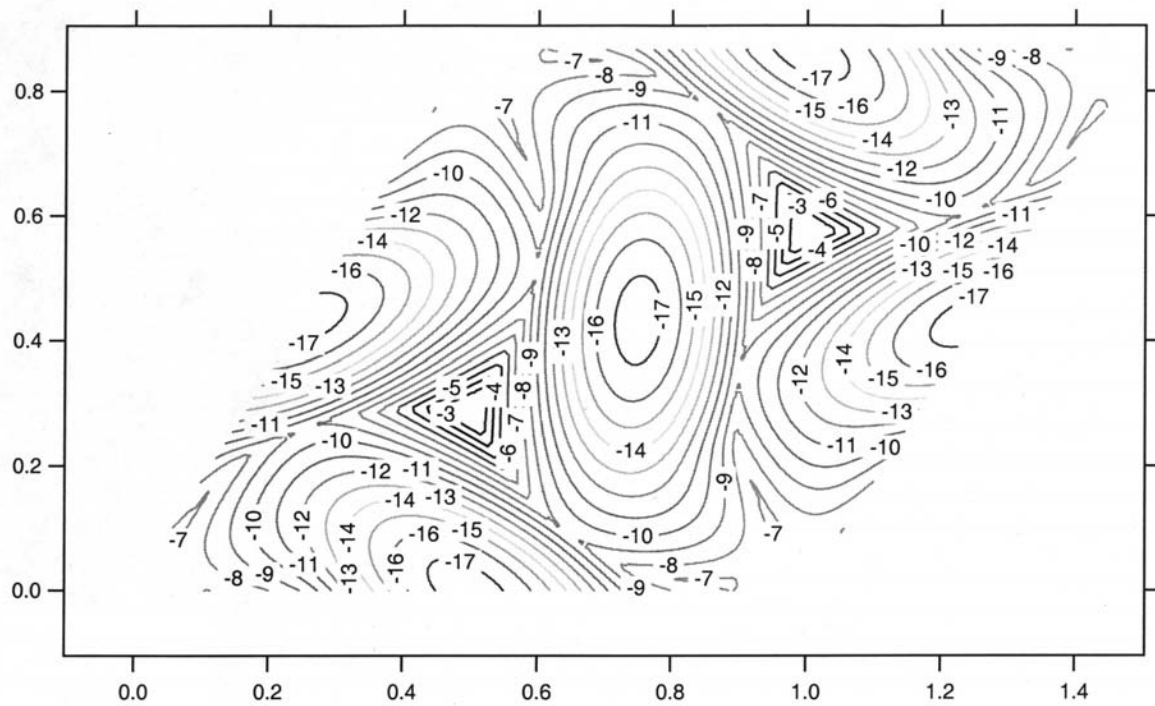


Figure 6.4. Contour plot of the unit cell for n-octane adsorption onto Cu(111). [6.17] The axes are in angstroms. The contours represent equipotential surfaces with units of meV. This plot is for n-octane in an “on the top” adsorption site, where the n-octane sits at the peak of the Cu(111) substrate potential.

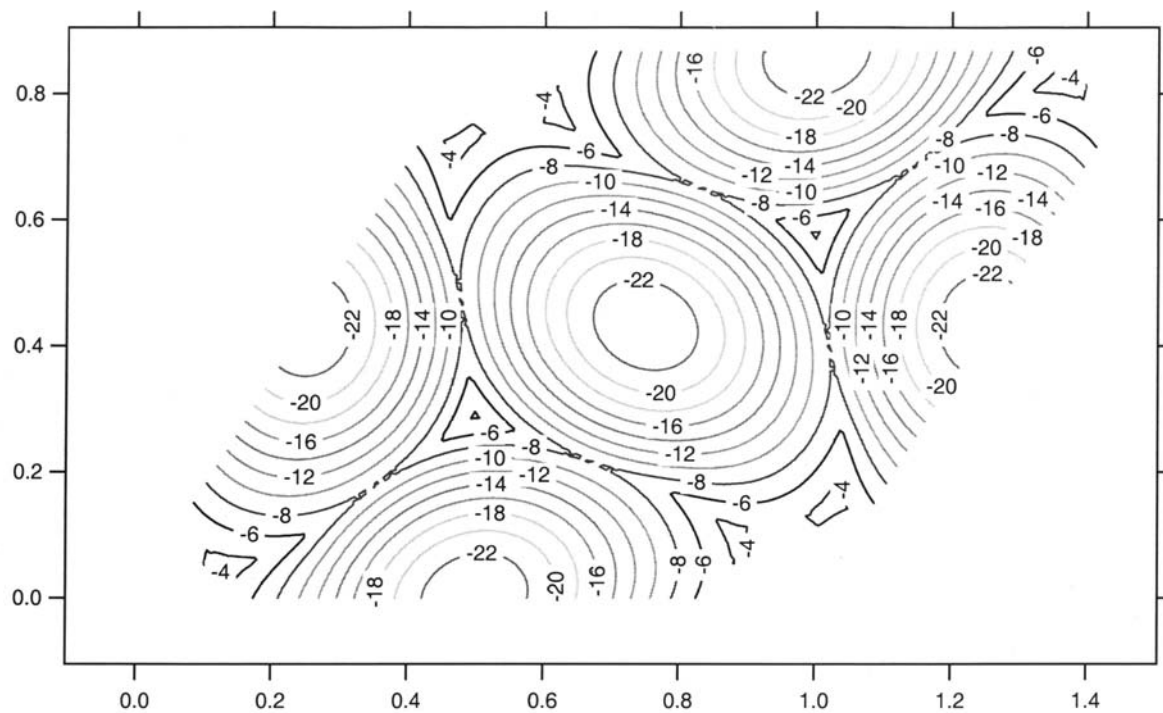


Figure 6.5. Contour plot of the unit cell for n-octane adsorption onto Cu(111). [6.17] The axes are in angstroms. The contours represent equipotential surfaces with units of meV. This plot is for n-octane in the 3-fold hollow adsorption site, where the n-octane sits at the valley of the Cu(111) substrate potential.

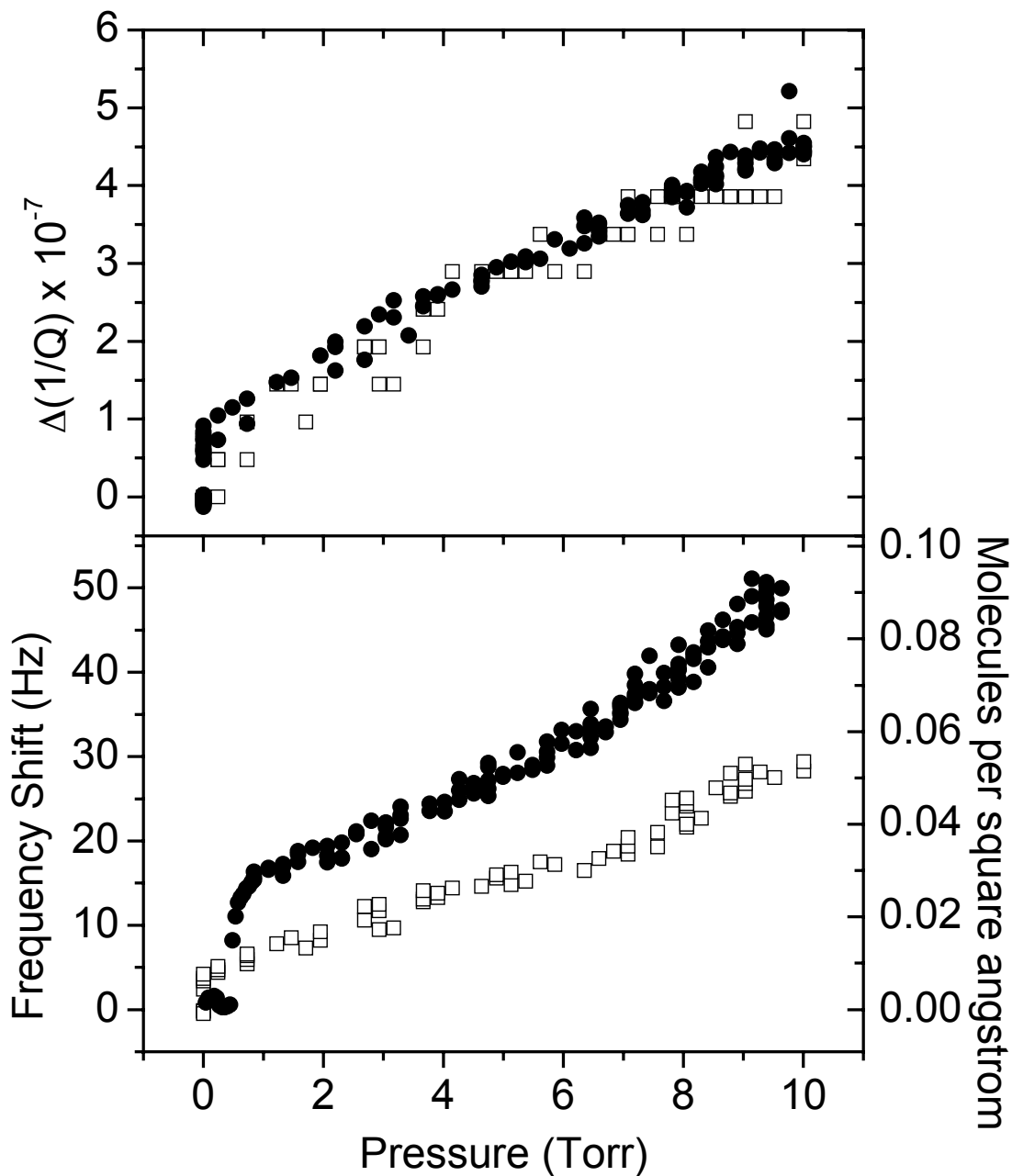


Figure 6.6. Frequency and quality factor shift for a representative sample for n-octane on Cu(111) (open squares) and Pb(111) (filled circles). The data shown here for Cu(111) is from file 043002a.dat, with a nitrogen calibration constant of 0.335 from file 050102a.dat. The Pb(111) data is from file 050302c.dat, with a nitrogen calibration constant of 0.554 from file 050302e.dat.

CHAPTER 7: QUARTZ CRYSTAL MICROBALANCE STUDIES OF THE FRICTION OF ROTATING VS. RIGID C₆₀

**manuscript in preparation for submission to Nature*

T. Coffey and J. Krim

Physics Department

North Carolina State University

Raleigh, NC 27695-8202

Abstract

Since C₆₀ was first discovered, it has intrigued tribologists. Due to its weak van der Waals interaction with most materials, its round shape, and its rapid rotation within its lattice position, there are hopes that C₆₀ will make an excellent lubricant, in analogy to nano-scale ball bearings. Although most experiments have shown that C₆₀ is a comparatively poor lubricant, the question of how the rotation of C₆₀ affects friction is still an interesting one. We have designed a Quartz Crystal Microbalance (QCM) experiment in ultra-high vacuum to determine how the rotation of C₆₀ affects slip time (friction.) In this experiment, we compare the slippage of methanol at room temperature on one monolayer of stationary C₆₀ or slowly rotating (~1 Hz) C₆₀ and two layers of quickly rotating (~10⁹ Hz) C₆₀. We found that methanol sliding on stationary and slowly rotating C₆₀ were indistinguishable. We found that methanol sliding on the stationary or slowly rotating monolayer of C₆₀ had longer slip times, or lower friction, than methanol sliding on the quickly rotating C₆₀, defying the ball-bearing analogy.

7.1 Introduction

The interesting properties and shape of C_{60} inspired scientists to imagine many diverse uses for bucky balls, from cages for the disposal of nuclear waste to nanomachine parts. When tribologists first heard of C_{60} , they were intrigued by its round shape, weak van der Waals interactions, and rapid rotation within its lattice. Because of these properties, there were hopes that C_{60} would act as a nanoscale ball bearing, and would perform well as a solid lubricant. Unfortunately, many experiments have shown that C_{60} does not make a very good solid lubricant [7.1-7.5], although it has shown some promise as an additive to liquid lubricants [7.6-7.8]. Although most experiments have shown that C_{60} is a comparatively poor lubricant, the question of how the rotation of C_{60} affects friction is still an interesting one.

C_{60} consists of 60 carbon atoms in a “soccer ball” arrangement. C_{60} is remarkably stable and non-reactive; it interacts with most materials via weak van der Waals interactions. At room temperature, it forms a face-centered cubic lattice with a nearest neighbor distance of 1.003 nm. [7.9] Within their FCC lattice positions, the C_{60} molecules rotate rapidly in random, independent directions, with rotational diffusion constants of $1.8 \times 10^{10} \text{ s}^{-1}$. [7.10, 7.11] When the bucky balls are cooled to $\sim 260 \text{ K}$, they change phase. The lower-temperature phase has a simple cubic lattice and a restricted rotation of the C_{60} , in which it ratchets between preferred orientations. [7.12, 7.13]

In a recent publication, Liang et al. reported on lateral force microscopy (LFM) studies conducted in high vacuum of a C_{60} coated tip on a crystalline C_{60} surface above and below its phase transition temperature of 260 K [7.14]. They found that the coefficient of friction, μ , was the same for C_{60} both above and below the phase transition. However, they

also found significant differences in the adhesion for C₆₀ above and below the phase transition—the adhesion was higher for C₆₀ with repressed rotation. (See figure 7.1.)

We have designed a quartz crystal microbalance (QCM) experiment to study the effect of C₆₀ rotation on friction. The QCM is an attractive technique for this study, due to its “real-world” sliding speeds and shear rates [7.15, 7.16]. The QCM has much faster sliding speeds than the LFM (~1 m/s vs. 1.5 μm/s) and hence shorter length and time scales. The friction studied with the QCM is viscous friction, $F = (m/\tau)v$, $F/A = S = \eta v$. (Here, m , τ , and v are the mass, slip time, and velocity of the adsorbates, and A , S , and η are the area, shear stress, and friction coefficient for the systems.) QCM is an extremely sensitive probe of viscous friction, capable of detecting sub-monolayer films and measuring sub-nanosecond slip times of adsorbate films on surfaces [7.17, 7.18]. Due to the shorter length and time scales, we believe that the QCM is more sensitive to small differences in friction than the LFM. Perhaps more importantly, the QCM and LFM systems have entirely different geometries, resulting in different friction laws. The QCM has an open geometry of gaseous and liquid adsorbates sliding on substrates, resulting in a viscous friction law. The LFM is a closed geometry of a solid tip sliding on a surface. For Liang et al., the friction followed Amontons’ law, $F = \mu N$, where N is the normal load.

It has been shown that at room temperature for monolayer films of C₆₀ on Ag(111), the free rotation of C₆₀ is repressed and the C₆₀ ratchets slowly between preferred orientations. For monolayer films of C₆₀ atop Cu(111), the C₆₀ does not rotate at all. For bilayer films, however, the C₆₀ molecules in the second layer rotate freely, just as they do in their FCC lattice. [7.19, 7.20] We have therefore utilized the QCM to compare the sliding of

methanol atop monolayers and bilayers of C₆₀ on Cu(111) and Ag(111) at room temperature in ultra-high vacuum (UHV). See figure 7.2. To distinguish the effects of the rotation of the C₆₀ from other effects, such as surface morphology, we have also examined the slippage of krypton atop the monolayer and bilayer C₆₀ films at 77.4 K. At 77.4 K, the C₆₀ does not rotate.

7.2 Experimental

The microbalance crystals for these studies were overtone-polished 8 MHz AT-cut quartz that had quality factors near 10⁵. For the Cu(111) sample, the copper was deposited atop a QCM with a 20 nm titanium pre-coat, to prevent roughening of the copper electrode. [7.21] The base pressure of the vacuum system ranged from 8 x 10⁻¹¹ to 5 x 10⁻¹⁰ Torr. Thermal evaporation was then used to deposit 60 nm of 99.999% pure Cu or 80 nm of 99.999% pure Ag atop the titanium pre-coat or blank QCM, respectively, producing a mosaic structure with a (111) fiber texture [7.22]. C₆₀ substrates were prepared by thermally evaporating 1 or 2 monolayers of C₆₀ atop the Cu(111) or Ag(111) electrode on a blank QCM. The QCM frequency shift was monitored during the C₆₀ deposition; one monolayer of C₆₀ corresponds to a frequency shift of 21 +/- 1 Hz, or a mass uptake of 73 +/- 4 ng/cm².

All samples were immediately transferred *in situ* to the adsorption cell where they were electrically connected to an external Pierce oscillator circuit. Adsorption isotherms of krypton and methanol were then acquired for each sample. First, the samples were chilled to 77.4 K by submersion in a liquid nitrogen bath in preparation for the krypton isotherm. After the samples had come to thermal equilibrium, they were exposed to research grade krypton

gas while frequency and amplitude shifts were monitored with increasing pressure. After acquisition of the krypton isotherm, the sample was warmed to room temperature and the krypton gas evacuated from the chamber. Samples were then exposed to research grade methanol gas while monitoring frequency and amplitude shifts with increasing pressure.

The frequency shifts (δf) are proportional to the mass per unit area of the film that tracks the QCM motion. [7.23].

$$\frac{\delta f_{massloading}}{f} = -\frac{2\rho_f t_f}{\rho_q t_q} \quad (7.1)$$

Here, ρ_f and t_f are the density and thickness of the adsorbed film, and ρ_q (2.65 g/cm³) and t_q (0.021 cm for $f = 8$ MHz) are the density and thickness of the QCM. The change in amplitude (A) is proportional to the change in quality factor (Q): $\delta(Q^{-1}) = c\delta(A^{-1})$. To determine the proportionality constant, c , we calibrated our samples with helium gas adsorption after completion of the krypton or methanol uptake measurements. [7.17] Frequency and quality factor shifts can also be caused by gas pressure, tensile stress, and temperature, however these effects were negligible in this experiment. We can therefore use the following equation to calculate characteristic slip times (τ) [7.17, 7.18]:

$$\delta\left(\frac{1}{Q}\right) = 4\pi\tau(\delta f) \quad (7.2)$$

7.3 Results

The krypton and methanol data was acquired for 8 independent samples, 4 with a monolayer of rigid or ratcheting C_{60} and 4 with the bilayer of rotating C_{60} . The frequency shift and quality factor data for a representative sample for the krypton uptake is shown in figure 7.3. This data was acquired for each krypton and methanol isotherm for every sample. The average methanol frequency shift and coverage data for the 4 monolayer vs. 4 bilayer C_{60} samples is shown in figure 7.4. Examination of the frequency shift (mass uptake) data shows that the two curves lie atop one another, within the experimental error, indicating that the adhesion of methanol on rigid and slowly ratcheting vs. rotating C_{60} systems is similar. If anything, there is a slightly faster methanol uptake on rotating C_{60} , which may indicate a slightly higher adhesion for this system. There was no difference among the 4 monolayer C_{60} samples in methanol mass uptake data for rigid vs. slowly ratcheting C_{60} .

The slip times for all 8 samples for methanol atop monolayer (rigid) and bilayer (rotating) C_{60} are shown in figure 7.5. Again, there was no difference between the 4 monolayer C_{60} samples, indicating that the methanol slippage was not dependent on whether the C_{60} was rigid or slowly ratcheting. Note that the methanol slipping on monolayer C_{60} has longer slip times than the methanol slipping on the bilayer C_{60} . The average slip times for methanol on monolayer vs. bilayer C_{60} are shown in figure 7.6. The slip times for a monolayer of methanol atop monolayer and bilayer C_{60} are 3.6 ± 1.2 ns and 1.9 ± 0.4 ns, respectively. The average slip times for krypton on monolayer vs. bilayer C_{60} (both rigid) are shown in figure 7.7. The slip times for a monolayer of krypton atop monolayer vs. bilayer

C_{60} at 77.4 K are within experimental error, 3.1 ns +/- 1.1 ns and 3.2 ns +/- 0.6 ns respectively.

7.4 Conclusion

Our experiment shows that the C_{60} rotation may cause an increase in friction, indicating that the C_{60} rotation is simply another mechanism for energy dissipation in the system. Given the similarity of the 77.4 K data for krypton sliding on monolayer vs. bilayer C_{60} films, (neither of which are rotating) we believe that the differences in the room temperature methanol slip times on monolayer (not rotating) vs. bilayer (freely rotating) C_{60} are indeed due to the C_{60} rotation, not differences in surface morphology. While we cannot preclude the possibility of rotation-dependent chemical effects that may explain our results, we know of no mechanisms or prior examples of such.

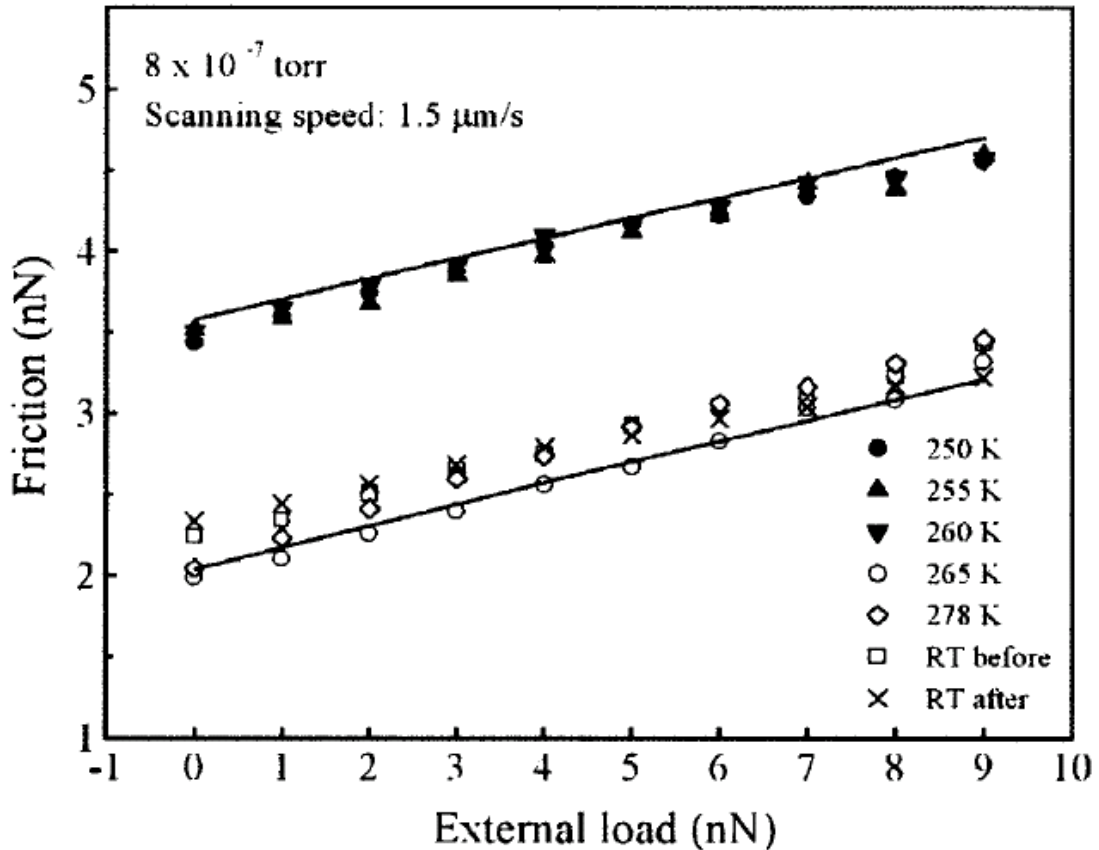
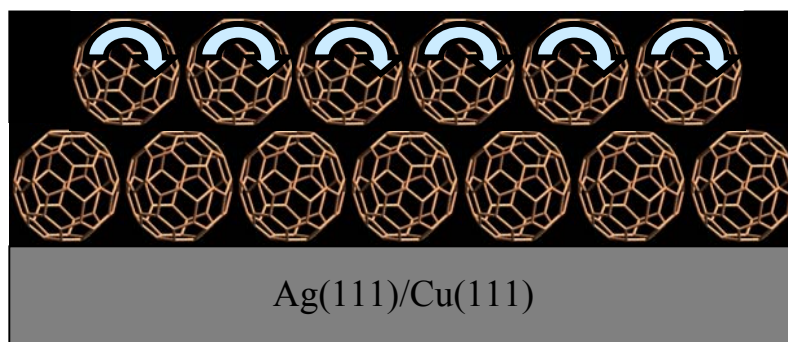
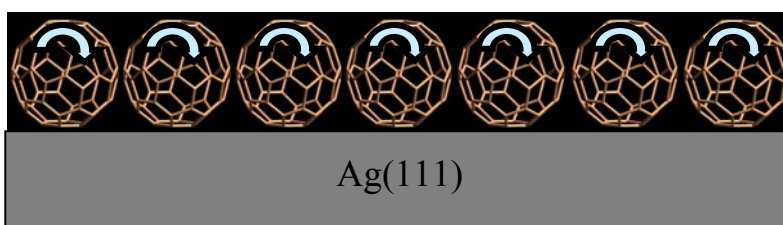


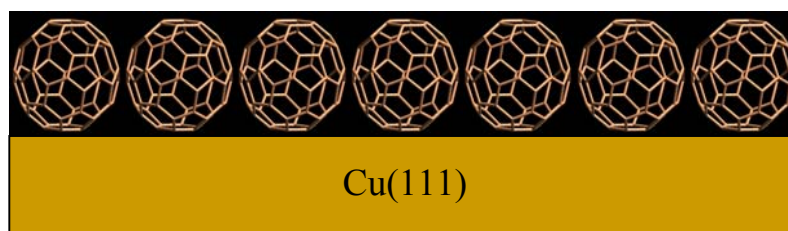
Figure 7.1. Friction vs. load curves acquired by Liang et al. [7.14] using LFM for a C₆₀ coated tip sliding on a C₆₀ crystalline surface. The closed symbols represent the hindered rotational phase of C₆₀, acquired below 260K, and the open symbols represent the freely rotating phase of C₆₀, acquired above 260K. Note that the slope of the friction vs. load curve for rotating vs. non-rotating C₆₀ is the same, but the intercept of these two curves is very different. The slope is the coefficient of friction, while the intercept is related to the adhesion.



10^9 - 10^{10} Hz



< 1 Hz



0 Hz

Figure 7.2. Schematic of our QCM experiment. On Ag(111) or Cu(111), C_{60} molecules in the 2nd layer will rotate rapidly in random, independent directions, with rotational diffusion constants of $1.8 \times 10^{10} \text{ s}^{-1}$. [7.10, 7.11] On Ag(111), C_{60} molecules in the 1st layer will ratchet slowly between preferred orientations. On Cu(111), C_{60} molecules in the 1st layer will not rotate. [7.18, 7.19]

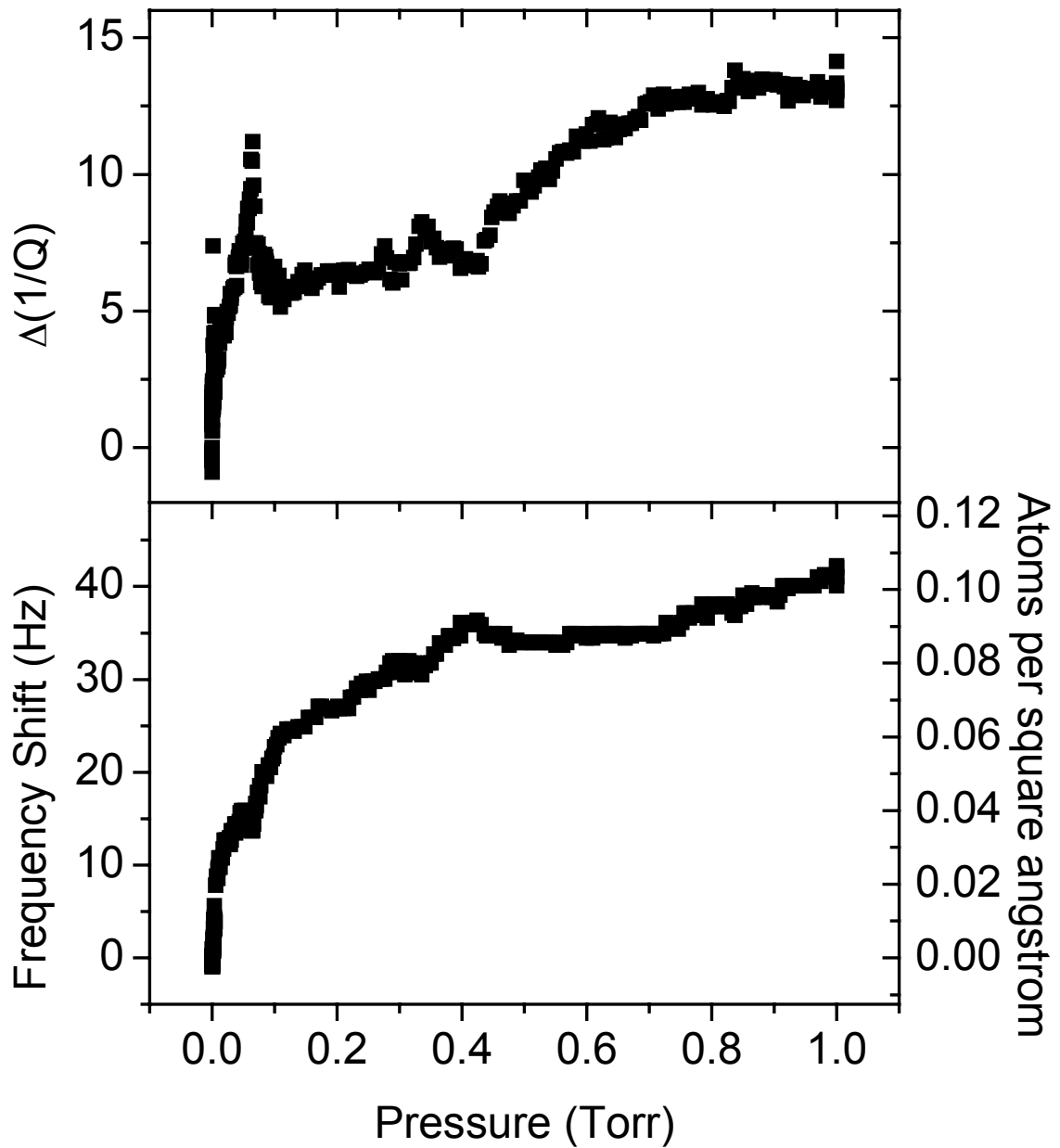


Figure 7.3. Representative frequency shift and quality factor data for krypton adsorbed onto a monolayer $C_{60}/Ag(111)$ substrate. The quality factor axis has been multiplied by a factor of 10^{-7} .

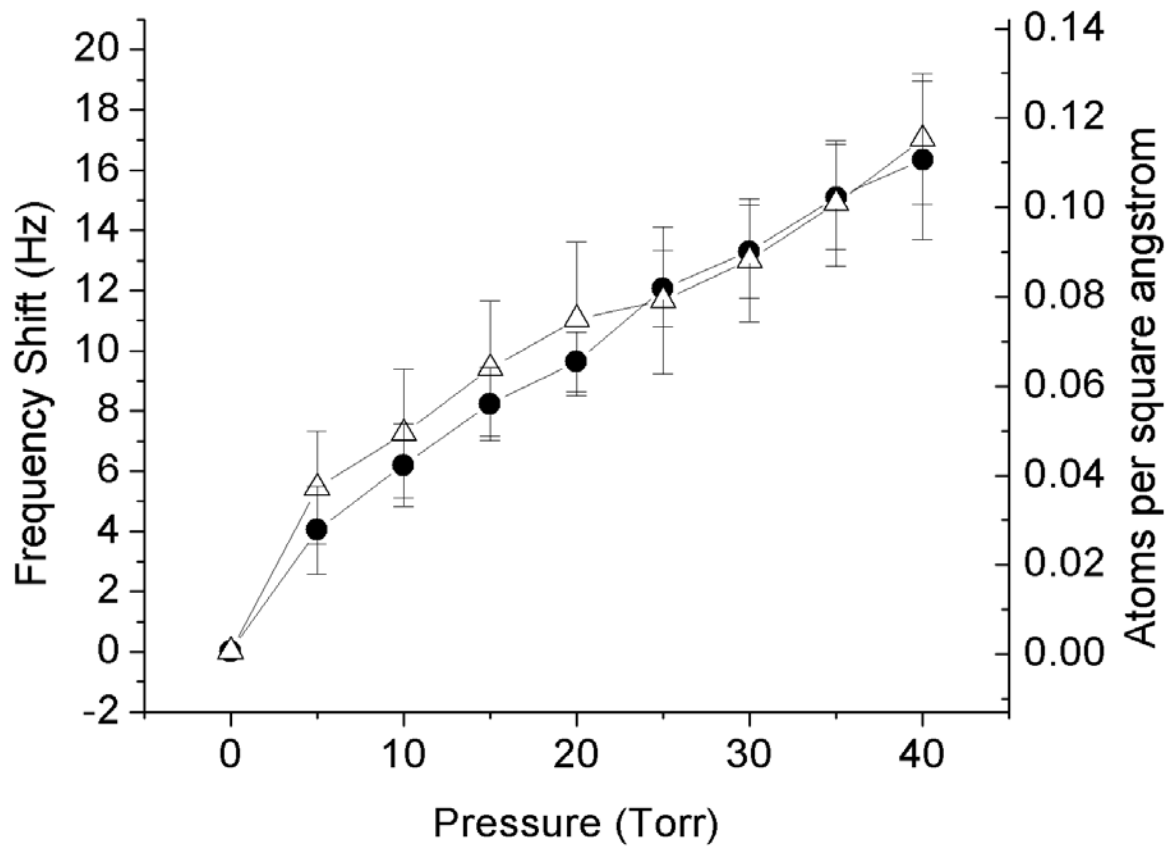


Figure 7.4. Average methanol frequency shift and coverage data for the 4 C_{60} monolayer (filled circles) and 4 C_{60} bilayer (open triangles) samples. The data sets for monolayer vs. bilayer C_{60} were box averaged to give a mean frequency shift, and the error bars represent one standard deviation from the mean.

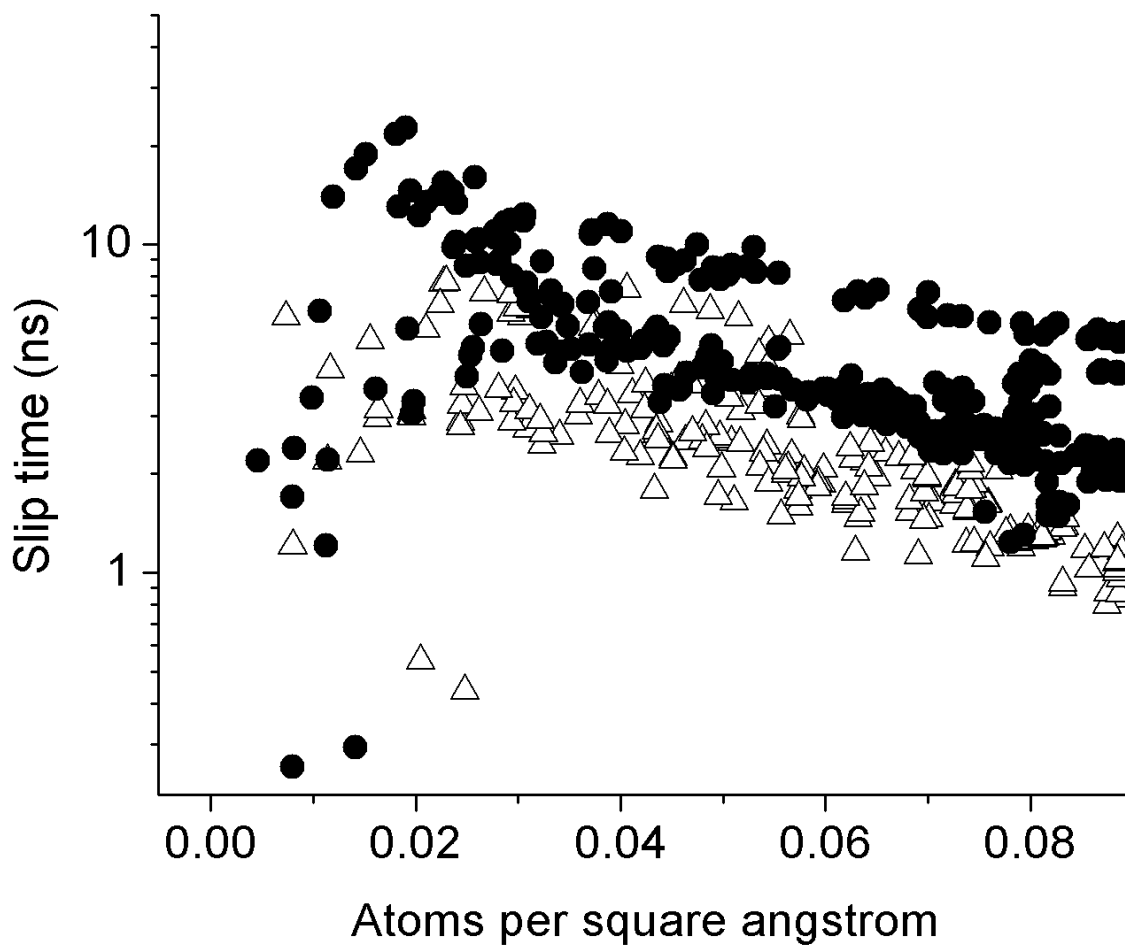


Figure 7.5. The methanol slip times for all 8 C_{60} samples. The filled circles are from the monolayer C_{60} samples, and the open triangles are from the bilayer C_{60} samples.

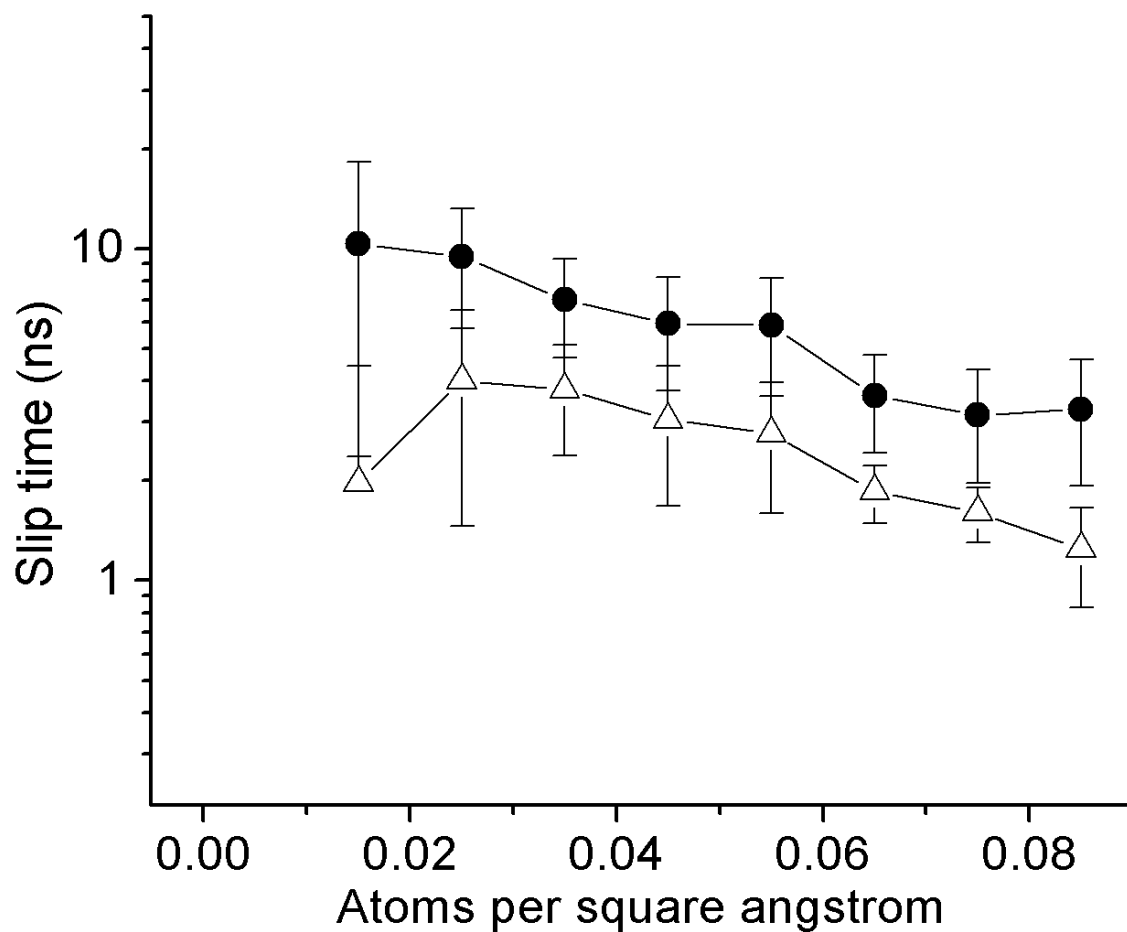


Figure 7.6. The average slip times for methanol on monolayer C₆₀ (filled circles) and bilayer C₆₀ (open triangles) samples. The 4 data sets were box-averaged to give a mean slip time, and the error bars represent one standard deviation from the mean.

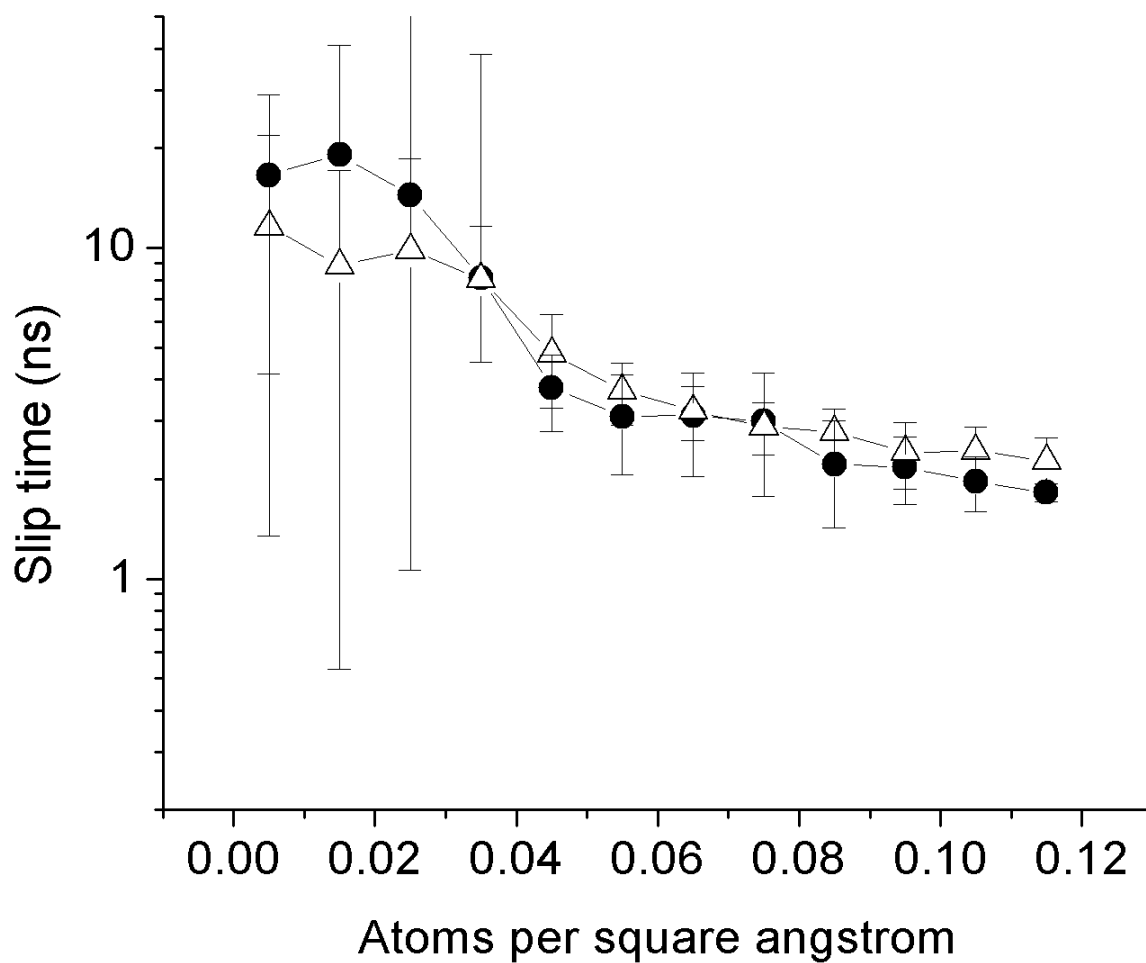


Figure 7.7. The average slip times for krypton sliding on C_{60} monolayer (filled circles) and C_{60} bilayer (open triangles) films. The 4 data sets were box-averaged to give a mean slip time, and the error bars represent one standard deviation from the mean. Due to the box-averaging of the data, the liquid-solid transition usually present in krypton isotherms cannot be seen here, although it was present in the raw data sets.

CHAPTER 8: A SCANNING PROBE AND QUARTZ CRYSTAL MICROBALANCE STUDY OF THE IMPACT OF C₆₀ ON FRICTION AT SOLID-LIQUID INTERFACES

**published in J. Phys.: Condensed Matter 13, 4991 (2001).*

T. Coffey, M. Abdelmaksoud, and J. Krim

Physics Department

North Carolina State University

Raleigh, NC 27695-8202

Abstract

We have investigated the changes in interfacial friction of toluene on mica and Ag(111) both in the presence and in the absence of interfacial C₆₀ layers employing atomic force microscope (AFM) and quartz crystal microbalance (QCM) techniques. The lateral force measurements fail to detect C₆₀ at the toluene/mica interface, presumably because the C₆₀ is dislodged by the slow-moving probe tip. In contrast, QCM measurements of interfacial friction and slippage for toluene/Ag(111) are sensitive to the presence of interfacial C₆₀. We see the friction double when C₆₀ is present. The results are discussed in the light of the full-slip boundary condition which had been previously reported for surface forces apparatus (SFA) measurements on toluene/mica in the presence and absence of interfacial C₆₀.

8.1 Introduction

Introductory treatments of the topic of friction generally begin with Amonton's Law for contacting solids:

$$F_f = \mu_s N \quad F_f = \mu_k N \quad (8.1)$$

where F_f is the force of friction, μ_s and μ_k are the coefficients of static and kinetic friction, respectively, and N is the normal load. For solid-solid interfaces, the true area of contact is usually much smaller than the apparent area of contact, due to the presence of multi-asperity contact points. As the normal force increases, the number of contacting points increases, which gives rise to Amonton's law. In contrast to solid-solid contact, the true area of contact at a solid-liquid interface is the same as the apparent area of contact, irrespective of any externally applied forces. It should therefore be of no surprise that a friction law associated with the solid-liquid geometry might not be described by Amonton's law. Indeed, for solid objects moving through a viscous retarding fluid, a retarding force of the form

$$F_f = \eta v \quad (8.2)$$

is frequently adequate, where η is a coefficient of friction and v is the relative solid-liquid velocity.

The field of nanotribology, or the study of friction and wear at submicron length scales, encompasses a number of experimental techniques involving single contact in both solid-solid and solid-liquid geometries. These techniques include probe-based methods such as atomic force microscopy (AFM), the surface forces apparatus (SFA), the quartz crystal microbalance (QCM) and the very recently developed "blow off experiment." [8.1] For

QCM, SFA, the blow off experiment, and ideally for AFM, the true area of contact is equal to the apparent area of contact. Given the unique experimental geometries involved, the appropriate friction governing nanotribological behavior is of current interest.

The AFM, SFA and QCM techniques have made important contributions to the understanding of nanotribology. The AFM was adapted for atomic-scale friction measurements in 1987 by Mate, McClelland, Erlandsson, and Chang. [8.2] AFM observations by Mate *et al.* [8.2] of a tungsten wire sliding on the basal plane of graphite were the first to directly link the structure of a surface with the dynamical frictional properties of an interface. A few years later, Germann *et al.* [8.3] demonstrated frictional forces with no load dependence; this showed a departure from the classic Amonton's law of macroscale friction. Nonetheless, most AFM measurements do in fact depend on the load, and obey Amonton's Laws. This implies a less-than-ideal tip which makes contact with the sample at multiple asperities. Germann *et al.* avoided this problem by conducting their experiments in vacuum with a carefully constructed tip.

The SFA [8.4] has been used to study the dependence of the frictional force for a range of temperatures, adhesive strengths, sliding speeds, and ambient environments. [8.5] Israelachvili and colleagues [8.6] used the SFA to study the friction between mica surfaces, and found friction to be proportional to the area of contact. Hirano *et al.* employed SFA to demonstrate that the friction between mica surfaces in a dry argon environment depended upon the commensurability of the surfaces in contact. [8.7] For SFA measurements, the frictional force is not generally linearly proportional to the applied load. However, both static and kinetic frictions are observed in the sense that a yield stress (static friction) is required to initiate sliding (kinetic friction).

The QCM has been used for decades for micro-weighing purposes [8.8], and was adapted for friction measurements in 1986-88 by Widom and Krim. [8.9-8.11] Krim *et al.*, employing a QCM, observed that solid krypton monolayers exhibited lower shear stresses than liquid krypton monolayers, or that sometimes interfaces are “slippery when dry. [8.12] QCMs were also used to show an electronic contribution to friction, by observing the change in friction in and out of the superconducting state. [8.13] Static friction has never been evident in QCM measurements, with both solid-solid and liquid-solid interfaces being well described by the viscous friction law of equation (8.2).

Mate and Marchon have recently attempted to “bridge the gap” between the QCM and SFA experimental geometries. [8.1] They focused on the fact that while both QCM and SFA measurements of the shearing of liquid films reveal viscous friction; static friction is present only in the SFA geometry. Mate and Marchon, employing a “blow off experiment,” explored whether the open geometry of the QCM, or its much greater shear rates, could account for the difference in the observed behaviors. Their results, which were performed in an open geometry at very low shear rates, yielded viscous friction, showing that the differences between QCM and SFA are due to their geometries.

By using the blow off experiment as an intermediary technique, Mate and Marchon have taken a first step in cross-referencing the various nanotribological techniques. Nonetheless, an interface comprised of identical material has never been studied by even two out of the four experimental techniques. This is because the various nanotribological probes have very different geometries and cover a different range of shear stresses, length scales, time scales, and sliding speeds, and lend themselves well to differing experimental systems. Employing the same interface to cross-reference the friction obtained by means of the

different techniques would provide understanding of how these very different techniques relate to one another and exactly how each technique measures friction. It would also enable better selection of the appropriate technique to use for studying any given system.

In order to mutually cross reference the results of various nanotribological probes and to compare nanotribological results to macro-scale, we have performed AFM and QCM investigations of the changes in interfacial friction and wetting of toluene on single crystal substrates in both the presence and absence of C_{60} adsorbed layers. We chose the system of C_{60} in toluene on mica substrates to be able to correlate our results with those of Campbell *et al.* [8.14] who employed SFA to investigate C_{60} dissolved in toluene on mica. They reported that the C_{60} adsorbed as monolayers on the mica surfaces immersed in liquid toluene. These adsorbed layers, however, interacted very weakly with each other and with the mica surface. Due to their weak interactions, the adsorbed C_{60} layers possessed unusually high fluidity, and they were easily pushed out of the way when the surfaces were approached slowly together. When the mica surfaces were sheared in the presence of the adsorbed layers, fluid flow between the two mica surfaces were reported to exhibit full-slip boundary conditions. For the pure toluene between the mica surfaces, the fluid exhibited a typical no-slip boundary condition. The C_{60} adsorbed layers therefore produced “an effective boundary of near-zero drag on the adjacent liquid.” [8.14]

Due to the round shape and the weak van der Waals interaction of C_{60} molecules, there has been much speculation on the potential lubricating properties of fullerenes. The frictional properties of C_{60} have therefore been widely investigated by a variety of techniques. In some studies, as a lubricant additive or for metal contacts, fullerenes and fullerene-like molecules have been shown to reduce friction. [8.15-8.18] Other AFM studies,

however, have shown an increase in friction for surfaces with solid film coatings of C₆₀. [8.19-8.20] Most studies of C₆₀ molecules investigate solid films adsorbed onto different substrates, and no previous studies have attempted to cross-reference the study by Campbell *et al.* of a C₆₀/toluene solution on a mica surface.

8.2 AFM Experimental Details and Results

For our contact-mode AFM measurements, we used a Molecular Imaging Pico SPM with the standard environmental chamber with RHK control electronics and software. AFM consists of a sharp tip mounted at the end of a compliant cantilever. For these measurements, the tip was held in contact with the sample surface while it was raster-scanned across the sample surface. The forces that act on the tip are determined by measuring the angular deflections of the cantilever. These forces both map out the sample surface and measure lateral forces. The MI AFM detects cantilever motion with the standard optical deflection technique. [8.21] Here, a laser beam is reflected off of the back of the cantilever onto the four-quadrant position-sensitive photodiode detector.

Topographic images were acquired by keeping the tip at zero normal loads using a feedback system. Overview images were acquired prior to friction measurements to select a smooth, flat area to avoid any topographic contribution to the lateral force. Friction measurements were conducted by raster-scanning the tip across the same 100 nm line with the feedback system disabled while varying the normal load. We then plotted lateral force vs. normal force for a friction vs. load map.

Our measurements were conducted at room temperature and pressure. For measurements acquired under liquid toluene, the AFM cantilever was completely submerged in the liquid to avoid capillary effects, and an open container of toluene was placed inside the environmental chamber to create an air/toluene vapor environment.

The measurements were conducted at low normal loads (smaller than 50 nN). Normal loads were estimated using the normal force constant of the cantilever as specified by the manufacturer (standard oxide-sharpened silicon nitride triangular cantilevers and microprobes from Digital Instruments, 0.58 N/m). Lateral forces are given in voltage (V) as measured by the photodiode without further calibration.

The high-purity C_{60} (99.5% C_{60}) was purchased from Alfa Aesar in powder form. For the AFM measurements, a solution of toluene and C_{60} was prepared by dissolving 0.1 mg C_{60} for every 1 mL of toluene in order to duplicate the SFA experiment by Campbell and colleagues as closely as possible. The lateral force microscopy (LFM) measurements of mica under toluene and mica under the C_{60} /toluene solution were carried out successively with the same cantilever on the same day. A second cantilever was used to acquire the LFM measurements comparing bare mica with mica under toluene.

Atomic-scale AFM images of toluene on mica and the C_{60} /toluene solution on mica are shown in figures 8.1 and 8.2. As shown in figure 8.1, AFM atomic-scale images acquired under pure toluene show the periodicity of the mica lattice. For the C_{60} to have an effect on the lateral force, they must form a barrier layer between the AFM tip and the mica. In our measurements, however, the C_{60} did not form the barrier layer, and were instead pushed out of the way by the AFM tip, as is shown in figure 8.2. For AFM images acquired under the C_{60} /toluene solution, the periodicity of the lattice in the image corresponds to the periodicity

of the mica lattice. As the spacing between lattice points for C₆₀ adsorbed on mica surfaces is double the spacing between lattice points for mica [8.22], we are certain that our AFM images do not show trapped C₆₀ layers.

Our results agree with those of Campbell *et al.* in the sense that we show that for the slow-moving AFM, the C₆₀ monolayers on the mica are easily disrupted, or pushed out of the way. Correspondingly, our measurements of lateral force show no difference between pure toluene on mica and the C₆₀/toluene solution on mica, as is shown in figure 8.3. We do however observe substantially higher friction for bare mica versus mica under toluene (figure 8.4). This is presumably due to the capillary forces of adsorbed water layers on the AFM tip. For all friction measurement, Amonton's Law was obeyed, indicating multiple asperity contacts between the tip and the mica surface.

8.3 QCM Experimental Details and Results

8.3.1 QCM in Vacuum

Our QCM measurements were conducted in ultra-high vacuum (UHV) to avoid monolayers of water and other surface contaminants. The microbalance crystals for these studies were polished 8 MHz AT-cut quartz that had quality factors near 10⁵. The adsorption substrates were silver electrodes deposited on the planar faces of the crystal. We produced the electrodes by evaporation of 99.999% pure Ag at 10⁻⁸ Torr onto the faces of the quartz blanks. During the desorption process the crystals were radiantly heated by the evaporation boat to temperatures over 200 C. This procedure produces a mosaic structure with a (111) fiber texture. We then adsorbed toluene onto the Ag(111) surface and monitored both the

frequency shift and change in the quality factor with increasing pressure and toluene coverage. Adsorption onto the microbalance produces shifts in both the frequency f_o and the quality factor Q , which are indicative of the degree to which the adsorbate is able to track the oscillatory motion of the underlying substrate. Characteristic slip times τ , and friction coefficients (i.e. shear stresses per unit velocity) η , are determined via the relations [8.9]

$$\delta\left(\frac{1}{Q}\right) = 4\pi\tau\delta f_o \quad \eta = \frac{\rho_2}{\tau} \quad (8.3)$$

where ρ_2 is the mass per unit area of the adsorbate. In terms of separate phonon and electron-hole slip times [8.23], τ_{ph} and τ_{eh} , the slip time τ can ideally be written as

$$\frac{1}{\tau} = \frac{1}{\tau_{ph}} + \frac{1}{\tau_{eh}}. \quad (8.4)$$

After measuring the change in frequency and quality factor for toluene on silver, we then again evacuated the chamber to UHV conditions and deposited approximately two monolayers of C_{60} onto the Ag(111). We then again adsorbed toluene onto the $C_{60}/Ag(111)$ surface and observed changes in the frequency and quality factor.

Our QCM in UHV results are shown in figure 8.5 and figure 8.6. The frequency shift of toluene adsorbed on $C_{60}/Ag(111)$ is much larger than that of toluene sliding on Ag(111) (figure 8.5). The slip time of toluene on Ag(111) is a factor two longer than the slip time of toluene on $C_{60}/Ag(111)$ (figure 8.6). The slip time is proportional to the reciprocal of the coefficient of friction, η . This means that the friction for toluene sliding on C_{60} is higher than the friction for toluene sliding on Ag(111). We observed only viscous friction, as expected.

8.3.2 QCM in liquids

The operation of a QCM in a liquid environment has become routine within the last decade. [8.24] When the electrode operates in contact with a liquid, the shear motion of the surface generates motion in the liquid near the interface. If the surface is sufficiently smooth (as are the electrodes on our QCMs), then the oscillating surface generates plane-parallel laminar flow in the contacting liquid. The response of the oscillator in such conditions depends critically on the viscosity of the fluid adjacent to the electrode, which may well exhibit a structure and viscosity which is from that of the bulk, and also on whether slippage is occurring at the interface. A variety of models have been developed to predict the oscillator response in a liquid environment, incorporating the possibility of liquid structure and interfacial slip. [8.25-8.27]

We have made preliminary measurements of a QCM with a gold electrode completely submerged in both pure toluene and the C₆₀/toluene solution. We compared the frequency shifts of the QCM between air/toluene and air/solution of C₆₀/toluene. The frequency shift of the QCM from air to the solution of C₆₀/toluene was a factor two larger than the frequency shift of air/toluene, completely consistent with the QCM in UHV measurements. This suggests that we can correlate bulk, or macroscale, QCM measurements with the monolayer, or nanoscale, measurements acquired in UHV.

8.4 Discussion

Our AFM and LFM results are well correlated with previous SFA results. [8.14] Although our LFM results do not show a significant change in the lateral force between toluene on mica and the solution of C_{60} /toluene on mica as is seen in the SFA, both SFA and AFM results show that the monolayers of C_{60} on mica are easily disrupted.

Our QCM in UHV measures slip times which are due to both the electronic and phononic contributions to friction. For the Ag(111) surface, the atomic surface corrugation is small, which means that the phononic contribution to friction will be relatively small. The large number of conduction electrons implies, however, that the electronic contribution to friction might be relatively large. When monolayers of C_{60} molecules are deposited on the Ag(111) surface, the frictional properties change dramatically. Now, the number of conduction electrons is small, which means the electronic contribution to friction will also be small. The surface corrugation, however, is quite large, which causes the phononic contribution to friction to increase. As we see the friction increase when C_{60} is present, we conclude that phononic friction is dominant for this system.

For our QCM in UHV results, we found that toluene sliding on monolayers of C_{60} deposited onto Ag(111) has a higher friction than that of toluene sliding on Ag(111). The distinguishing feature between our results and previous SFA results is the fact that C_{60} is known to chemisorb onto silver [8.28, 8.29] and physisorb onto mica. Therefore the C_{60} molecules are more likely to be mobile on a mica surface than a silver surface. This is confirmed by the fact that we saw no change in the quality factor between the bare Ag(111) surface and the layers of C_{60} on the Ag(111) surface, which indicates that the C_{60} is not

slipping on the Ag(111). (Although C_{60} does not slip on the Ag(111) surface, it is known that the C_{60} molecules freely rotate in their lattice position. [8.29]) Our results also show that the full-slip boundary condition found in previous SFA measurements [8.14] is not due to the slipping of the toluene on the C_{60} molecules. It is more likely due to the slipping of the C_{60} on the mica surface.

8.5 Future Work

An ideal cross-referencing experiment would measure the same interface with different techniques, have the same basic geometry, and be simultaneously measured, ensuring identical conditions. An experiment satisfying these criteria would be a comparison of QCM with the blow-off technique. The QCM and the blow-off experiment both have open geometries and measure viscous friction. It would also be possible to place the blow-off apparatus atop the QCM, and acquire both QCM and blow-off measurements simultaneously.

Recent theoretical papers [8.30] have postulated a link between the wetting behavior of a liquid on a solid and the friction at the solid-liquid interface. In a future experiment, we will test this postulate by comparing contact angle measurements with QCM and AFM measurements of the friction at the interface. It is known that C_{60} chemisorbs onto both copper and silver substrates [8.28, 8.29]. However, C_{60} molecules are able to freely rotate in their fixed lattice position on Ag(111), but they are not free to rotate on Cu(111). [8.29] We will deposit monolayers of C_{60} onto both Ag(111) and Cu(111) surfaces in UHV, and then measure the contact angle of toluene on $C_{60}/Ag(111)$ and $C_{60}/Cu(111)$ surfaces. We will then

employ QCM and AFM to measure the friction on these surfaces, and see if a correlation exists between the wetting behavior and the friction.

Acknowledgements

This work has been supported by NSF grant No. DMR0072030 and AFOSR grant No. F49620-98-1-0201 and a Department of Education GAANN Fellowship.

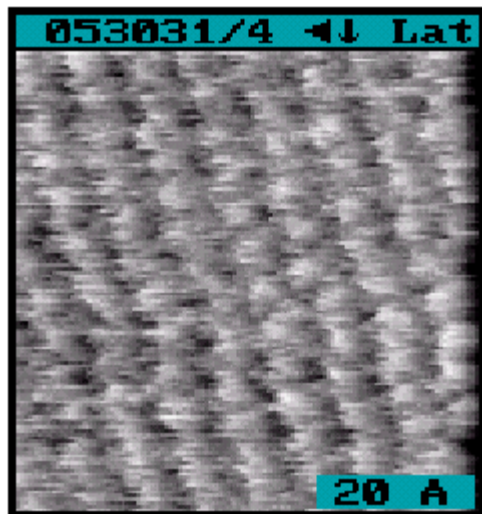


Figure 8.1. An AFM atomic-scale image of the mica lattice submerged in toluene.

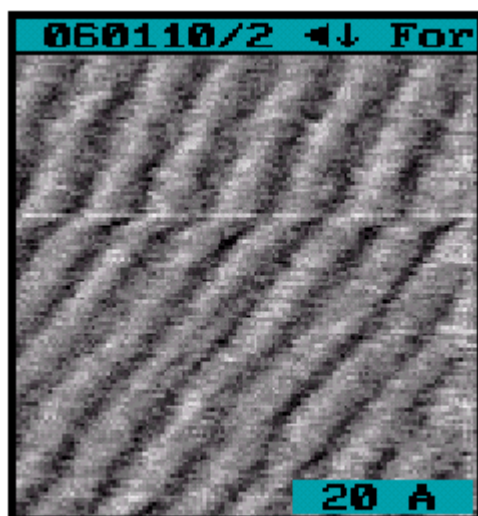


Figure 8.2. An AFM atomic-scale image of the mica lattice submerged in the C_{60} /toluene solution.

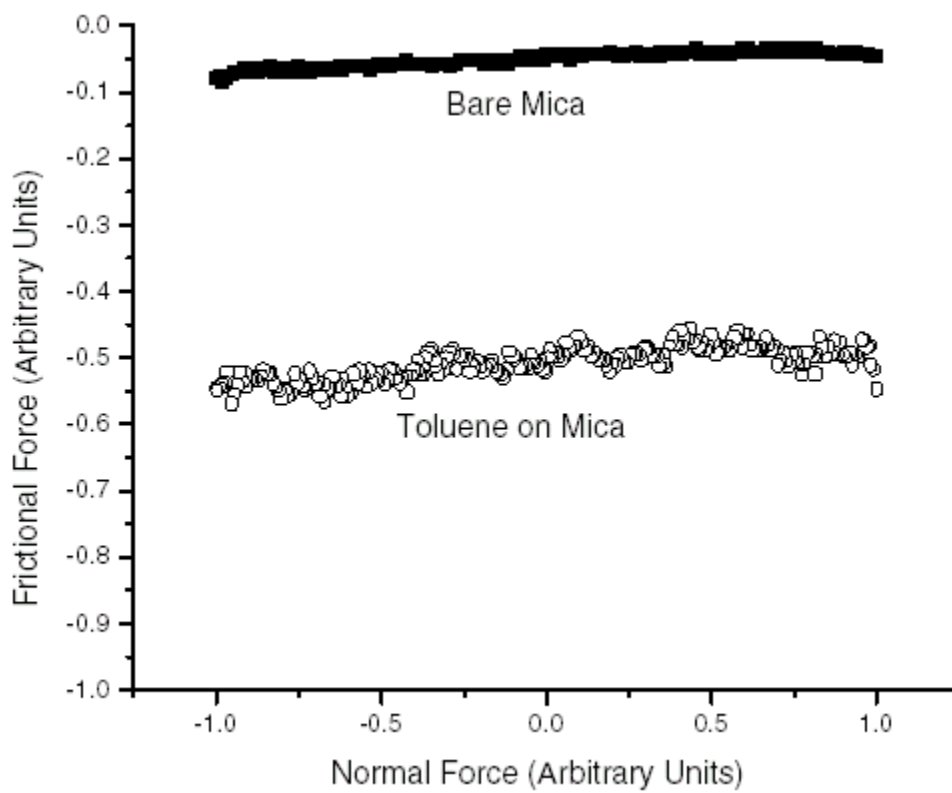


Figure 8.3. Frictional force vs. normal force for bare mica in air vs. mica submerged in toluene.

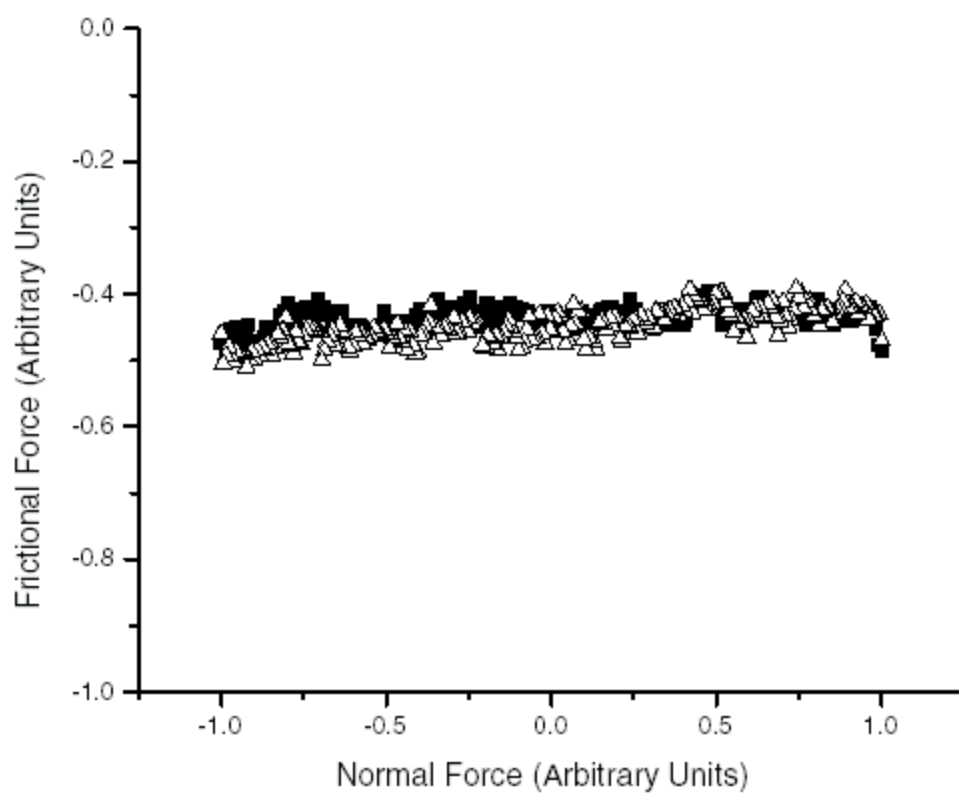


Figure 8.4. Frictional force vs. normal force for mica submerged in toluene vs. mica submerged in the C_{60} /toluene solution. The two data sets are indistinguishable from one another.

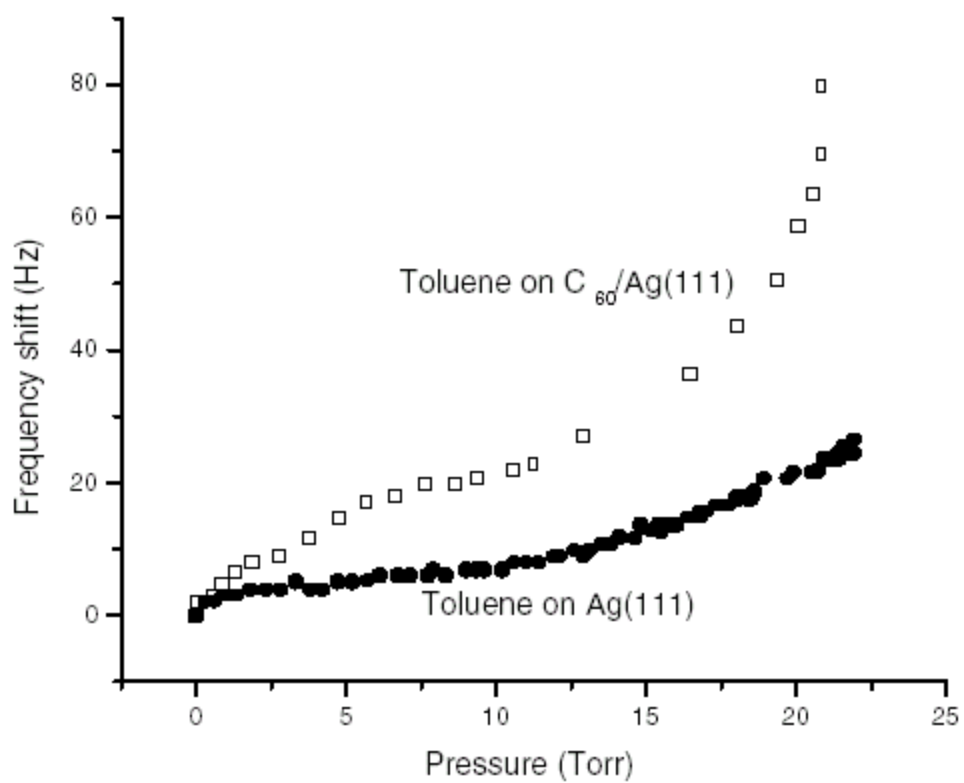


Figure 8.5. QCM frequency shifts for toluene on Ag(111) and toluene on C₆₀/Ag(111). The difference in the frequency shift curves is due to the wetting [8.31].

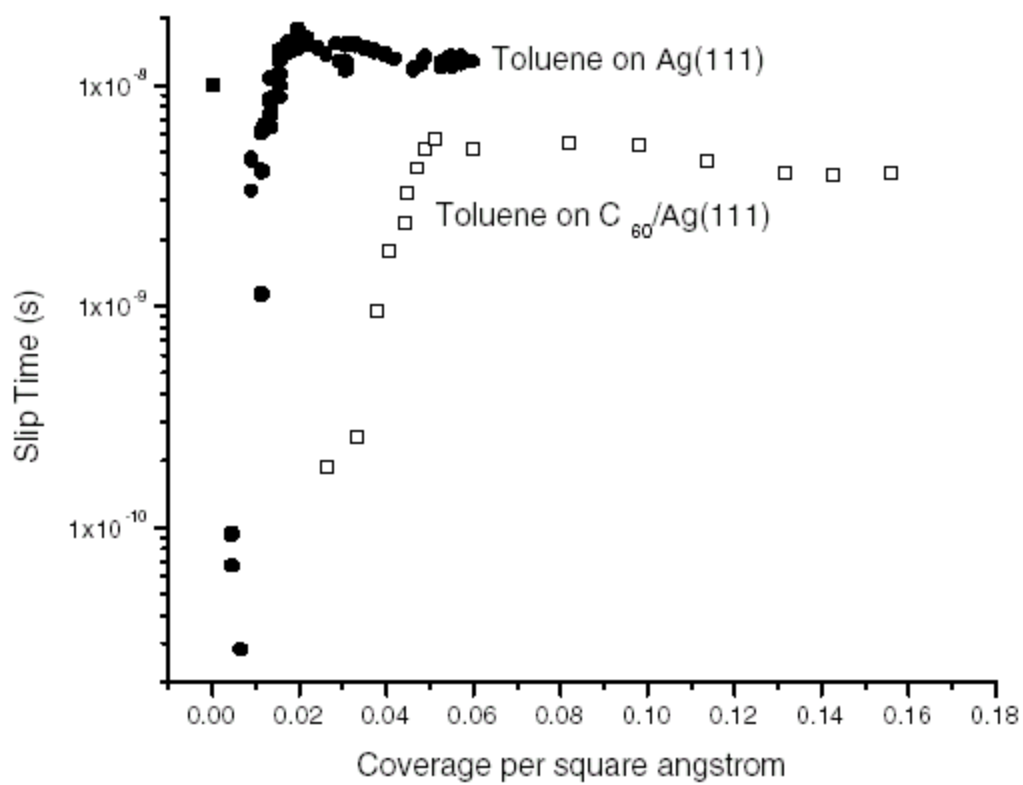


Figure 8.6. QCM slip times for toluene on Ag(111) and toluene on $C_{60}/Ag(111)$. The slip time is proportional to the reciprocal of the coefficient of friction, η . This means that the friction for toluene sliding on C_{60} is approximately twice the friction for toluene sliding on Ag(111).

CHAPTER 9: CONCLUSIONS

In this work, I have used the Quartz Crystal Microbalance (QCM) to study the nanoscale friction of monolayer adsorbates on (111) metals. The friction of these systems is viscous friction, defined as $F_f = \eta v = \left(\frac{m}{\tau}\right)v$. Here, η is the viscous coefficient of friction, v is the velocity of the adsorbate, m is the adsorbate mass, and τ is the slip time, which is the time it takes for the film's speed to fall to $1/e$ of its original value. The main focus of this dissertation was to determine the factors that control η , the viscous coefficient of friction.

We investigated the validity of an equation for predicting the viscous coefficient of friction: $\eta = \eta_{subs} + aU_o^2$. Here, η_{subs} is the damping of adsorbate sliding energy within the substrate, a is a constant depending on mainly temperature and adsorbate film coverage, and U_o is the atomic-scale surface corrugation. In Chapter 4, I closely examined the effect of varying U_o while holding the lattice spacing relatively constant by studying the slippage of xenon films on Cu(111), Ni(111), graphene, and C₆₀ substrates at 77.4 K. It was found that the slippage of xenon on Cu(111), Ni(111), and graphene/Ni(111) was very well fit by the proposed equation. These three systems had very similar nearest neighbor lattice spacings (0.255 nm, 0.249 nm, and 0.249 nm, respectively) but varying atomic scale surface corrugations (1.9 meV, 14 meV, and 5.3 meV, respectively.) The xenon monolayer slip times (τ) of 15.5 ns, 0.41 ns, and 1.7 ns, respectively, were well fit by the relation $\tau \propto U_o^{-2}$. Specifically, when plotted on a $\ln \tau$ vs. $\ln U_o$ plot, the data were fit by a slope of -1.82 ± 0.20 .

In Chapter 5, I examined the slippage of solid and liquid krypton monolayers on Cu(111), Ag(111), Ni(111), and C₆₀ substrates at 77.4 K. I documented the liquid-solid phase transition and compared the slip times of the krypton for the various substrates. The slip times for the solid krypton monolayers are longer than the slip times for liquid krypton monolayers on metal substrates and monolayer C₆₀ films, as observed previously for krypton/Au(111). However, this jump is not as large as that previously observed for krypton/Au(111) surfaces. The slip time for liquid and solid krypton monolayers is slightly longer atop C₆₀ bilayer films than C₆₀ monolayer films. However, for bilayer C₆₀ films, the jump in slip time at the liquid-solid phase transition is not present. Although the damping and atomic scale corrugation is not known for all of these systems, they are ideal for further study and future modeling.

In Chapter 6, I have examined the effect of varying η_{subs} while controlling other parameters by studying the slippage of n-octane films on Cu(111) vs. Pb(111) surfaces at room temperature. It has been proposed that η_{subs} should be linearly proportional to the damping of frustrated translational (FT) phonon modes (γ) of an adsorbate-substrate system via $\gamma = h\eta$. The parallel FT modes are believed to be directly linked to the sliding friction, but it is not clear how damping of the perpendicular FT modes (FT_z) affect sliding friction. To explore this question, I have examined the sliding friction of n-octane on Cu(111) vs. Pb(111) surfaces. The damping of these surfaces has been measured as $\gamma = 0.45$ meV and $\gamma = 0.26$ meV, respectively. I observed that the monolayer slip time for n-octane/Cu(111) is longer (lower friction), 0.94 ± 0.36 ns, than the slip time of n-octane/Pb(111) (higher friction), 0.59 ± 0.13 ns. Using $\gamma = h\eta$, I therefore observed no direct evidence that the

damping of the perpendicular FT modes affects sliding friction. It is still possible, however, that the damping of the parallel FT phonon mode affects sliding friction.

In Chapter 7, I studied the slippage of monolayer methanol films at room temperature on rotating, rigid, and slowly ratcheting C_{60} substrates, to examine the effect that the molecular rotation of the substrate surface has on the sliding friction of an adsorbate. It had been hypothesized that the rotation of the C_{60} molecules might reduce friction, because the round, rotating C_{60} could act as a nanoscale ball bearing. I found that the slippage and mass uptake for methanol on rigid and slowly ratcheting C_{60} was indistinguishable. I found that at all coverages, the slip time for methanol on rigid and slowly ratcheting C_{60} was longer (hence lower friction) than the slip time for methanol on rotating C_{60} , defying the ball bearing analogy.

Finally, in Chapter 8, I investigated the changes in interfacial friction of toluene on mica and Ag(111) both in the presence and in the absence of interfacial C_{60} layers employing atomic force microscope (AFM) and quartz crystal microbalance (QCM) techniques. The lateral force measurements failed to detect C_{60} at the toluene/mica interface, presumably because the C_{60} was dislodged by the slow-moving probe tip. In contrast, QCM measurements of interfacial friction and slippage for toluene/Ag(111) are sensitive to the presence of interfacial C_{60} ; the friction doubled when C_{60} is present. For the Ag(111) surface, the atomic surface corrugation is small, which means that the phononic contribution to friction will be relatively small. The large number of conduction electrons implies, however, that the electronic contribution to friction might be relatively large. When monolayers of C_{60} molecules are deposited on the Ag(111) surface, the frictional properties change dramatically. Now, the number of conduction electrons is small, which means the electronic

contribution to friction will also be small. The surface corrugation, however, is quite large, which causes the phononic contribution to friction to increase. Since the friction doubled in the presence of C_{60} , we concluded that phononic friction is dominant for this system.

APPENDIX

The appendix contains supplementary and supporting data sets and shows the frequency and quality factor shifts for data sets contained in the box averaged results from chapters 4-7.

Helium or nitrogen calibration information is also given in the figure captions and tables for all data.

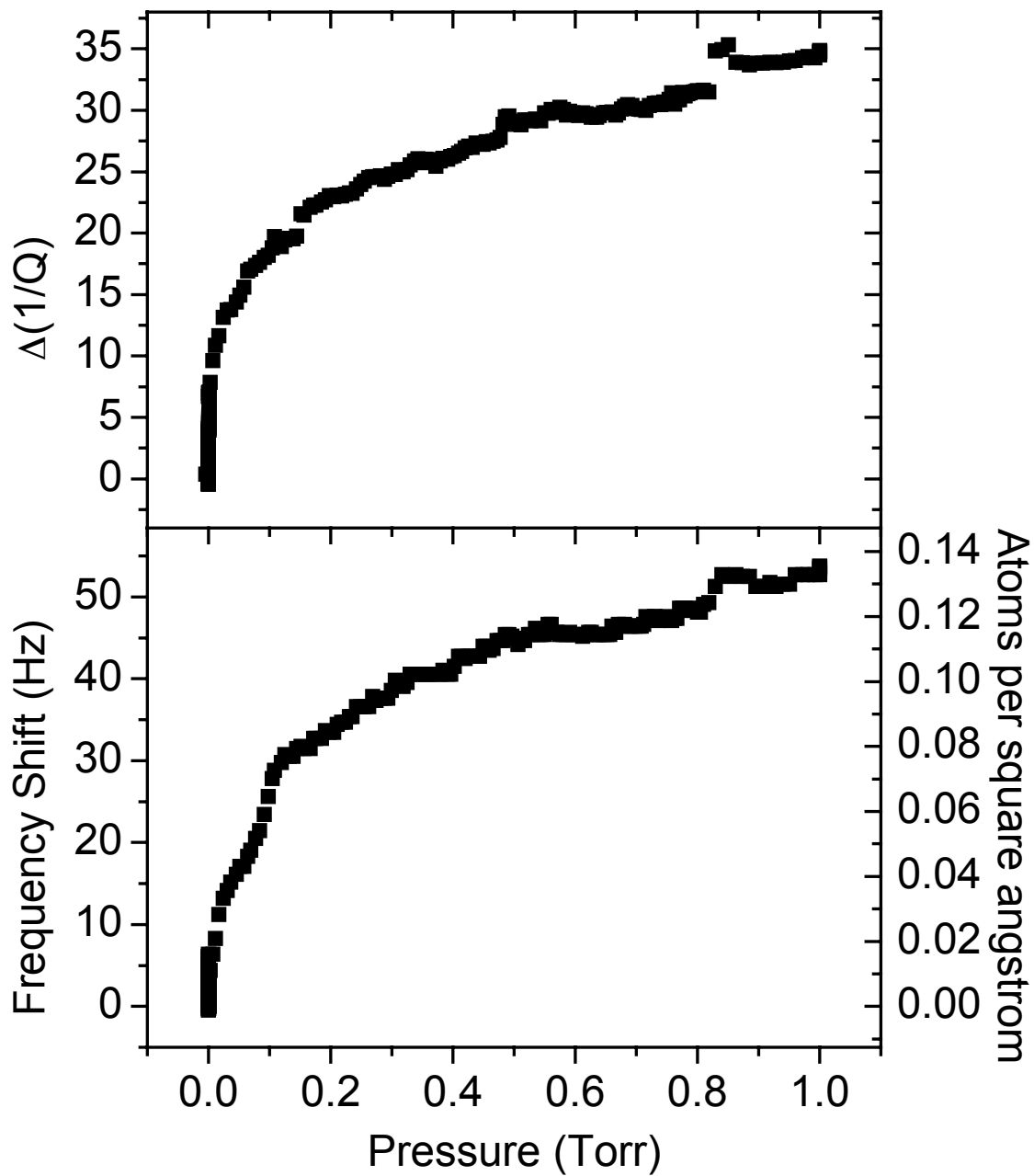


Figure A.1. Kr/Ag(111), 120503a.dat. Supporting data set for Chapter 5. Helium calibration constant (Hecal constant) = 0.8245; calibration file 120503b.dat.

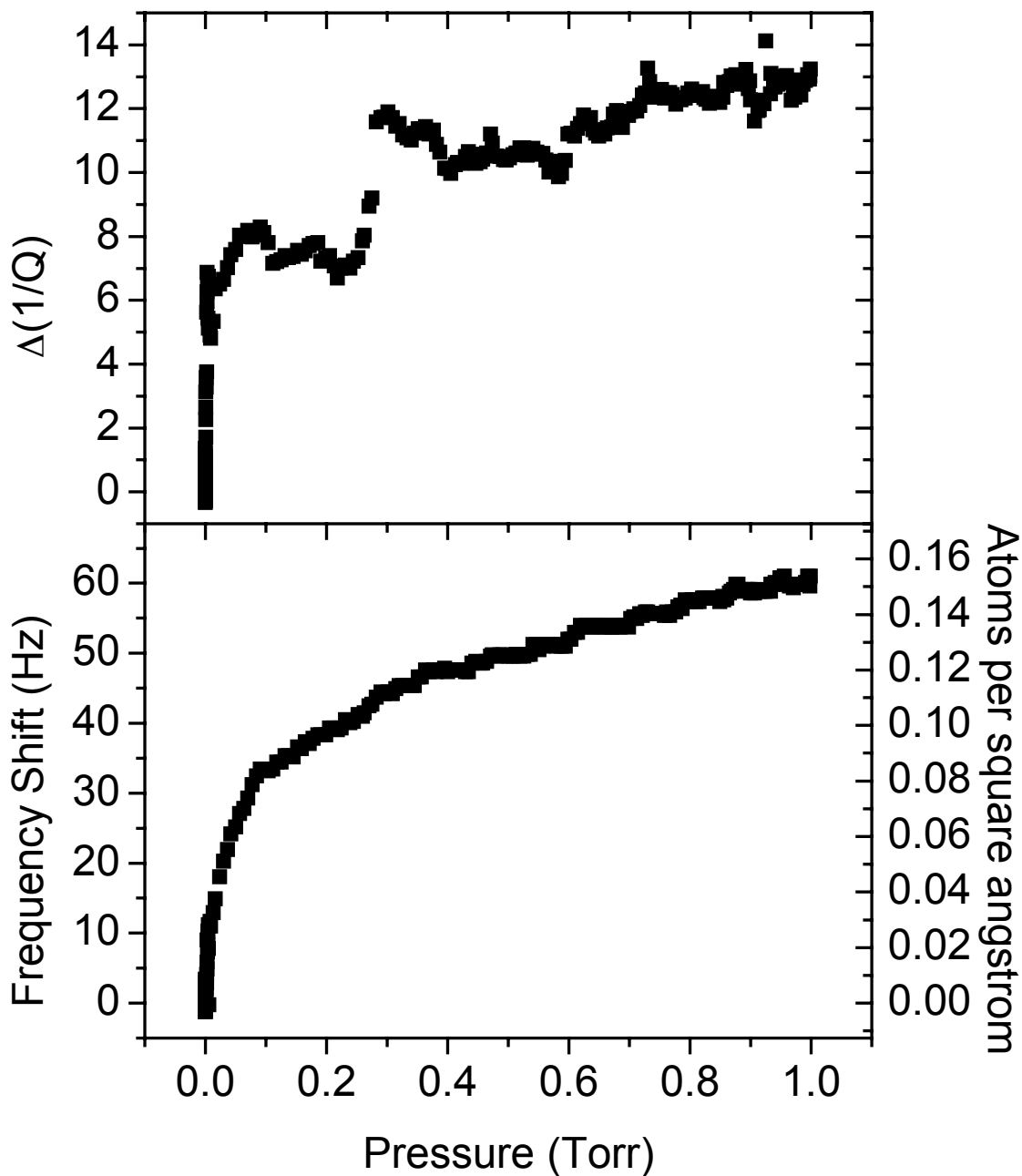


Figure A.2. Kr/monolayer $C_{60}/Ag(111)$, 121103a.dat. Supporting data set for Chapter 5 and contained in the box averaged krypton slip times for Chapter 7. Hecal constant = 0.575; calibration file 121103b.dat.

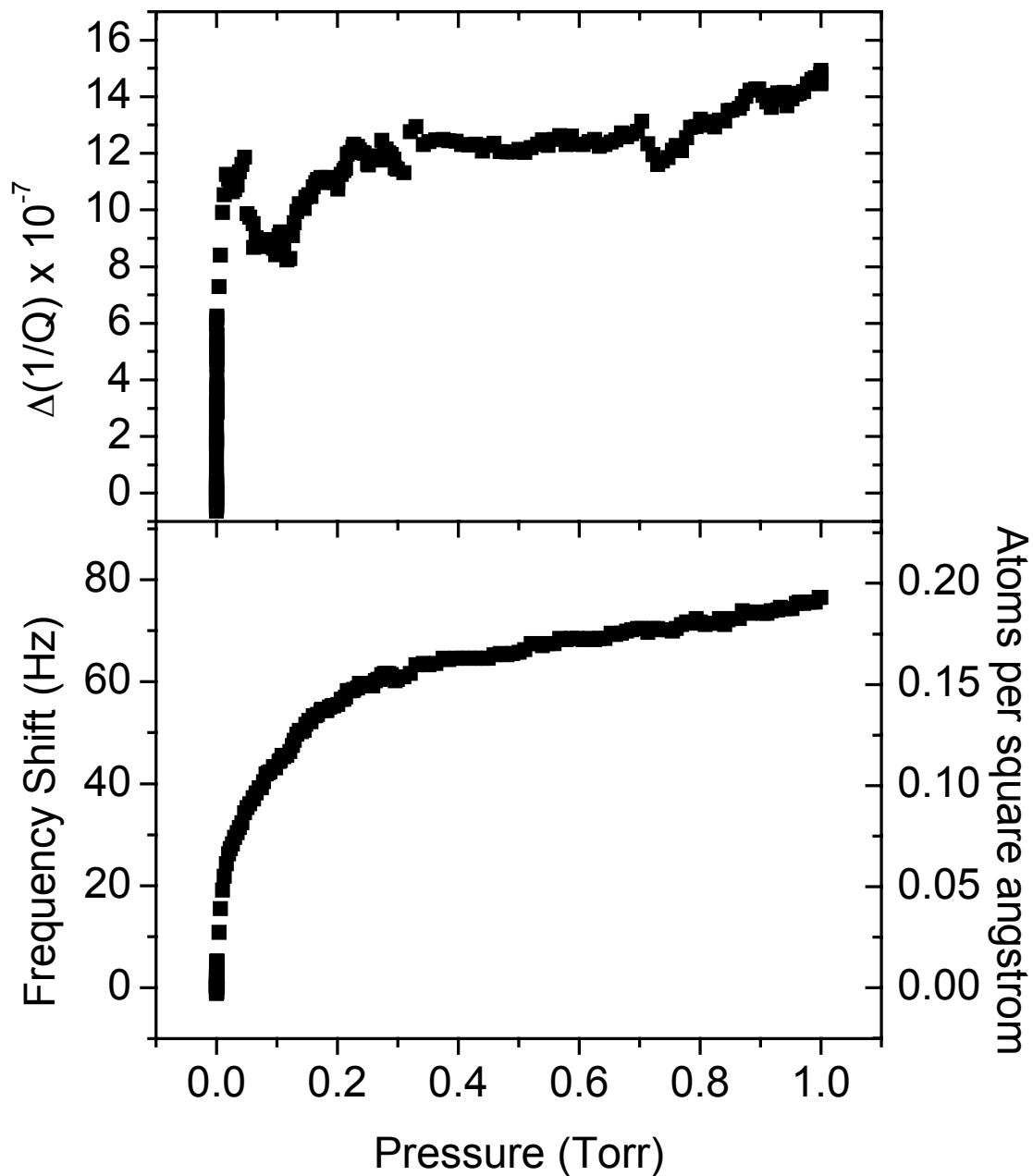


Figure A.3. Kr/bilayer $C_{60}/Ag(111)$, 121703a.dat. Supporting data set for Chapter 5 and contained in the box averaged krypton slip times for Chapter 7. Hecal constant = 0.686; calibration file 121703b.dat.

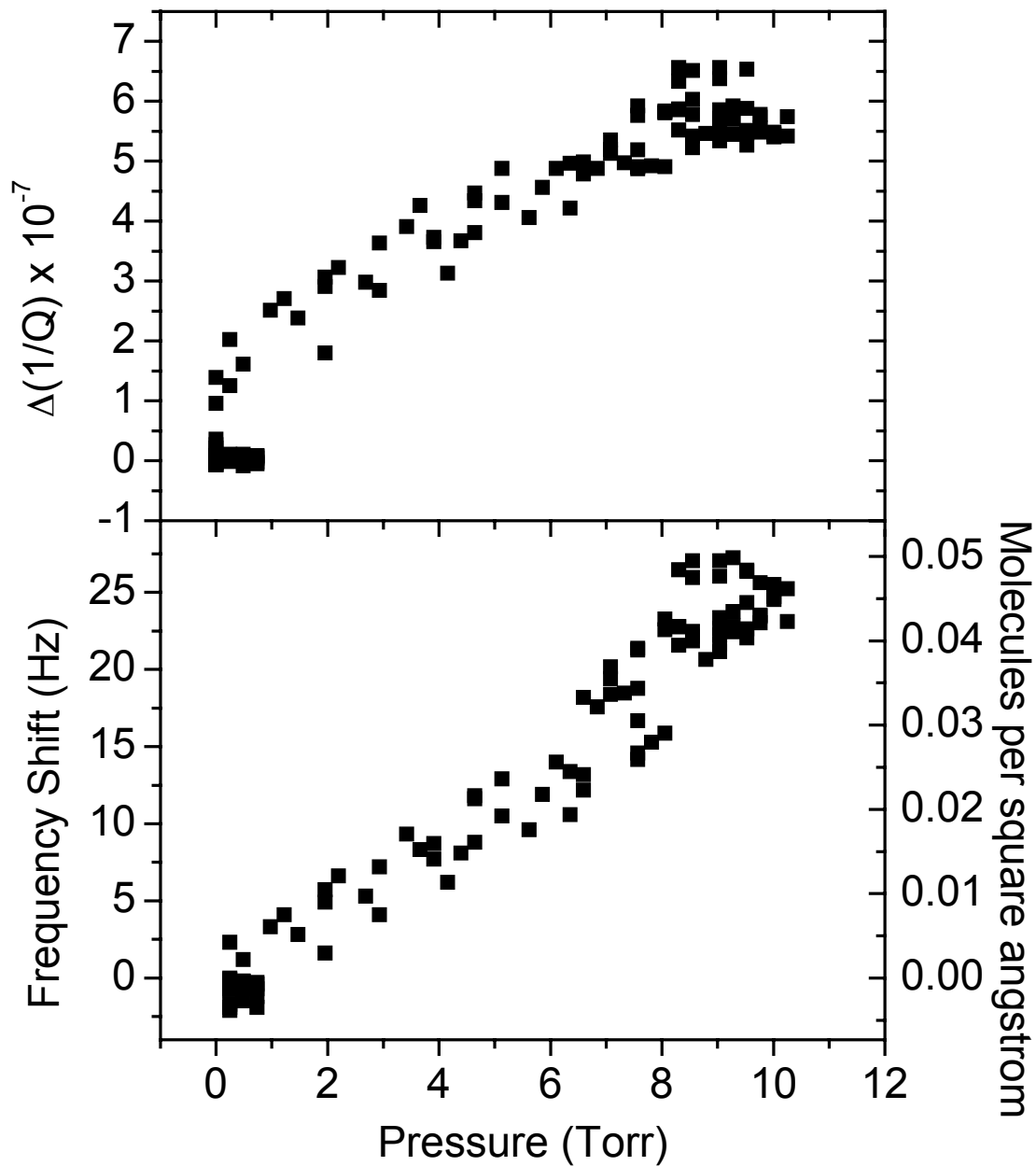


Figure A.4. N-octane/Cu(111), 061902c.dat. Data shown in average n-octane mass uptake and slip time, Chapter 6. Nitrogen calibration constant = 0.732; calibration file 061902f.dat.

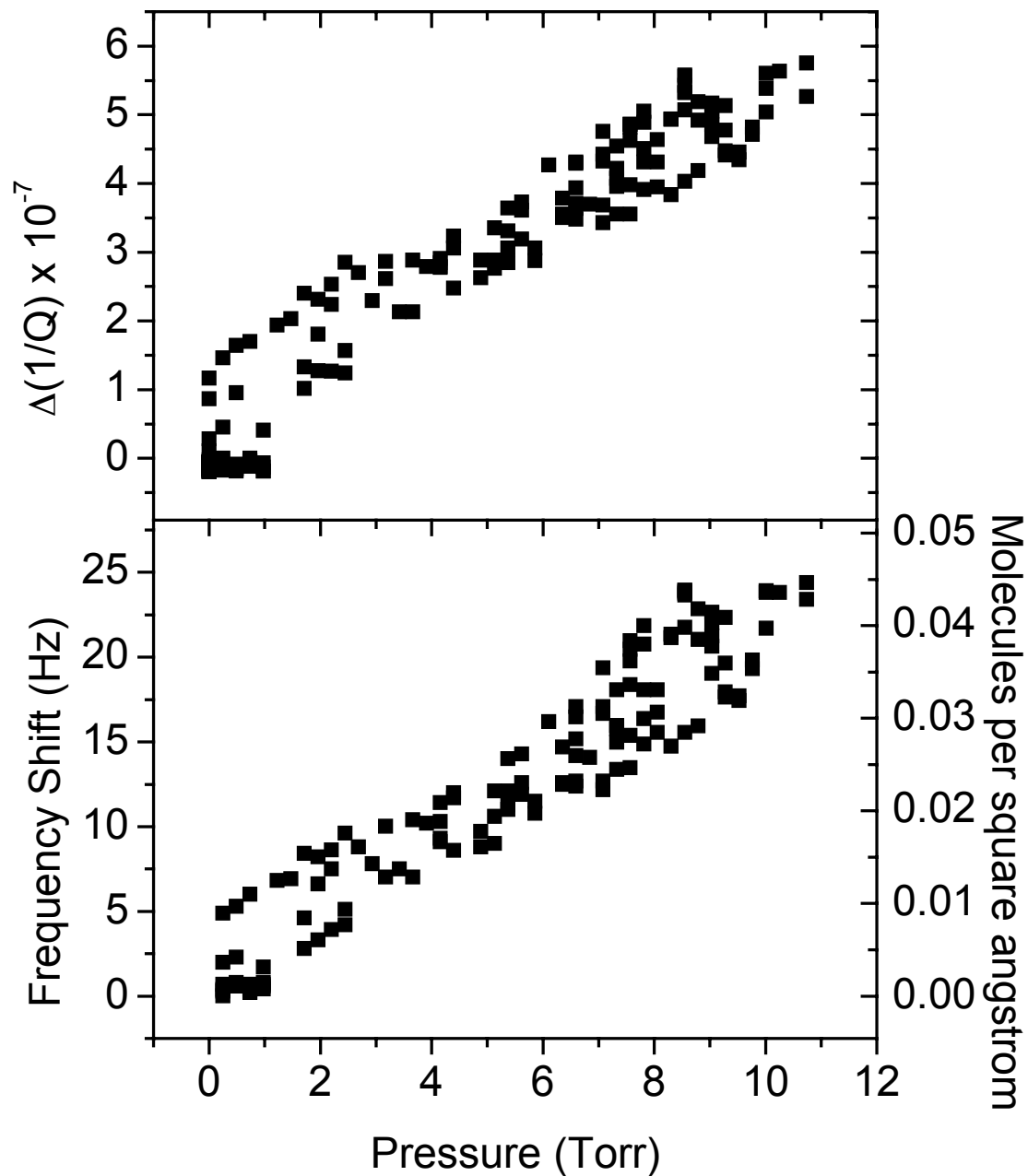


Figure A.5. N-octane/Cu(111), 070202c.dat. Data shown in average n-octane mass uptake and slip time, Chapter 6. Nitrogen calibration constant = 0.751; calibration file 070202e.dat.

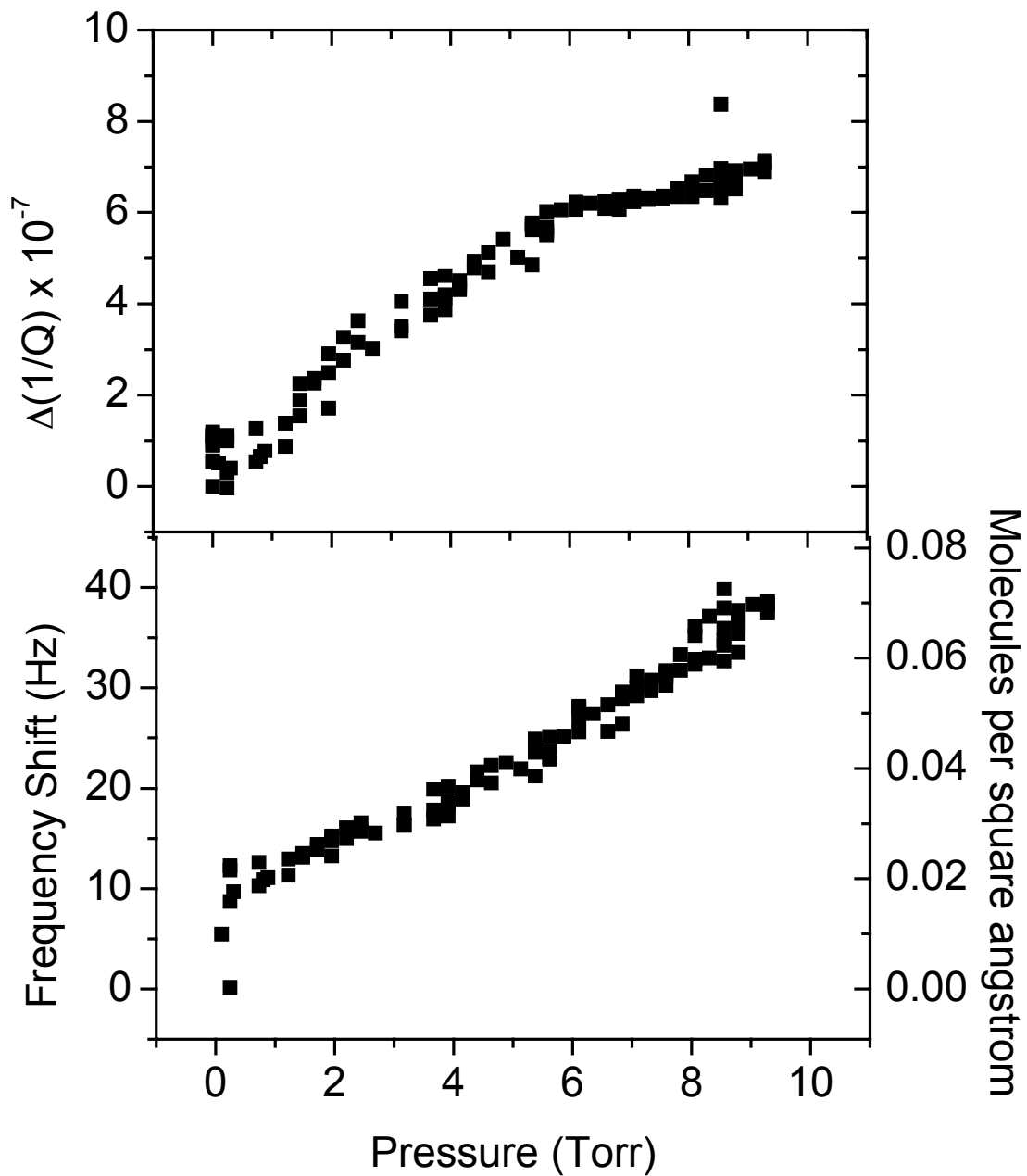


Figure A.6. N-octane/Pb(111), 052802b.dat. Data shown in average n-octane mass uptake and slip time, Chapter 6. Nitrogen calibration constant = 0.468; calibration file 052902a.dat.

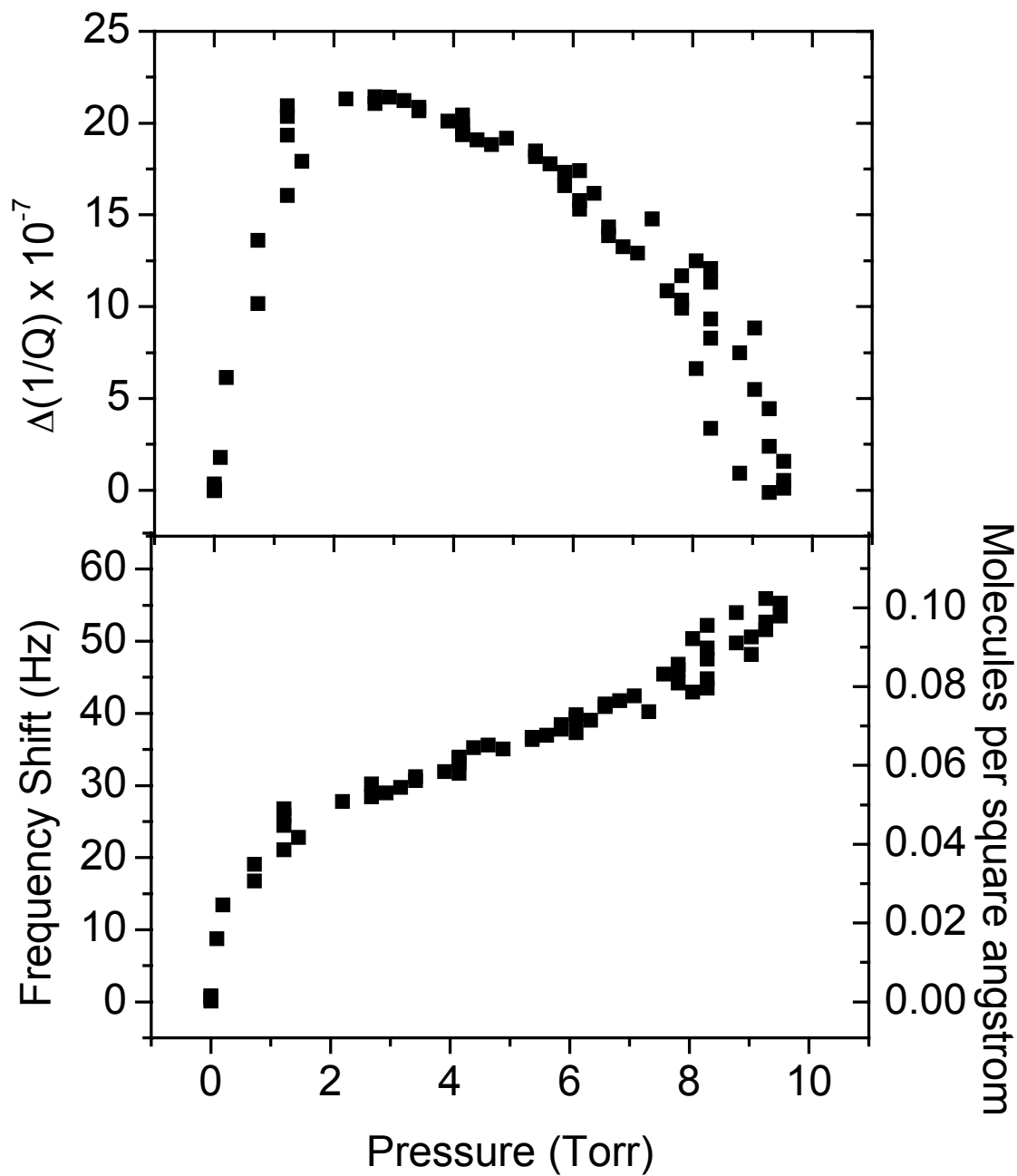


Figure A.7. N-octane/1.5 monolayers $C_{60}/Pb(111)/Cu(111)$, 050802c.dat. Supplementary data for sample A, not discussed, in Chapter 6. Nitrogen calibration constant = 0.298; calibration file 050702a.dat.

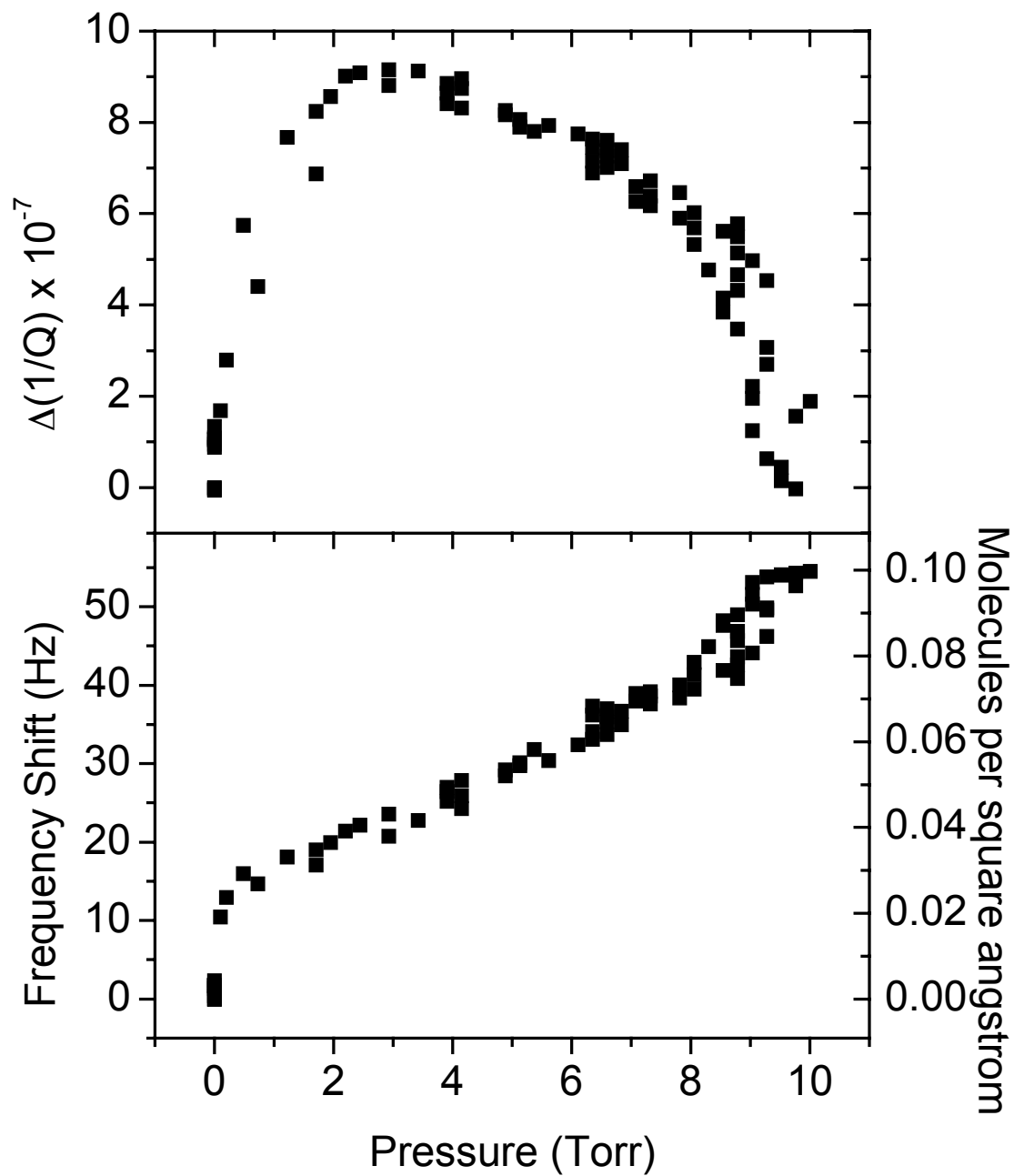


Figure A.8. N-octane/bilayer $C_{60}/Pb(111)/Cu(111)$, 051002b.dat. Supplementary data for sample A, not discussed, in Chapter 6. Nitrogen calibration constant = 0.478; calibration file 051002e.dat.

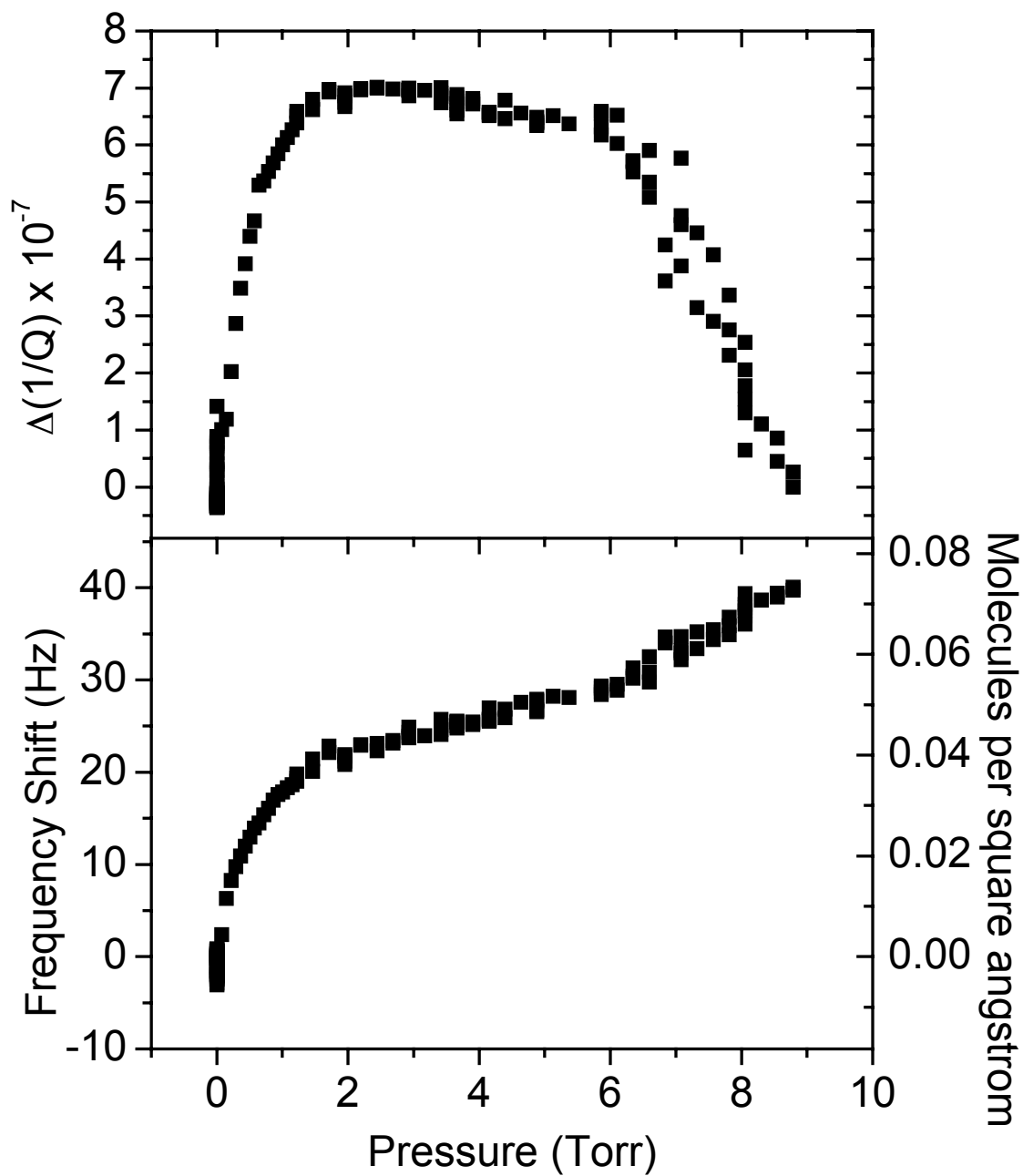


Figure A.9. N-octane/8 layers C_{60} /Pb(111)/Cu(111), 053002a.dat. Supplementary data for sample B, not discussed, in Chapter 6. Nitrogen calibration constant = 0.441; calibration file 053102a.dat.

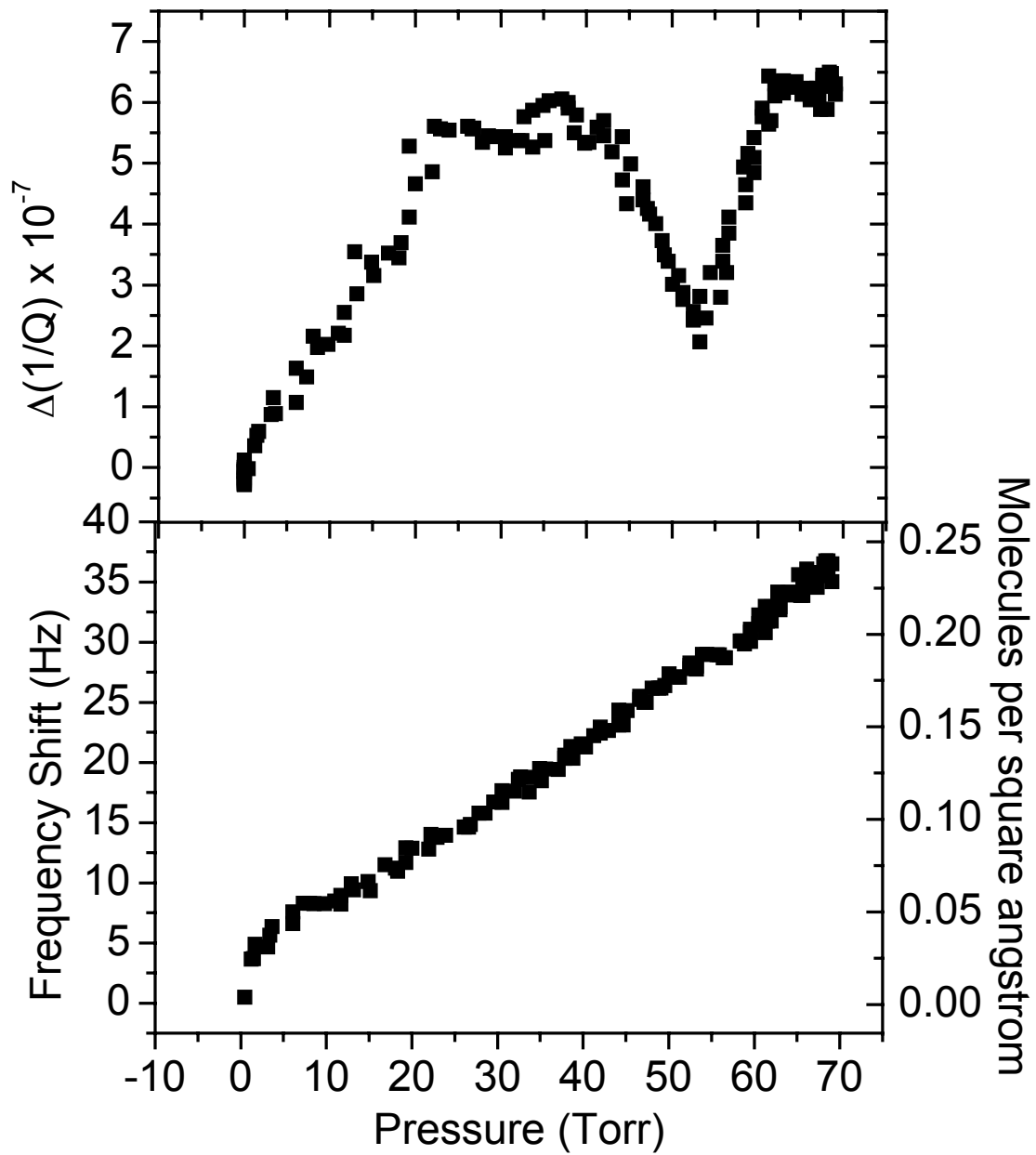


Figure A.10. Methanol/monolayer $C_{60}/Ag(111)$, 061903c.dat. Contained in box averaged frequency shift in Chapter 7. Hecal constant = 0.68; calibration file 062003a.dat.

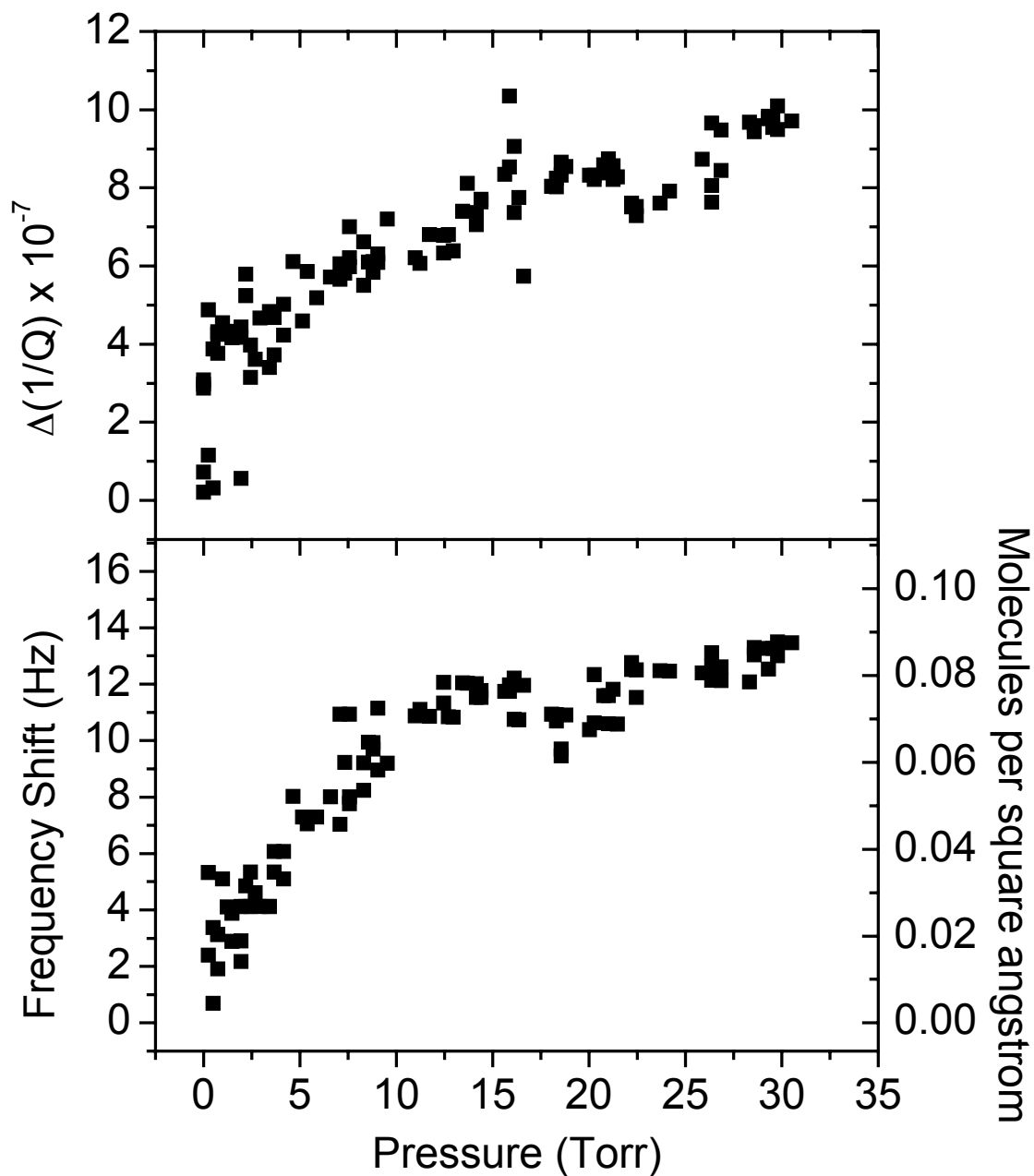


Figure A.11. Methanol/monolayer $C_{60}/Ag(111)$, 071603d.dat. Contained in box averaged slip time in Chapter 7. Hecal constant = 1.06 for $1/A = 11.5-12.1 \text{ V}^{-1}$ and 0.59 for $1/A = 12.3-13.0 \text{ V}^{-1}$; calibration file 071603f.dat.

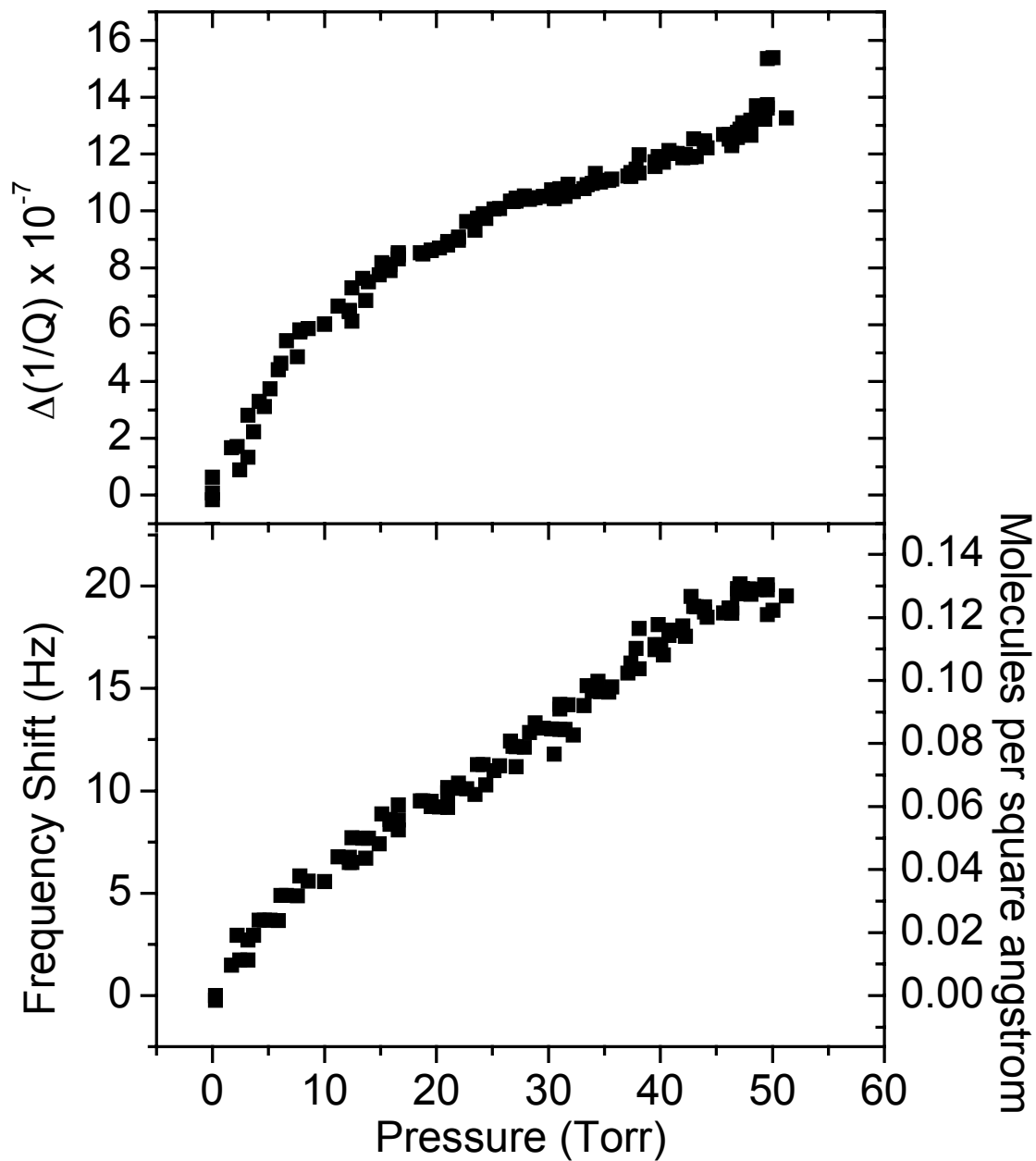


Figure A.12. Methanol/monolayer $C_{60}/Cu(111)$, 082803c.dat. Contained in box averaged slip time and box averaged frequency shift in Chapter 7. Hecal constant = 0.93 for $1/A = 18-18.6 \text{ V}^{-1}$ and 0.48 for $1/A = 18.6-20 \text{ V}^{-1}$; calibration file 082803e.dat.

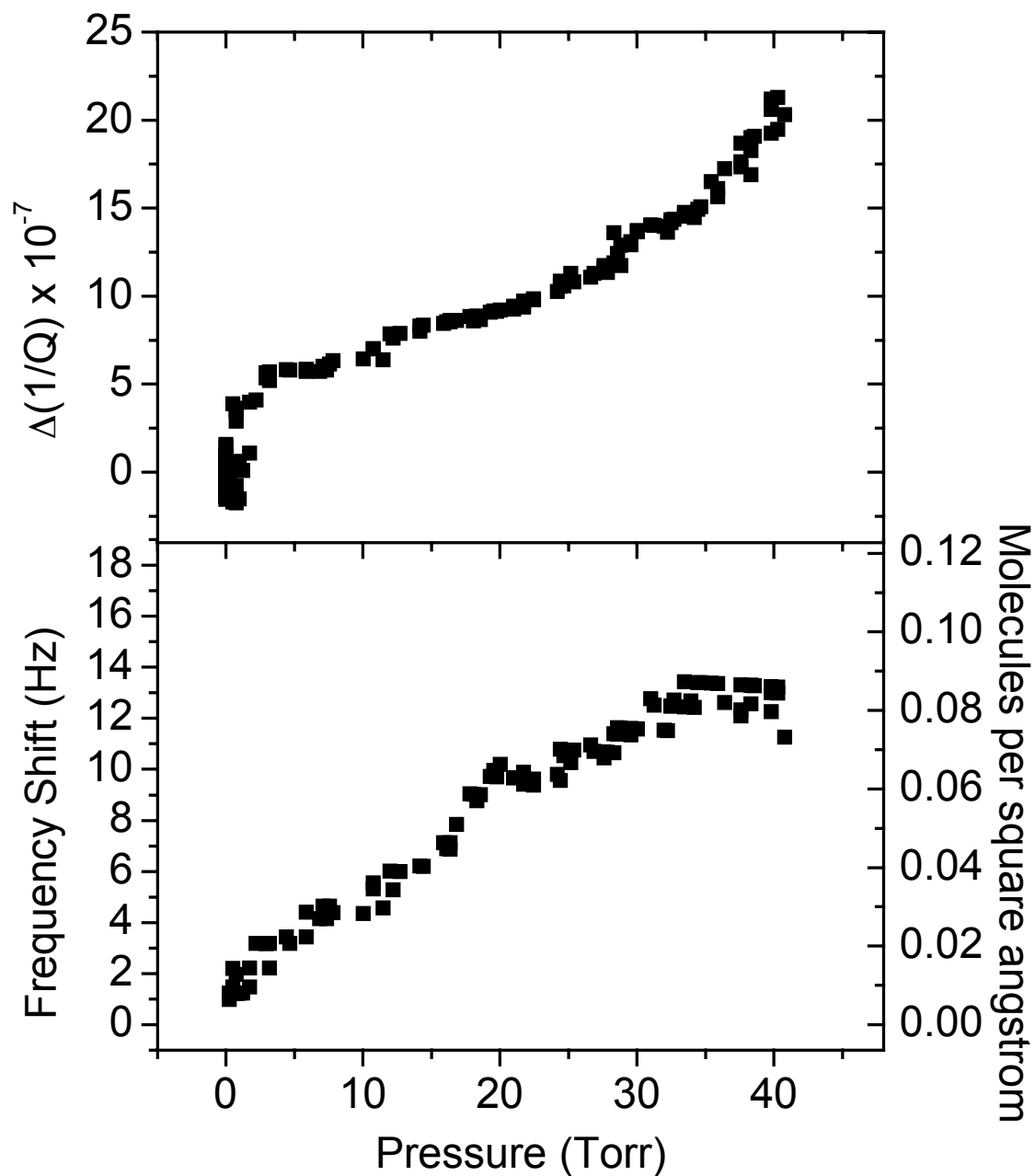


Figure A.13. Methanol/monolayer $C_{60}/Cu(111)$, 101603a.dat. Contained in box averaged slip time and box averaged frequency shift in Chapter 7. Hecal constant = 1.72 for $1/A = 15.9-16.5 \text{ V}^{-1}$ and 0.54 for $1/A = 16.5-18 \text{ V}^{-1}$; calibration file 101603c.dat.

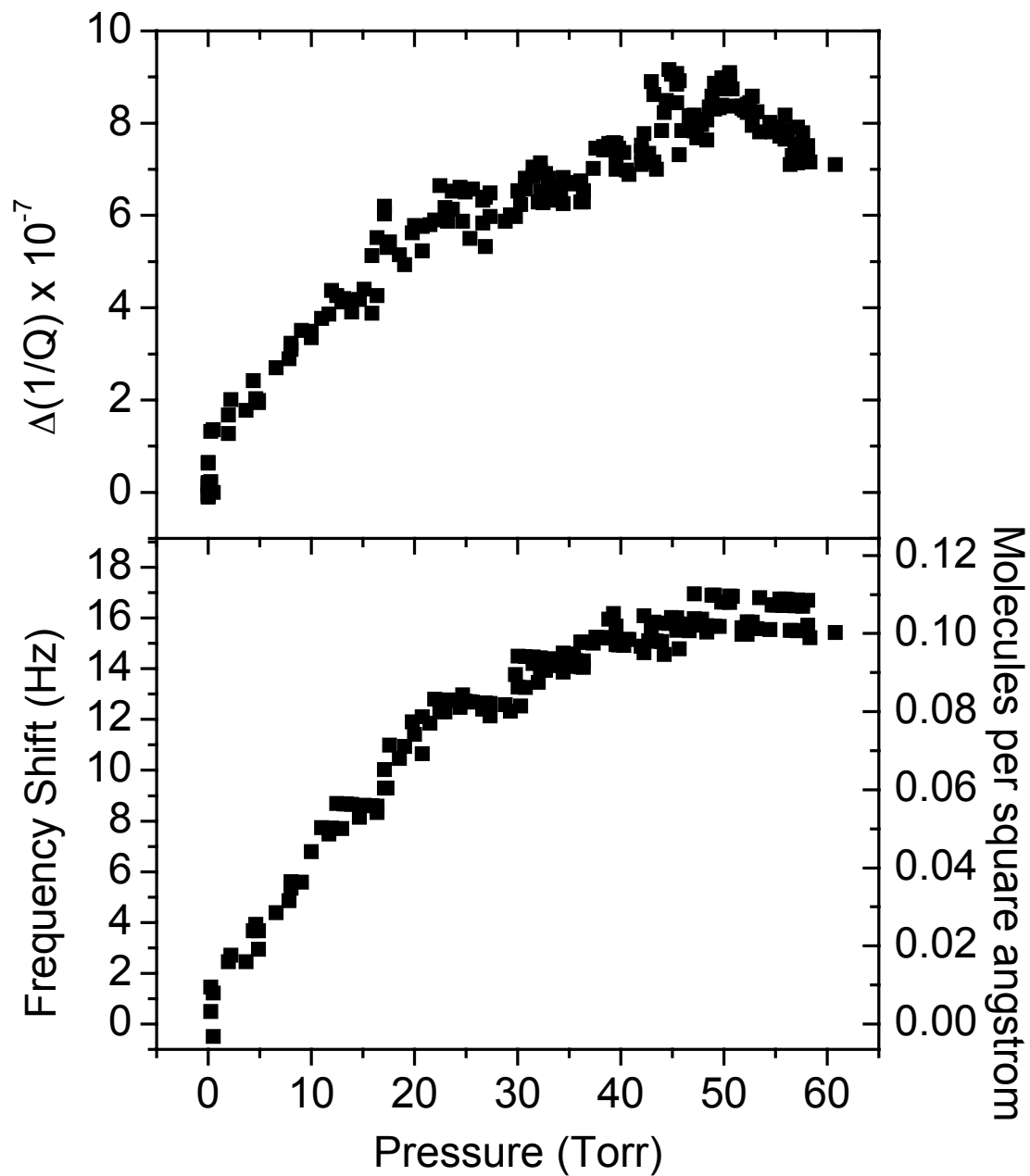


Figure A.14. Methanol/monolayer $C_{60}/Ag(111)$, 121203a.dat. Contained in box averaged frequency shift in Chapter 7. Hecal constant = 1.224; calibration file 121203b.dat.

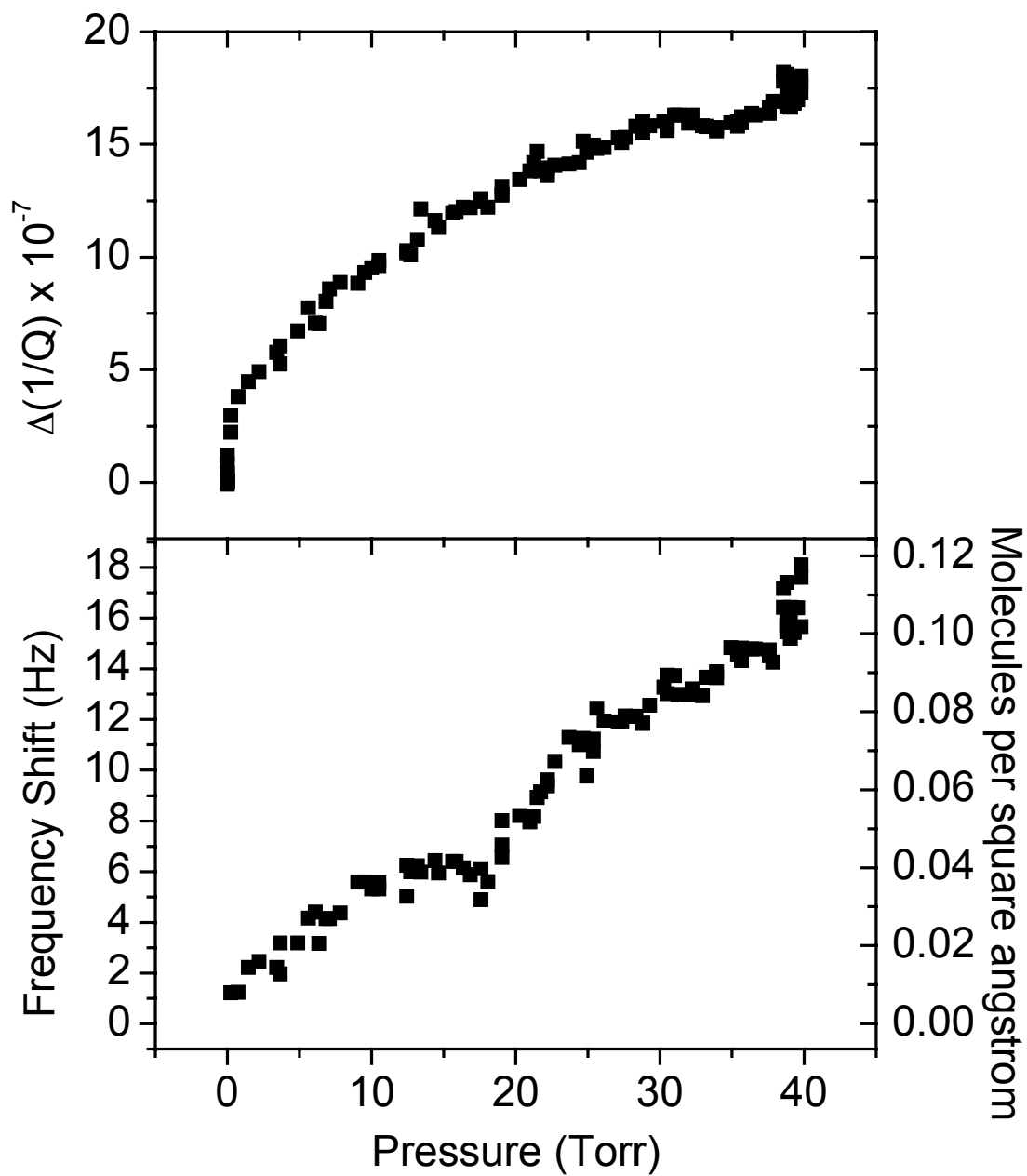


Figure A.15. Methanol/monolayer $C_{60}/Cu(111)$, 040804a.dat. Contained in box averaged slip time in Chapter 7. Hecal constant = 0.712; calibration file 040804b.dat.

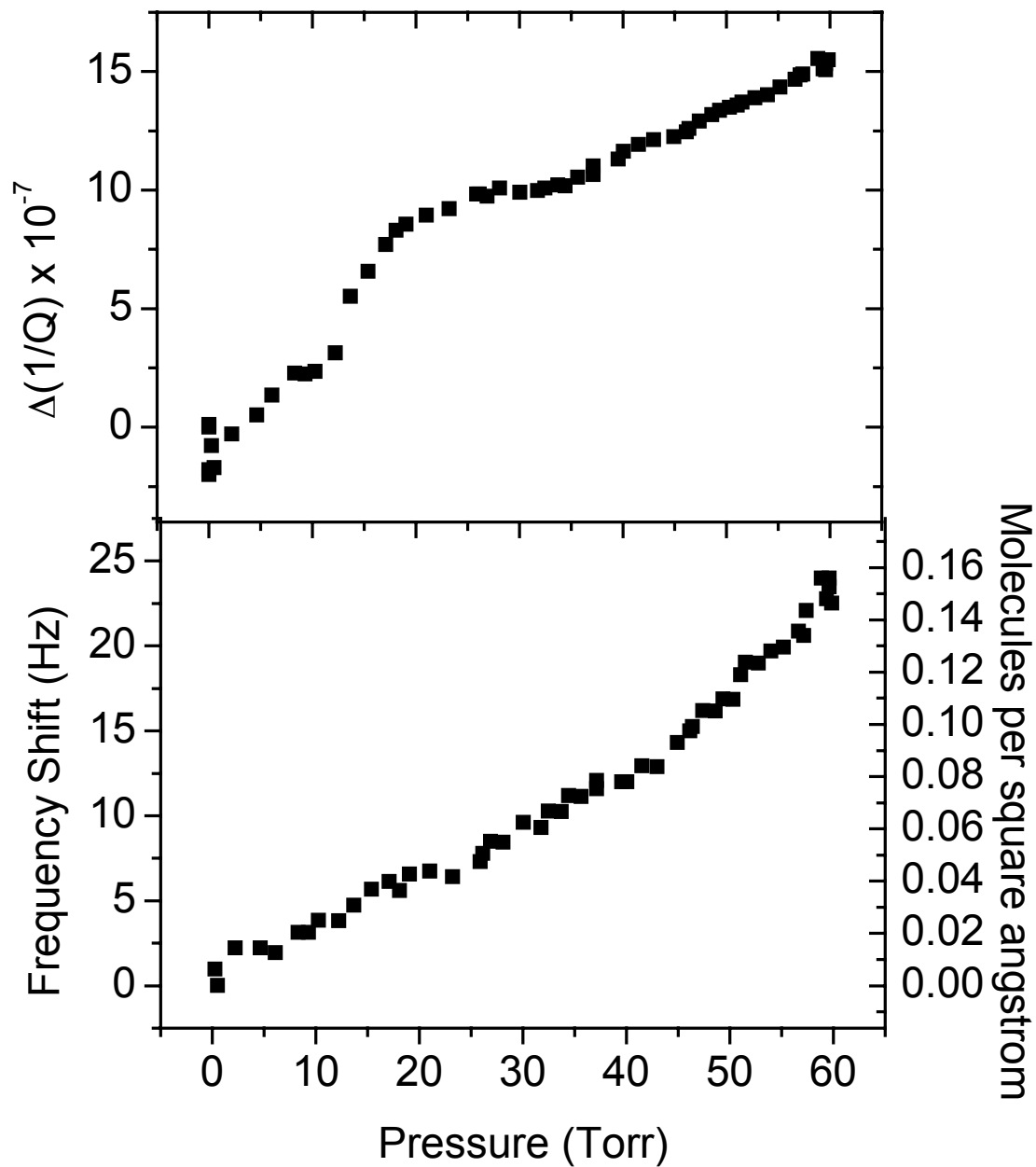


Figure A.16. Methanol/bilayer $C_{60}/Ag(111)$, 070103a.dat. Contained in box averaged slip time and box averaged frequency shift in Chapter 7. Hecal constant = 1.26 for $1/A = 11.8-12.4 \text{ V}^{-1}$ and 0.55 for $1/A = 12.4-13.1 \text{ V}^{-1}$; calibration file 070103c.dat.

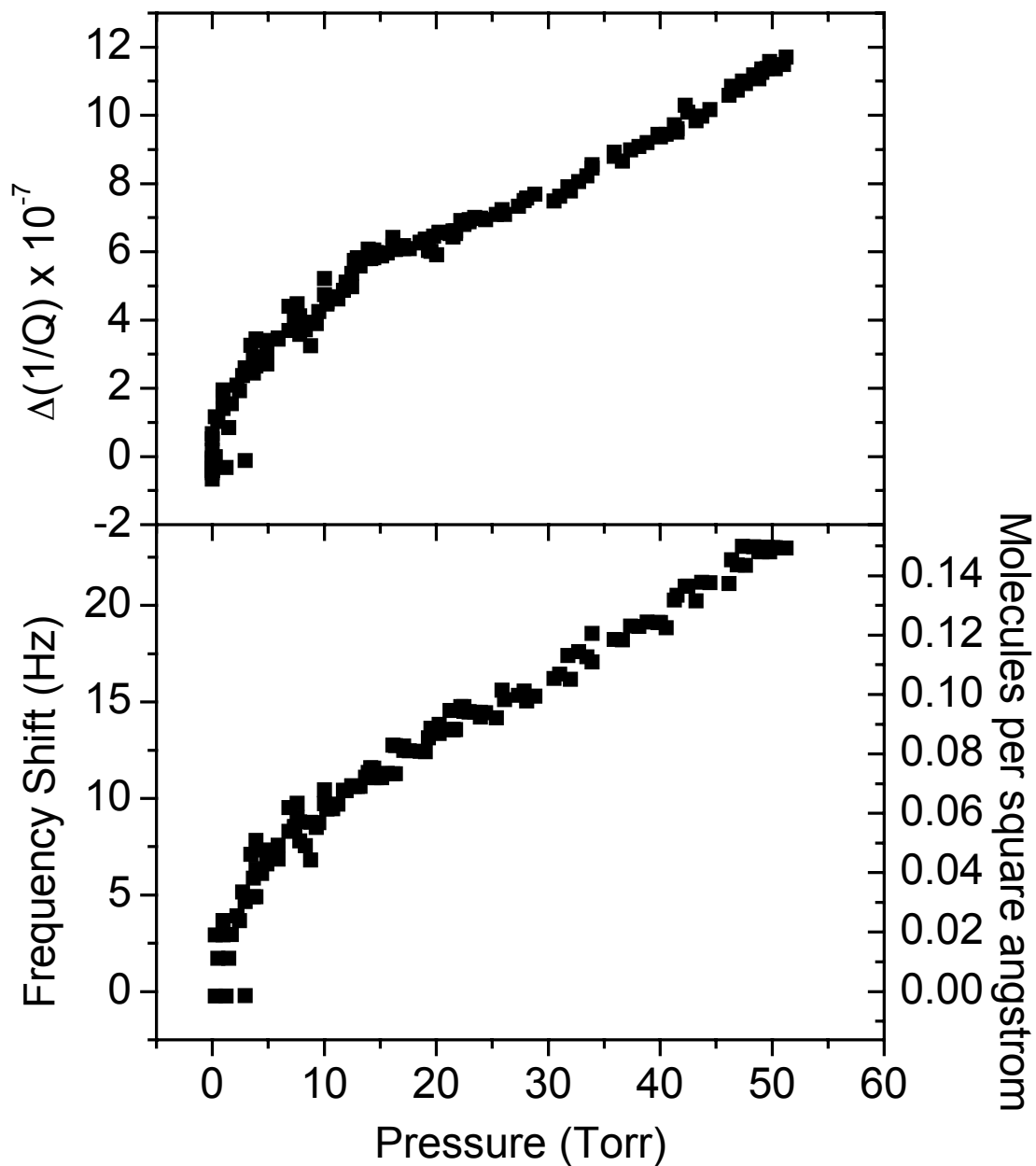


Figure A.17. Methanol/bilayer $C_{60}/Ag(111)$, 071703c.dat. Contained in box averaged slip time and box averaged frequency shift in Chapter 7. Hecal constant = 0.85 for $1/A = 13.5-14.1 \text{ V}^{-1}$ and 0.64 for $1/A = 14.1-14.8 \text{ V}^{-1}$ calibration file 071703d.dat.

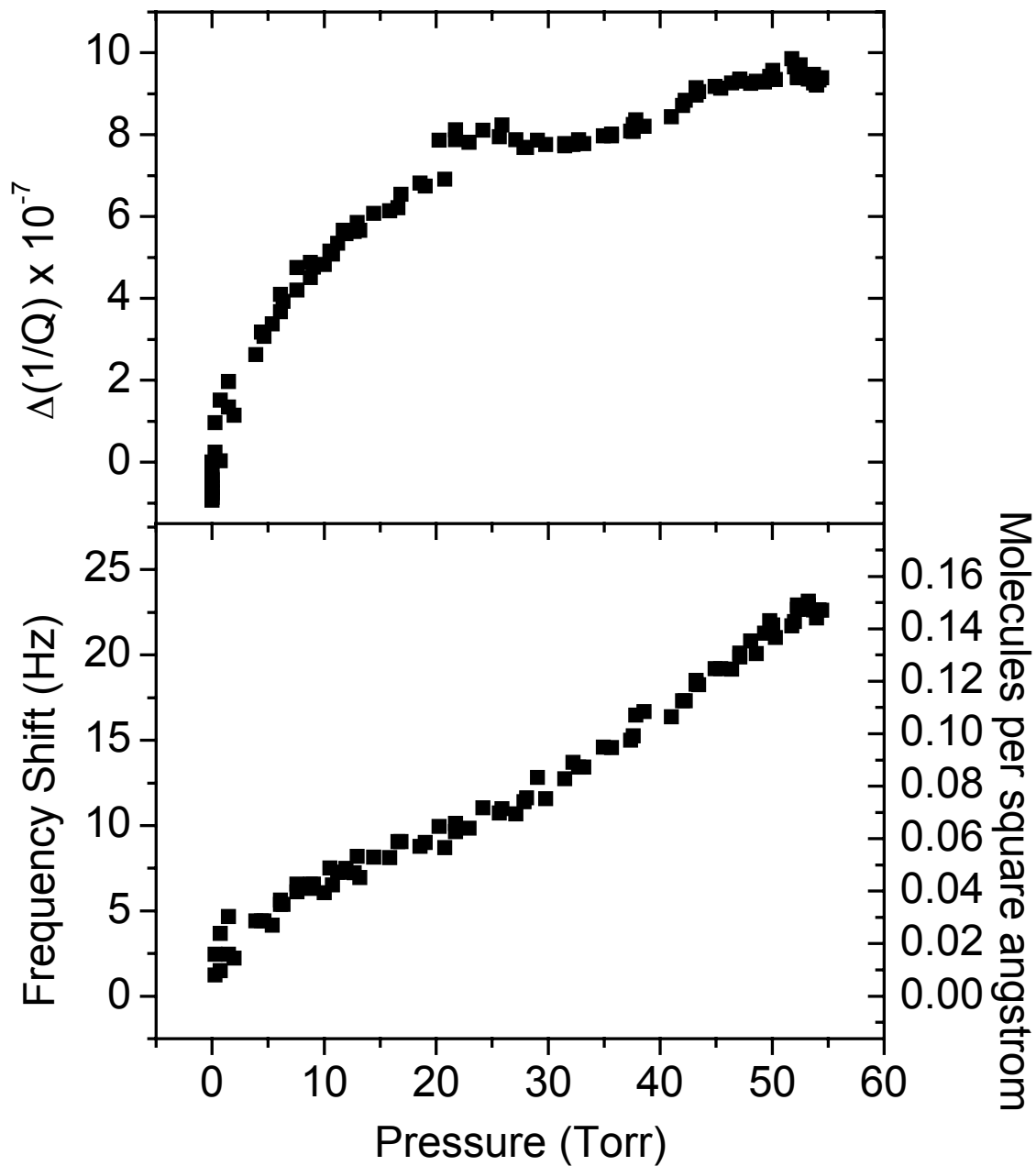


Figure A.18. Methanol/bilayer $C_{60}/Cu(111)$, 082903c.dat. Contained in box averaged slip time and box averaged frequency shift in Chapter 7. Hecal constant = 0.71 for $1/A = 18.9-20.25 \text{ V}^{-1}$ and 0.47 for $1/A = 20.25-21.2 \text{ V}^{-1}$; calibration file 082903e.dat.

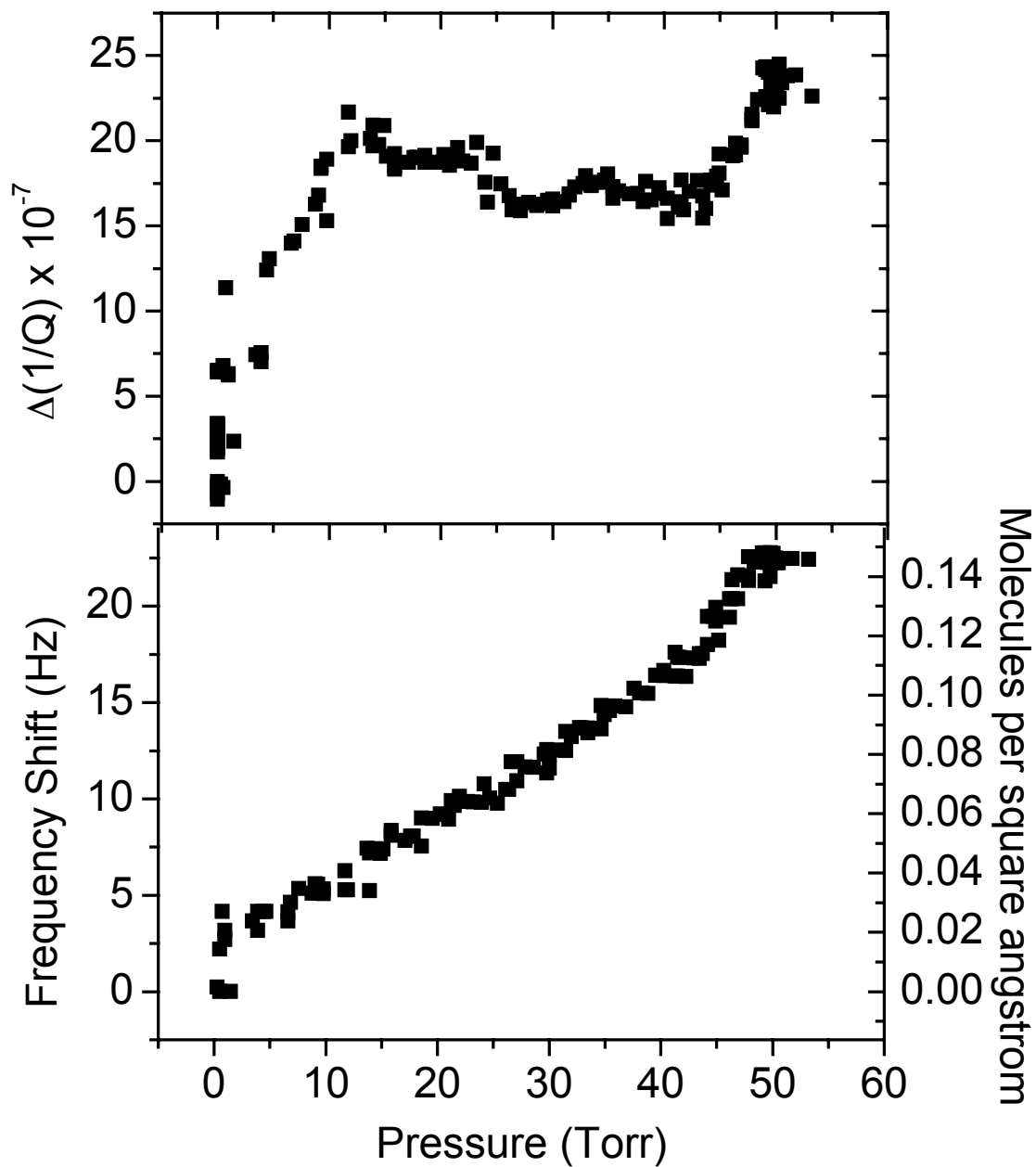


Figure A.19. Methanol/bilayer $C_{60}/Cu(111)$, 102203a.dat. Contained in box averaged frequency shift in Chapter 7. Hecal constant = 1.13; calibration file 102203c.dat.

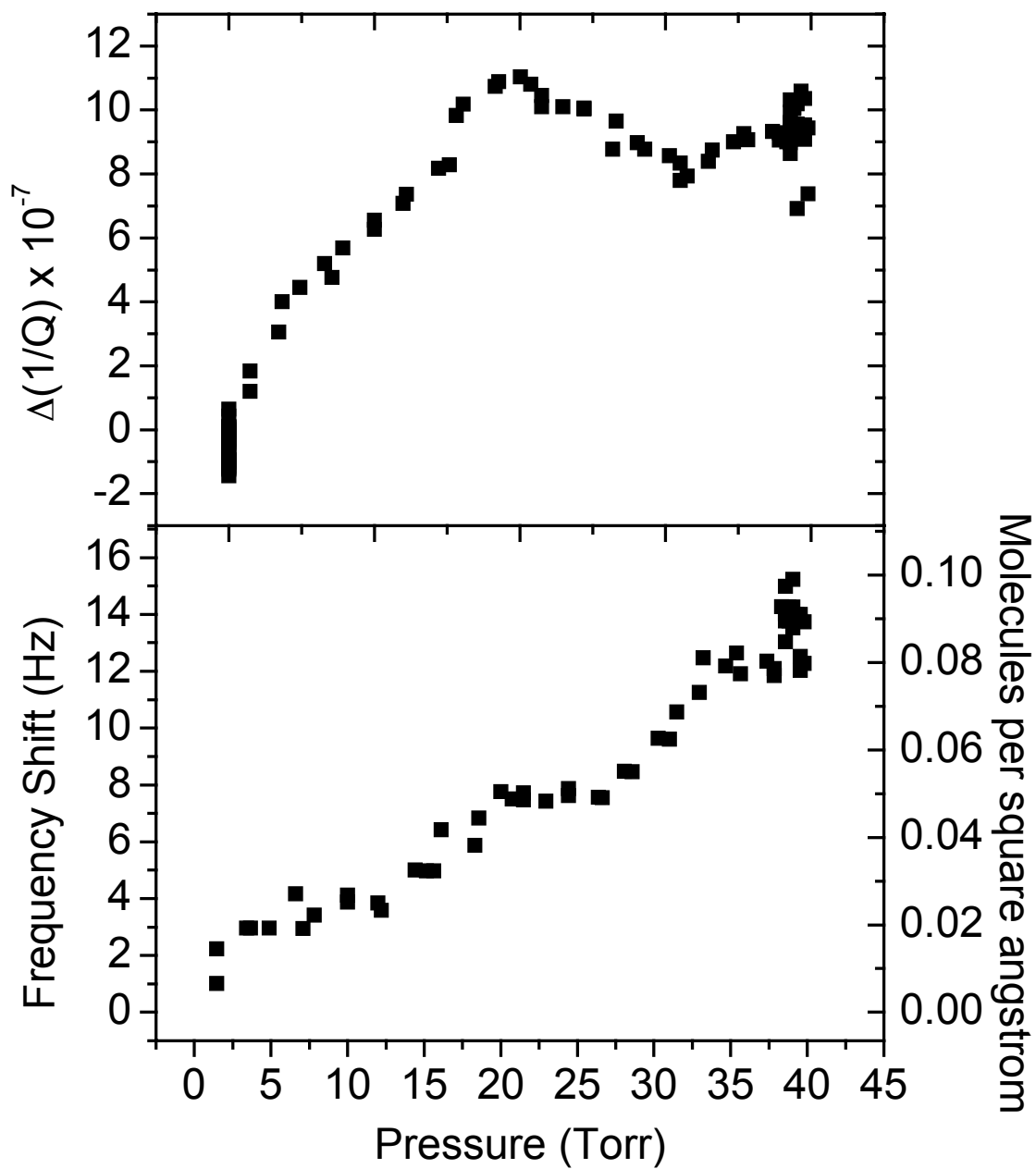


Figure A.20. Methanol/bilayer $C_{60}/Cu(111)$, 041304a.dat. Contained in box averaged slip time in Chapter 7. Hecal constant = 0.881; calibration file 041304c.dat.

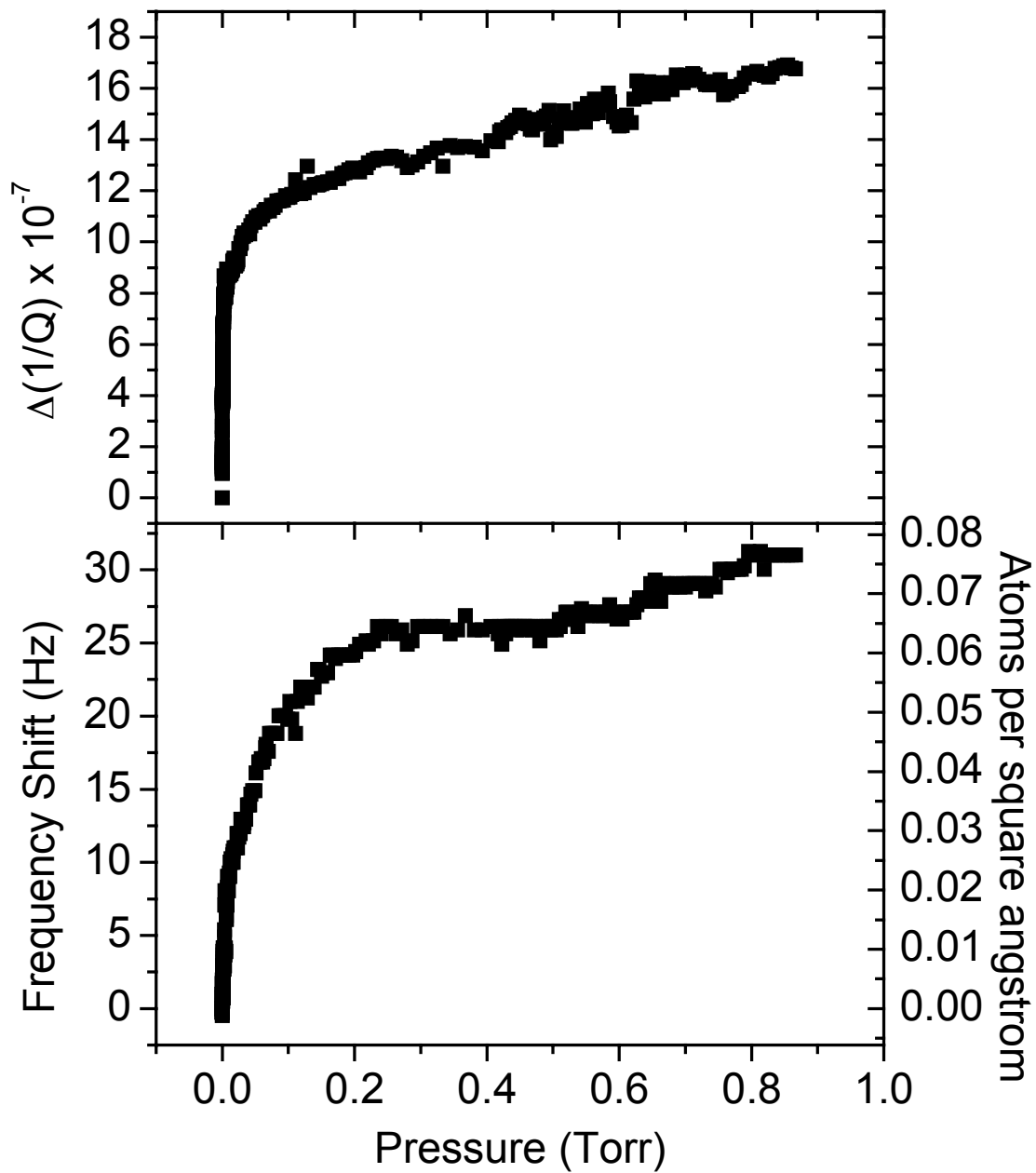


Figure A.21. Krypton/monolayer $C_{60}/Ag(111)$, 020604a.dat. Contained in box averaged slip time in Chapter 7. Hecal constant = 0.217; calibration file 020604b.dat.

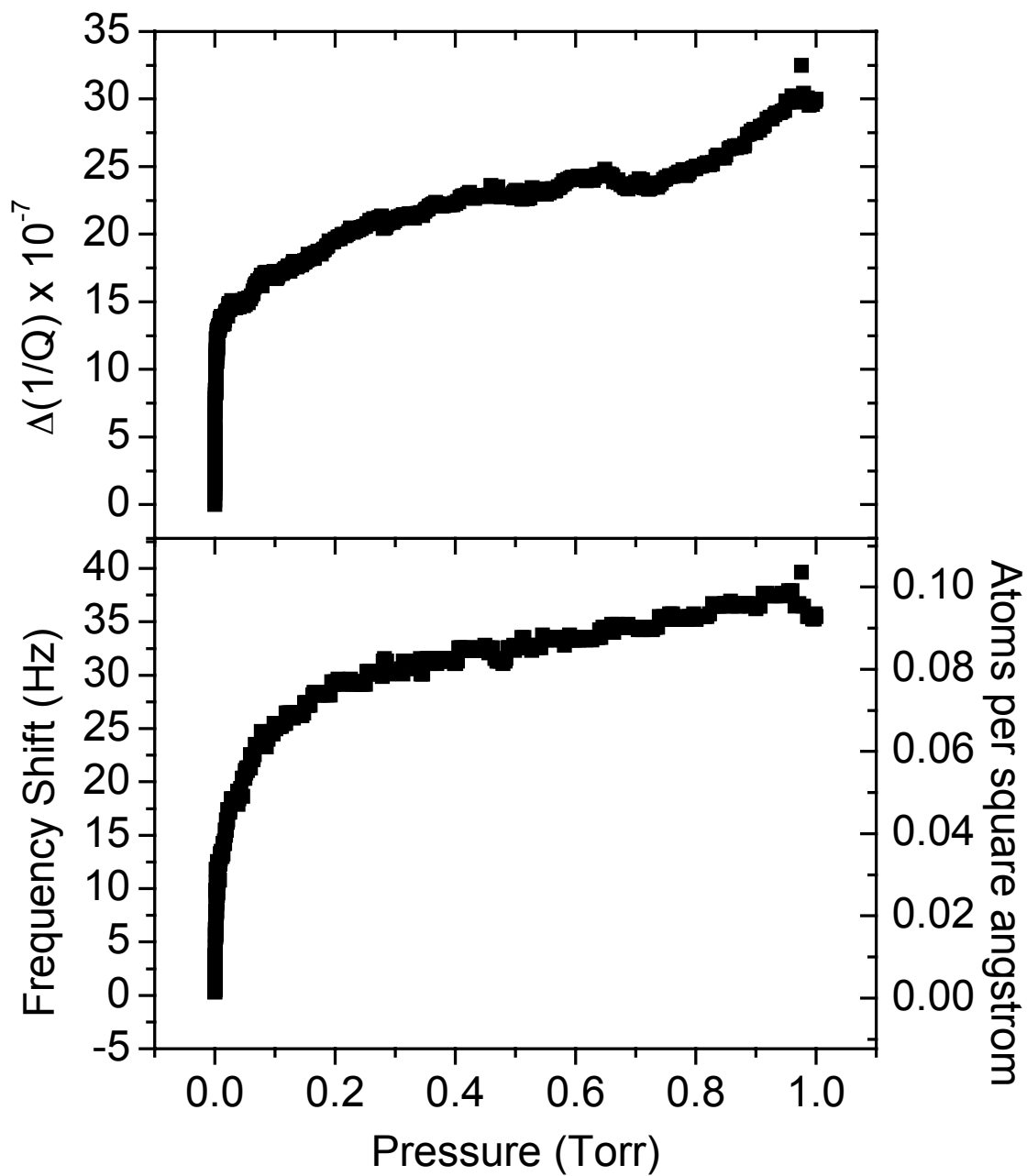


Figure A.22. Krypton/bilayer $C_{60}/Ag(111)$, 021104a.dat. Contained in box averaged slip time in Chapter 7. Hecal constant = 0.434; calibration file 021104b.dat.

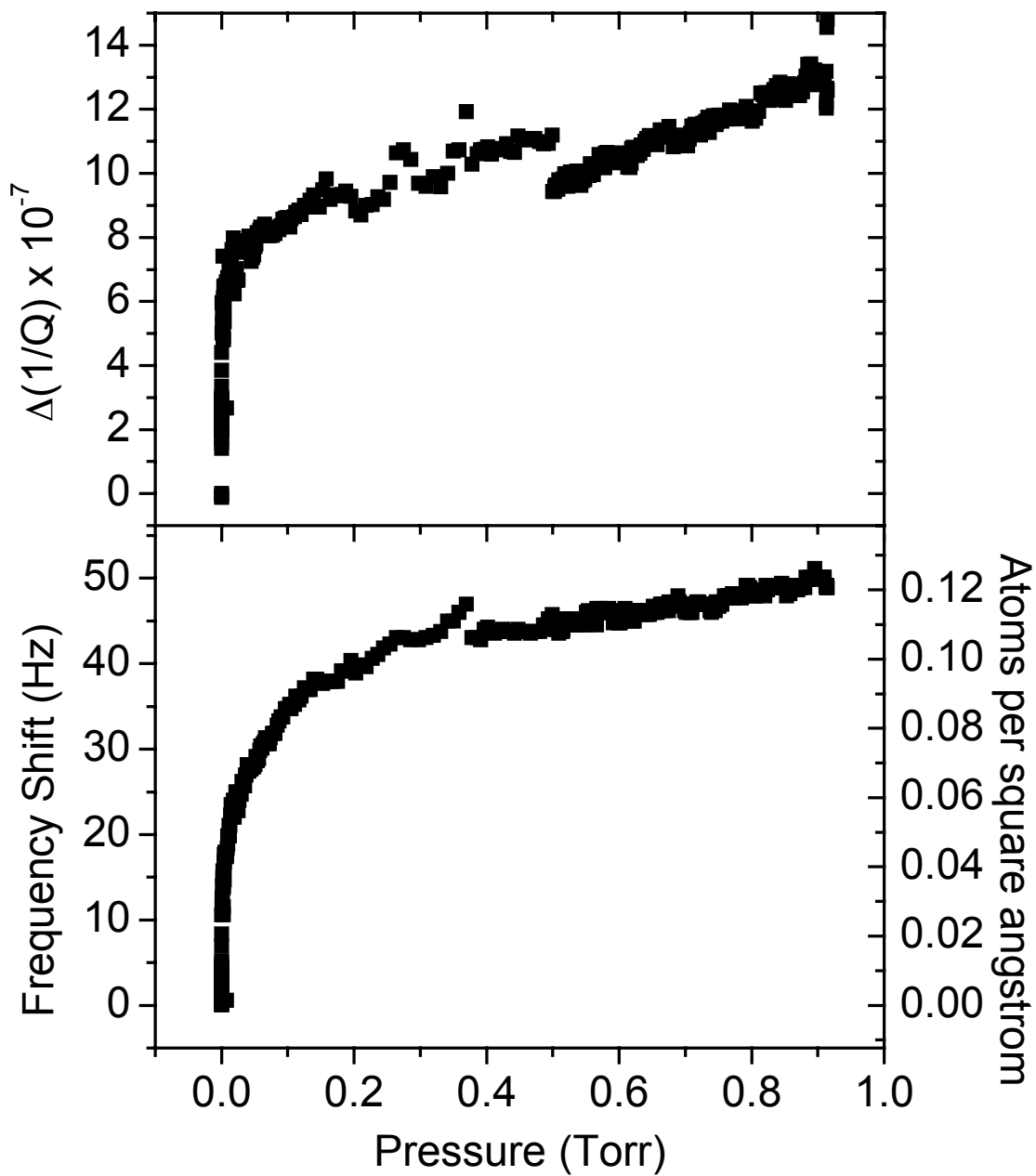


Figure A.23. Krypton/monolayer C₆₀/Cu(111), 040604a.dat. Contained in box averaged slip time in Chapter 7. Hecal constant = 0.611; calibration file 040604b.dat.

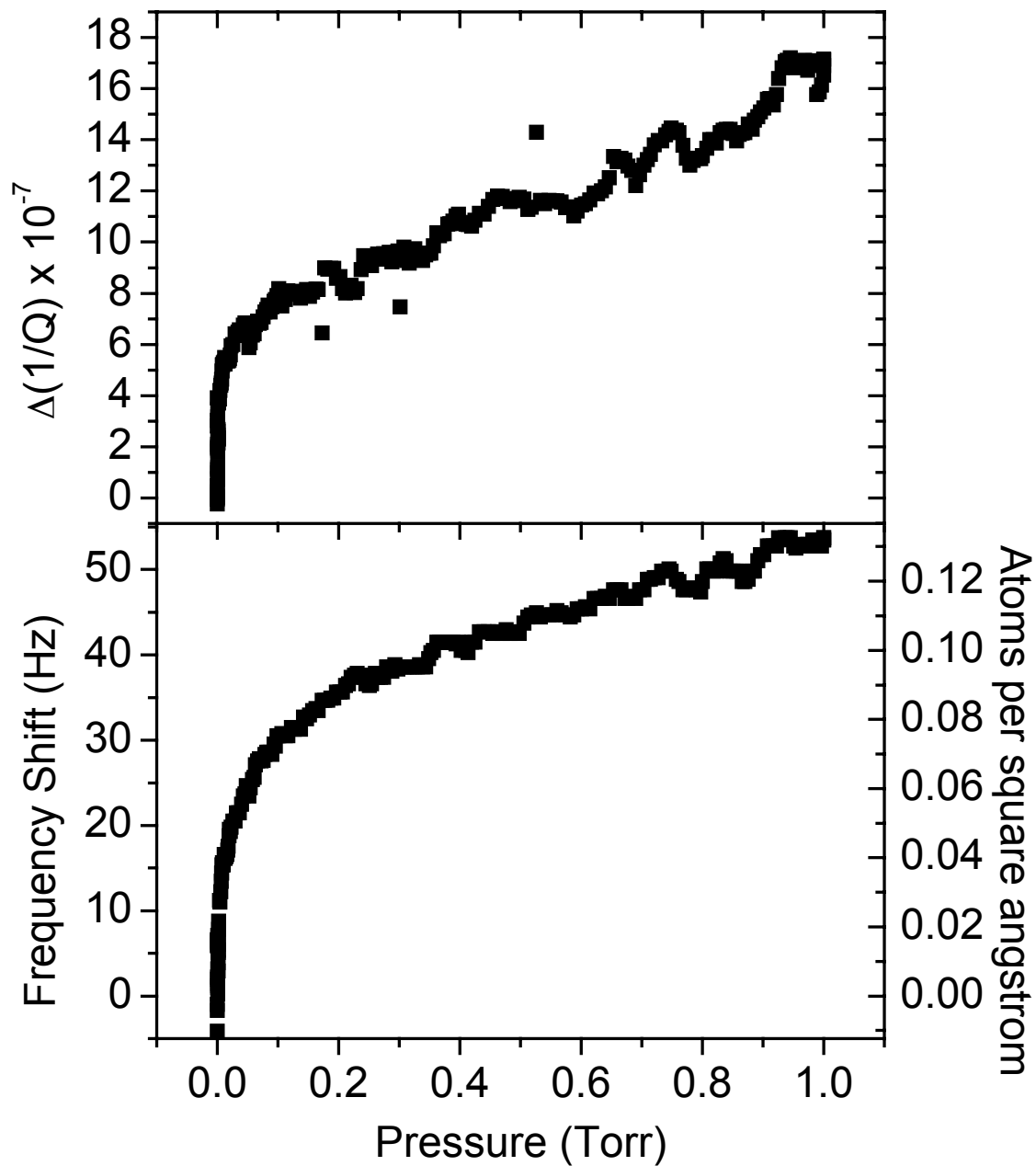


Figure A.24. Krypton/bilayer $C_{60}/Cu(111)$, 041204a.dat. Contained in box averaged slip time in Chapter 7. Hecal constant = 0.384; calibration file 041204b.dat.

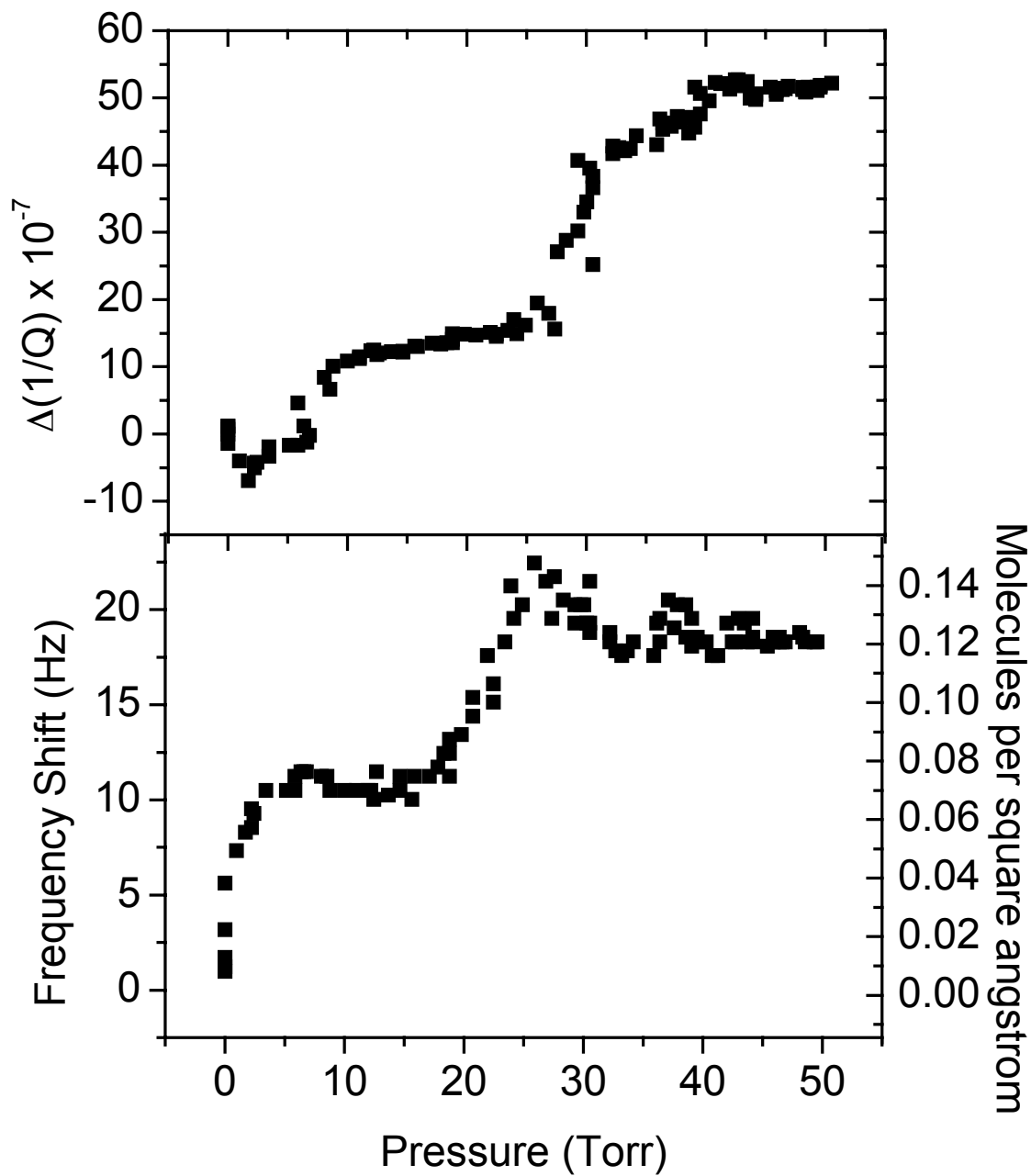


Figure A.25. Methanol/Cu(111), 101103a.dat. Supplementary data set, not discussed. Shows steps in methanol isotherm, indicating layer formation. Hecal constant = 1.5 for $1/\text{A} = 19.7\text{-}20 \text{ V}^{-1}$ and 0.49 for $1/\text{A} = 20\text{-}22 \text{ V}^{-1}$; calibration file 101103b.dat.

Table A.1. Chapter 4 helium calibration information.

Surface	Filename	Helium Calibration Information	Helium Calibration Filename
Xe/Cu(111)	100703a.dat	Hecal = 0.822	100703b.dat
Xe/Ni(111)	012701b.prn	Hecal = 0.606	012801a.prn
Xe/Graphene	022001a.prn	Hecal = 0.3	Ring-down method
Xe/C ₆₀ /Ag(111)	021304a.dat	Hecal = 0.391	021304b.dat

Chapter 1 References

- 1.1 G. Amontons, Mem. Acad. Roy. Sci. 206 (1699)
- 1.2 Coulomb, Charles A. Theorie des machines simples (1781).
- 1.3 Da Vinci, Leonardo, *Codex Atlanticus* c. 1500.; Da Vinci, Leonardo, *Codex Arundel*, c. 1500.
- 1.4 F. Palmer, Scientific American 184, 55 (February, 1951).
- 1.5 F.P.D. Bowden and D. Tabor, *Friction and Lubrication of Solids, Part I*, Oxford University Press, Oxford (1954)
- 1.6 B. Bhushan, J.N. Israelachvili, and U. Landman, Nature 374, 607 (1995).
- 1.7 J.N. Israelachvili and D. Tabor, Proc. R. Soc. Lond. A 331, 19 (1972)
- 1.8 J.N. Israelachvili and D. Tabor, Prog. Surf. Membr. Sci. 7, 1 (1973)
- 1.9 G.A. Tomlinson, Phil. Mag. 7, 905 (1929)
- 1.10 J.E. Sacco and J.B. Sokoloff, Phys. Rev. B 18, 6549 (1978)
- 1.11 J.B. Sokoloff, J.E.Sacco, and J.F. Weisz, Phys. Rev. Lett. 41, 1561 (1978)
- 1.12 C.M. Mate, G.M. McClelland, R. Erlandsson and S. Chang, Phys. Rev. Lett. 59, 1942 (1987)
- 1.13 J. Krim and A. Widom, Phys. Rev. B 38, 12184 (1986)
- 1.14 A. Widom and J. Krim, Phys. Rev. B 34, R3 (1986)
- 1.15 E.T. Watts, J. Krim, and A. Widom, Phys. Rev. B 41, 3466 (1990)
- 1.16 M.O. Robbins and J. Krim, MRS Bulletin 23, 23 (1998)
- 1.17 J. Krim, D.H. Solina, and R. Chiarello, Phys. Rev. Lett. 66, 181 (1991)
- 1.18 M. Cieplak, E.D. Smith, and M.O. Robbins, Science 265, 1209 (1994)
- 1.19 W. Steele, Surface Science 36, 317 (1973).

- 1.20 C. Daly and J. Krim, Phys. Rev. Lett. 76, 803 (1996)
- 1.21 B.N.J. Persson and A. Nitzan, Surf. Sci. 367, 261-275, (1996).
- 1.22 J. Braun, D. Fuhrmann, A. Siber, B. Gumhalter, and Ch. Woll, Phys. Rev. Lett. 80, 125 (1997).
- 1.23 M.S. Tomassone, J.B. Sokoloff, and J. Krim, Phys. Rev. Lett. 79, 4798 (1997)
- 1.24 B.N.J. Persson, Phys. Rev. B 44, 3277-3296 (1991)
- 1.25 D. Schumacher, *Surface Scattering Experiments with Conduction Electrons*, Springer, Berlin (1993) Sections 4.2-4.3.
- 1.26 A. Dayo and J. Krim, International J. of Thermophysics 19, 827 (1998)
- 1.27 A. Liebsch, S. Goncalves, and M. Kiwi, Phys. Rev. B 60, 5034 (1999).
- 1.28 M.O. Robbins and M.H. Muser, in Handbook of Modern Tribology, ed. B. Bhushan, CRC Press.

Chapter 2 References

- 2.1 J.P. Toennies, J. Phys. Condens. Matt. 5, A25 (1993)
- 2.2 Ch. Woll in *Physics of Sliding Friction* edited B.N.J. Persson and E. Tosatti, Kluwer Dordrecht (1996) p. 231
- 2.3 G. Witte, Surface Science 502-503, 405 (2002)
- 2.4 J. Braun, D. Fuhrmann, A. Siber, B. Gumhalter, and Ch. Woll, Phys. Rev. Lett. 80, 125 (1998).
- 2.5 L.W. Bruch and F.Y. Hansen, Phys. Rev. B 55, 1782 (1997)
- 2.6 L.W. Bruch, Phys. Rev. B 37, 6658 (1988).
- 2.7 B.N.J. Persson, *Sliding Friction: Physical Principles and Applications*, Springer, Berlin, 2000.

Chapter 3 References

- 3.1 C. Lu and A. Czanderna, eds. Applications of Piezoelectric Quartz Crystal Microbalances (Elsevier, Amsterdam, 1984).
- 3.2 W.G. Cady, Piezoelectricity, 2nd ed. (Dover, N.Y., 1964).
- 3.3 D. Salt, Hy-Q Handbook of Quartz Crystal Devices Van Nostrand Reinhold (UK) Co. Ltd., T.J. Press (Padstow) Ltd., Cornwall.
- 3.4 J. Krim and A. Widom, Phys. Rev. B 38, 12184, 1988; A. Widom and J. Krim, Phys. Rev. B 34, R3, 1986.
- 3.5 Crystallographic quartz axes figure reference
- 3.6 G.Z. Sauerbrey, Phys. Verhandl., 8 113, 1957.
- 3.7 G.Z. Sauerbrey, Z. Phys., 115, 206, 1959.
- 3.8 Yaws, Carl L., Handbook of Viscosity, (Gulf Publishing Co., Houston, 1995).
- 3.9 CRC Handbook of Chemistry and Physics, (Knovel, Norwich, N.Y., 2000).
- 3.10 L.D. Landau and E.M. Lifshitz, Fluid Mechanics, Vol. 6 of Course of Theoretical Physics (Pergamon, London, 1959), pp. 88-90.
- 3.11 C.D. Stockbridge, Vacuum Microbalance Techniques Vol. 5 (Plenum Press, New York, 1966).
- 3.12 H. Helmholtz and Piotrowski, Sitzungsber. Der K. Akad. In Wien, 40, 1860.
- 3.13 L. Bruschi and G. Mistura, Phys. Rev. B 63, 235411 (2001).
- 3.14 C.D. Stockbridge and A.W. Warner, Vacuum Microbalance Techniques, Vol. 2 (Plenum Press, New York, 1962).
- 3.15 E.P. EerNisse, Applications of Piezoelectric Quartz Crystal Microbalances edited by C. Lu and A.W. Czanderna (Elsevier, Amsterdam 1984).

- 3.16 S.M. Winder, Doctoral Dissertation, North Carolina State University, 2003.
- 3.17 H. Krim, thesis, University of Washington, 1980.

Chapter 4 References

- 4.1 J. Krim, D.H. Solina, and R. Chiarello, *Phys. Rev. Lett.* 66, 181 (1991).
- 4.2 C. Daly and J. Krim, *Phys. Rev. Lett.* 76, 803 (1996).
- 4.3 M. Cieplak, E.D. Smith, and M.O. Robbins, *Science* 265, 1209 (1994).
- 4.4 B.N.J. Persson and A. Nitzan, *Surf. Sci.* 367, 261 (1996).
- 4.5 M.S. Tomassone, J.B. Sokoloff, and J. Krim, *Phys. Rev. Lett.* 79, 4798 (1997).
- 4.6 A. Liebsch, S. Goncalves, and M. Kiwi, *Phys. Rev. B* 60, 5034 (1999).
- 4.7 M.O. Robbins and M.H. Muser, in *Handbook of Modern Tribology*, ed. B. Bhushan, CRC Press.
- 4.8 L.W. Bruch, *Phys. Rev. B* 37, 6658 (1988).
- 4.9 J. Braun, D. Fuhrmann, A. Siber, B. Gumhalter, and Ch. Woll, *Phys. Rev. Lett.* 80, 125 (1998).
- 4.10 R. Kariotis, J.A. Venables, M. Hamichi, and A.Q.D. Faisal, *J. Phys. C: Solid State Phys.* 19, 5717 (1987).
- 4.11 E. Nabighian and X.D. Zhu, *Chem. Phys. Lett.* 316, 177 (2000).
- 4.12 M.A. Chesters, M. Hussain, and J. Pritchard, *Surf. Sci.* 35, 161 (1973).
- 4.13 D. Fargues, P. Dolle, M. Alnot, and J.J. Ehrhardt, *Surf. Sci.* 214, 187 (1989).
- 4.14 L.W. Bruch, Private Conversation.
- 4.15 L.W. Bruch, "From Adsorbate Spectroscopy to Atomic Friction"
- 4.16 J. Nakamura, H. Hirano, M. Xie, I. Matsuo, T. Yamada, and K. Tanaka, *Surface Science* 222, L809 (1989).
- 4.17 S.M. Lee and J. Krim, in progress.
- 4.18 K.K. Kakati and H. Wilman, *J. Phys. D: Appl. Phys.* 6, 1307 (1973).

- 4.19 Research grade xenon (99.999% pure) was purchased from Airco Industrial Gases.
- 4.20 G.Z. Sauerbrey, *Phys. Verhandl.*, 8 113, 1957.
- 4.21 M. Chester, L.C. Yang, and J.G. Stephens, *Phys. Rev. Lett.* 29, 211 (1979).
- 4.22 E.T. Watts, J. Krim, and A. Widom, *Phys. Rev. B* 41, 3466 (1990).
- 4.23 J. Krim and A. Widom, *Phys. Rev. B* 38, 12184 (1986); A. Widom and J. Krim, *Phys. Rev. B* 34, R3 (1986); L. Bruschi and G. Mistura, *Phys. Rev. B* 63, 235411 (2001).
- 4.24 J. Krim, J.G. Dash, and J. Suzanne, *Phys. Rev. Lett.* 52, 640 (1984); G. Palasantzas and J. Krim, *Phys. Rev. Lett.* 73, 3564 (1994).
- 4.25 A. Dayo and J. Krim, *International J. of Thermophysics* 19, 827 (1998).
- 4.26 P.M. McGuiggan and J.N. Israelachvili, *J. Mater. Res.* 5, 2332 (1990); M. Hirano, K. Shinjo, R. Kaneko, and Y. Murata, *Phys. Rev. Lett.* 67, 2642 (1991); M. Hirano, K. Shinjo, R. Kaneko, and Y. Murata, *Phys. Rev. Lett.* 78, 1448 (1997)

Chapter 5 References

- 5.1 E. Watts, J. Krim, and A. Widom, *Phys. Rev. B* 41, 3466 (1990).
- 5.2 J. Krim and A. Widom, *Phys. Rev. B* 38, 12184 (1986); A. Widom and J. Krim, *Phys. Rev. B* 34, R3 (1986); L. Bruschi and G. Mistura, *Phys. Rev. B* 63, 235411 (2001).
- 5.3 J. Krim, D.H. Solina, and R. Chiarello, *Phys. Rev. Lett.* 66, 181 (1991), C. Mak and J. Krim, *Phys. Rev. B* 58, 5157 (1998).
- 5.4 J. Krim, J. Suzanne, and J.G. Dash, *Phys. Rev. Lett.* 52, 640 (1984).
- 5.5 A. Thomy and X. Duval, in *Adsorption at the Gas-Solid And Liquid-Solid Interface*, edited by J. Rouquerol and K.S.W. Sing (Elsevier, Amsterdam, 1982).
- 5.6 M. Cieplak, E.D. Smith, and M.O. Robbins, *Science* 265, 1209 (1994).
- 5.7 M.O. Robbins and M.H. Muser, in *Handbook of Modern Tribology*, edited by B. Bhushan (CRC Press).
- 5.8 S.M. Lee and J. Krim, in progress.
- 5.9 K.K. Kakati and H. Wilman, *J. Phys. D: Appl. Phys.* 6, 1307 (1973).
- 5.10 Research grade krypton (99.999% pure) was purchased from Airco Industrial Gases.
- 5.11 G.Z. Sauerbrey, *Phys. Verhandl.*, 8 113, 1957.
- 5.12 M. Chester, L.C. Yang, and J.G. Stephens, *Phys. Rev. Lett.* 29, 211 (1979).
- 5.13 G. Palasantzas and J. Krim, *Phys. Rev. Lett.* 73, 3564 (1994).
- 5.14 B.N.J. Persson, *Phys. Rev. B* 44, 3277-3296 (1991)

Chapter 6 References

- 6.1 B.N.J. Persson, *Sliding Friction: Physical Principles and Applications*, Springer, Berlin, 2000.
- 6.2 D. Fuhrmann and Ch. Woll, *Surf. Sci.* 368, 20 (1996).
- 6.3 J. Krim, D.H. Solina, and R. Chiarello, *Phys. Rev. Lett.* 66, 181 (1991); C. Mak and J. Krim, *Phys. Rev. B* 58, 5157 (1998); C. Daly and J. Krim, *Phys. Rev. Lett.* 76, 803 (1996).
- 6.4 M.O. Robbins and M.H. Muser, in *Handbook of Modern Tribology*, edited by B. Bhushan (CRC Press).
- 6.5 A. Liebsch, S. Goncalves, and M. Kiwi, *Phys. Rev. B* 60, 5034 (1999).
- 6.6 J.P. Toennies, *J. Phys. Condens. Matt.* 5, A25 (1993)
- 6.7 Ch. Woll in *Physics of Sliding Friction* edited B.N.J. Persson and E. Tosatti, Kluwer Dordrecht (1996) p. 231
- 6.8 G. Witte, *Surface Science* 502-503, 405 (2002)
- 6.9 J. Braun, D. Fuhrmann, A. Siber, B. Gumhalter, and Ch. Woll, *Phys. Rev. Lett.* 80, 125 (1998).
- 6.10 L.W. Bruch and F.Y. Hansen, *Phys. Rev. B* 55, 1782 (1997)
- 6.11 B.N.J. Persson, E. Tosatti, D. Fuhrmann, G. Witte, and Ch. Woll, *Phys. Rev. B* 59, 11777 (1999).
- 6.12 The GC grade n-octane (99.7% pure) was obtained from Alfa-Aesar.
- 6.13 G.Z. Sauerbrey, *Phys. Verhandl.*, 8 113, 1957.
- 6.14 E.T. Watts, J. Krim, and A. Widom, *Phys. Rev. B* 41, 3466 (1990).

- 6.15 J. Krim and A. Widom, Phys. Rev. B 38, 12184 (1986); A. Widom and J. Krim, Phys. Rev. B 34, R3 (1986); L. Bruschi and G. Mistura, Phys. Rev. B 63, 235411 (2001).
- 6.16 K.K. Kakati and H. Wilman, J. Phys. D: Appl. Phys. 6, 1307 (1973).
- 6.17 L.W. Bruch, submitted to J. Chem. Phys.

Chapter 7 References

- 7.1 P.J. Blau and C.E. Haberlin, *Thin Solid Films* 219, 129 (1992).
- 7.2 T. Thundat, R.J. Warmack, D. Ding, and R.N. Compton, *Appl. Phys. Lett.* 63, 891 (1993).
- 7.3 B. Bhushan, B.K. Gupta, G.W. Van Cleef, C. Capp, and J.V. Coe, *Appl. Phys. Lett.* 62, 3253 (1993).
- 7.4 T. Coffey, M. Abdelmaksoud, and J. Krim, *J. Phys.: Condens. Matter* 13, 4991 (2001).
- 7.5 G. Luengo, S.E. Campbell, V.I. Srdanov, F. Wudl, and J.N. Israelachvili, *Chem. Mater.* 9, 1166 (1997).
- 7.6 S.E. Campbell, G. Luengo, V.I. Srdanov, F. Wudl, and J.N. Israelachvili, *Nature* 382, 520 (1996).
- 7.7 B.M. Ginzburg, O.F. Kireenko, M.V. Baidakova, and V.A. Solovev, *Tech. Phys.* 44, 1367 (1999).
- 7.8 D.G. Tochilnikov and B.M. Ginzburg, *Tech. Phys.* 44, 700 (1999).
- 7.9 M.S. Dresselhaus, G. Dresselhaus, and P.C. Eklund, *Science of Fullerenes and Carbon Nanotubes*, (Academic Press, San Diego, 1996).
- 7.10 D.A. Neumann, J.R.D. Copley, R.L. Cappelletti, W.A. Kamitakahara, R.M. Lindstrom, K.M. Creegan, D.M. Cox, W.J. Romanow, N. Coustel, J.P. McCauley, Jr., N.C. Maliszewskyj, J.E. Fischer, and A.B. Smith, III, *Phys. Rev. Lett.* 67, 3808 (1991).
- 7.11 R.D. Johnson, C.S. Yannoni, H.C. Dorn, J.R. Salem, D.S. Bethune, *Science* 255, 1235 (1992).

- 7.12 P.A. Heiney, J.E. Fischer, A.R. McGhie, W.J. Romavow, A.M. Denenstein, J.P. McCauley, Jr., A.B. Smith, III, and D.E. Cox, *Phys. Rev. Lett.* 66, 2911 (1991).
- 7.13 R. Tycko, R.C. Haddon, G. Dabbagh, S.H. Glarum, D.C. Douglass, and A.M. Mujsce, *J. Phys. Chem.* 95, 518 (1991).
- 7.14 Q. Liang, O.K.C. Tsui, Y. Xu, H. Li, and X. Xiao, *Phys. Rev. Lett.* 90, 146102 (2003).
- 7.15 C. Lu and A. Czanderna, *Applications of Piezoelectric Quartz Crystal Microbalances*, (Elsevier, Amsterdam, 1984).
- 7.16 J.W. Bender and J. Krim, in *Microscale Diagnostic Tehcniques*, ed. D.S. Breuer (Springer-Verlag, New York, to be published.)
- 7.17 E. Watts, J. Krim, and A. Widom, *Phys. Rev. B* 41, 3466 (1990).
- 7.18 J. Krim and A. Widom, *Phys. Rev. B* 38, 12184 (1986); A. Widom and J. Krim, *Phys. Rev. B* 34, R3 (1986); L. Bruschi and G. Mistura, *Phys. Rev. B* 63, 235411 (2001).
- 7.19 E.I. Altman and R.J. Colton, *Surface Science* 295, 13 (1993).
- 7.20 T. Sakurai, X.D. Wang, T. Hashizume, V. Yurov, H. Shinohara, and H.W. Pickering, *Applied Surface Science* 87/88, 405 (1995).
- 7.21 S.M. Lee and J. Krim, in progress.
- 7.22 K.K. Kakati and H. Wilman, *J. Phys. D: Appl. Phys.* 6, 1307 (1973).
- 7.23 G.Z. Sauerbrey, *Phys. Verhandl.*, 8 113, 1957.

Chapter 8 References

- 8.1 C.M. Mate and B. Marchon, *Phys. Rev. Lett.* 85, 3901 (2000).
- 8.2 C.M. Mate, G.M. McClelland, R. Erlandsson, and S. Chang, *Phys. Rev. Lett.* 59, 1942 (1987).
- 8.3 G.J. Germann, S.R. Cohen, G. Neubauer, G.M. McClelland, and H. Seki, *J. Appl. Phys.* 73, 163 (1993).
- 8.4 J.N. Israelachvili and D. Tabor, *Wear* 24, 386 (1973).
- 8.5 H. Yoshizawa, Y.L. Chen, and J.N. Israelachvili, *J. Phys. Chem.* 97, 4128 (1993).
- 8.6 J.N. Israelachvili, P.M. McGuiggan and A.M. Homola, *Science* 240, 189 (1988).
- 8.7 M. Hirano, K. Shinjo, R. Kaneko and Y. Murata, *Phys. Rev. Lett.* 67, 2642 (1991).
- 8.8 C. Lu and A.W. Czanderna (eds.) *Applications of Piezoelectric Quartz Crystal Microbalances* (Amsterdam: Elsevier, 1984).
- 8.9 J. Krim and A. Widom, *Phys. Rev. B* 38, 12184 (1986).
- 8.10 J. Krim and A. Widom, *Phys. Rev. B* 34, R3 (1986).
- 8.11 E.T. Watts, J. Krim, and A. Widom, *Phys. Rev. B* 41, 3466 (1990).
- 8.12 J. Krim, D.H. Solina, and R. Chiarello, *Phys. Rev. Lett.* 66, 181 (1991).
- 8.13 A. Dayo and J. Krim, *Int. J. Thermophys.* 19, 827 (1998).
- 8.14 S.E. Campbell, G. Luengo, V.I. Srdanov, F. Wudl, and J.N. Israelachvili, *Nature* 382, 520 (1996).
- 8.15 B. Bhushan, B.K. Gupta, G.W. Van Cleef, C. Capp, and J.V. Coe, *Appl. Phys. Lett.* 62, 3253 (1993).
- 8.16 B.M. Ginzburg, O.F. Kireenko, M.V. Baidakova, and V.A. Solovev, *Tech. Phys.* 44, 1367 (1999).

- 8.17 Y. Golan, C. Drummond, M. Homyonfer, Y. Feldman, R. Tenne, and J.N. Israelachvili, *Adv. Mater.* 11, 934 (1999).
- 8.18 D.G. Tochilnikov and B.M. Ginzburg, *Tech. Phys.* 44, 700 (1999).
- 8.19 S. Lee, Y.S. Shon, T.R. Lee, and S. Perry, *Thin Solid Films* 358, 152 (2000).
- 8.20 T. Thundat, R.J. Warmack, D. Ding, and R.N. Compton, *Appl. Phys. Lett.* 63, 891 (1993).
- 8.21 G. Meyer and N.M. Amer, *Appl. Phys. Lett.* 57, 2089 (1990).
- 8.22 D. Schmicker, S. Schmidt, J.G. Skofronick, J.P. Toennies, and R. Vollmer, *Phys. Rev. B* 44, 10995 (1991).
- 8.23 M.S. Tomassone, J.B. Sokoloff, A. Widom, and J. Krim, *Phys. Rev. Lett.* 79, 4798 (1997).
- 8.24 J.W. Grate, S.J. Martin, and R.M. White, *Anal. Chem.* 64, 94 (1992).
- 8.25 M.J. Lea and P. Fozzoni, *Ultrasonics* 41, 133 (1985).
- 8.26 W.C. Duncan-Hewitt and M. Thompson, *Anal. Chem.* 64, 94 (1992).
- 8.27 M. Yang, M. Thompson, and W.C. Duncan-Hewitt, *Langmuir* 9, 802 (1993).
- 8.28 E.I. Altman and R.J. Colton, *Surf. Sci.* 295, 13 (1993).
- 8.29 T. Sakurai et al., *Appl. Surf. Sci.* 87/88, 405 (1995).
- 8.30 J.L. Barrat and L. Bocquet, *Phys. Rev. Lett.* 82, 4671 (1999).
- 8.31 J. Krim, J.G. Dash, and J. Suzanne, *Phys. Rev. Lett.* 52, 640 (1984).